FORTY FEMTOTESLA MICROELECTROMECHANICAL SYSTEMS (MEMS) MAGNETOMETER FOR BRAIN IMAGING

by

Kushagra Sinha

A thesis submitted to the faculty of
The University of Utah
in partial fulfillment of the requirements for the degree of

Master of Science

Department of Electrical and Computer Engineering

The University of Utah

August 2016

The University of Utah Graduate School

STATEMENT OF THESIS APPROVAL

The thesis of **Kushagra Sinha**

has been approved by the following supervisory committee members:

Massood Tabib-Azar	, Chair	**05/13/2016** Date Approved
Carlos H. Mastrangelo	, Member	**05/13/2016** Date Approved
Marc Bodson	, Member	Date Approved

and by **Gianluca Lazzi** , Chair/Dean of

the Department/College/School of **Electrical and Computer Engineering**

and by David B. Kieda, Dean of The Graduate School.

ABSTRACT

The design, working principle, fabrication, and characterization of ultrasensitive ferromagnetic and magnetoelectric magnetometer are discussed in this thesis. Different manufacturing techniques and materials were used for the fabrication of the two versions of the magnetometer. The ferromagnetic microelectromechanical systems (MEMS) magnetometer was fabricated using low-pressure chemical vapor deposition (LPCVD) of silicon nitride, yielding low compressive stress, followed by patterning. The built-in stress was found to be -14 Mpa using Tencor P-10 profilometer. A neodymium magnet (NdFeB) was used as a foot-mass to increase the sensitivity of the device. A coil (Ø=3 cm), placed at a distance from the sensor (2.5-15 cm), was used to produce the magnetic field. The response of the ferromagnetic MEMS magnetometer to the AC magnetic field was measured using Laser-Doppler vibrometer. The ferromagnetic sensor's average temperature sensitivity around room temperature was 11.9 pV/pT/°C, which was negligible. The resolution of the ferromagnetic sensor was found to be 27 pT (1 pT = 10^{-12} T). To further improve the sensitivity and eliminate the use of the optical detection method, we fabricated a Lead Zirconate titanate (PZT) based magnetoelectric sensor. The sensor structure consisted of a 9 mm long, and 0.17 mm thick PZT beam of varying widths. A neodymium permanent magnet was used as a foot-mass in this case as well. The magnetic field from the coil generated a driving force on the permanent magnet. The driving force displaced the free end of the PZT beam and generated a proportional

voltage in the PZT layer. The magnetoelectric coupling, i.e., the coupling between mechanical and magnetic field, yielded a sensor resolution of ~40 fT (1 fT = 10^{-15} T); an improvement by three orders of magnitude. We used high permeability Mu sheets (0.003") attached to copper plates (0.125") to shield stray magnetic fields around the sensor. For both the ferromagnetic MEMS and the magnetoelectric magnetometer, the initial output was improved by using external bias and parametric amplification. By applying an external DC magnetic field bias to the sensor, the effective spring compliance of the sensor was modified. Electronic feedback reduced the active noise limiting the sensor's sensitivity. We used magnetic coupling to enhance the sensors' sensitivity and to reduce the electronic noise. Two identical sensors, with identical foot-mass (permanent magnet), was used to show coupling. The magnet on one of the sensors was mounted in NS polarity, whereas, on the other it was in SN polarity. When excited by the same external AC magnetic field (using coil), one of the sensors was pulled towards the coil and the other was pushed away from it. Adding the individual sensor output, using a preamplifier, an overall increase in sensors' output was observed. The techniques mentioned above helped to improve the output from the sensor. The sensitivity of the sensor can be improved further by using a 3-axis magnetic field cancellation system, by eliminating the AC and DC stray magnetic field, by using coupled-mode resonators and by increasing the surface field intensity of the foot-mass. The magnetometers, thus, developed can be used for mapping the magnetic print of the brain.

TABLE OF CONTENTS

ABSTRACT iii

LIST OF TABLES vii

LIST OF FIGURES viii

ACKNOWLEDGEMENTS xiii

PREFACE xiv

Chapters

1. INTRODUCTION 1

    1.1 Magnetic Field from Brain 2
    1.2 Background 3
        1.2.1 Existing Detection Techniques 4
        1.2.2 MEMS Magnetometers Reported in the Literature 7
    1.3 Our Approach and Methods 8

2. DESIGN AND DYNAMICS OF MAGNETOMETER 19

    2.1 Structural Dynamics of the Sensor 19
    2.2 Sensor Design 23
    2.3 Strategies to Improve the Sensor Signal 26
        2.3.1 Spring Constant Modification 26
        2.3.2 Shielding and Concentrators 29
        2.3.3 Parametric Amplification 31
        2.3.4 Coupled Resonator 32
        2.3.5 Noise Reduction Techniques 35
        2.3.6 Vacuum 36
    2.4 Experimental Procedures 37
    2.5 Transduction Techniques 39
        2.5.1 Optical Transduction 39
        2.5.2 Piezoelectric Transduction 40
        2.5.3 Magnetostrictive Transduction 41
        2.5.4 Capacitive Transduction 42

2.5.5 Piezoresistive Transduction 43

3. FERROMAGNETIC MAGNETOMETER 52

3.1 Sensor Design 52
3.2 Fabrication 53
3.3 Simulation 54
3.4 Experimental Set-up 54
3.5 Results 55
3.5.1 Extended Spectrum 55
3.5.2 Signal Improvement Strategy: Results 56
3.5.2.1 Spring Constant Modification 56
3.5.2.2 Shielding and Concentrators 58
3.5.2.3 Vacuum 59
3.5.2.4 Parametric Amplification 60
3.5.2.5 Noise Reduction Techniques 63
3.6 Temperature Dependence 63

4. MAGNETOELECTRIC MAGNETOMETER 82

4.1 Overview 82
4.2 Sensor Design 85
4.3 Fabrication 86
4.4 Experimental Set-up 87
4.5 Results 88

5. CONCLUSION 105

APPENDIX 111

REFERENCES 113

LIST OF TABLES

Table

1.1 Comparison of the sensitivity and the MDS for the MEMS magnetometers reported in the literature……18

3.1 The effect of the external bias on the resonant frequency and the amplitude of the ferromagnetic MEMS magnetometer (device #1)…….…..…81

LIST OF FIGURES

Figure

1.1. Hierarchy involved in magnetic field production starting from a single neuron to the human brain as a whole…….13

1.2. A single neuron, with parts labeled, showing the direction of flow of current……13

1.3. Comparison of field propagation in a single neuron and the human brain as a whole. Also, note the current and the magnetic field magnitude involved…….14

1.4. (a) A typical spectral response measured using EEG (b) electrode placement for measurements……..……14

1.5. Schematic showing working principle of magnetoencephalography……...15

1.6. Schematic showing the working principle of SQUIDs a type of MEG, with (a) detailed look at the individual sensor (b) positioning of sensors on the human skull….15

1.7. Schematic of a DC SQUID's electronics based on flux modulation and phase sensitive detection…….……..16

1.8. The approach used for the ultra-sensitive ferromagnetic (27 pT resolution) and the magnetoelectric (40 fT resolution) magnetometer……..16

1.9. Schematic showing the interaction between the magnetic field from the permanent magnet used as a foot-mass on the sensor and the AC magnetic field produced by a coil to either (a) attract (b) repel the flexure……..17

2.1. Schematic showing the sensor with the parameters affecting its dynamics…….45

2.2. Schematic showing the interaction between the magnetic field (B) produced by the coil and the permanent magnet (M´) used as a foot-mass……...45

2.3. Representation of the ferromagnetic MEMS sensor (a) device #1 (b) device #2 showing the effective Hooke's constant……..46

2.4. Effective force on the ferromagnetic MEMS sensor subject to (a) no external bias (b) +13.75 mT (c) –13.75 mT bias……...……..46

2.5. Graphical showing improvement in attenuation by increasing high-Mu sheet thickness……47

2.6. Representation of the principle of operation used in parametric amplification. We optimally selected the band-pass frequency for maximum output……...47

2.7. Diagram showing the electromagnetic coupling between the resonators……..48

2.8. Schematic showing the out-of-phase and in-phase motion of the coupled resonator……...48

2.9: Graphical comparison of (a) the output and, (b) the noise-floor from the magnetoelectric sensor for different working conditions…….…49

2.10. Graphical comparison of electronic noise from the magnetoelectric sensor for optical and piezoelectric transduction at 0.07 nT and 0.8 nT input……..49

2.11. Pictorial representation of the setup used for calibrating the coil using RM-100 NanoTesla meter…….…..50

2.12. The magnetic field produced by the coil with varying (a) input voltage, and (b) stand-off distance calibrated using RM-100 NanoTesla meter……51

3.1. Optical image of the ferromagnetic MEMS sensor structures, namely: (a) plus-bridge (device #1) (b) 3-leg bridge (device #2) (c) normal bridge (device #3), and (d) diaphragm (device #4)…….….66

3.2. Representation of the fabrication steps used for the silicon nitride based ferromagnetic MEMS magnetometer……...66

3.3. (a) Graphical comparison of the experimental and the simulated output for the device #1 with 0.07 nT input to the coil and, (b) simulated frequency and displacement for 200 nN force……67

3.4. Table showing (a) the device parameters and (b) the material properties used for simulation……..68

3.5. Schematic showing the experimental set-up used for the ferromagnetic MEMS magnetometer characterization……68

3.6. An optical image of the experimental setup used for the ferromagnetic MEMS sensor characterization……..69

3.7. A spectrum showing the RMS noise level of 2.8 μV for the device #1. The input to the inner coil (see Figure 2.5) was fixed at 0.07 nT. The bandwidth used was 2 Hz. We calculated the RMS noise level from 638 Hz to 3 KHz……69

3.8. Graphical representation of effect of the external bias with (a) -Z polarity (b) +Z polarity on the amplitude and the frequency for the device #1……70

3.9. Graphical representation of the variation in (a) the amplitude and (b) the resonant frequency with varying external bias……71

3.10. Graph showing the effect of external bias polarity and strength on the spring constant of the ferromagnetic MEMS magnetometer……...72

3.11. Graph showing the deflection in the wafer as a function of distance measured using a Tencor P-10 Profilometer……...72

3.12. Schematic of High-Mu enclosure used for (a) the ferromagnetic MEMS magnetometer and (b) the magnetoelectric magnetometer……...73

3.13. Graphs showing the comparison of output under atmospheric pressure and vacuum (1 mTorr) for (a) 7 mm normal-bridge, and (b) 10 mm cross-bridge……...73

3.14. Graphs showing variation in (a) the amplitude and (b) the change in the resonant frequency for the device #1, with an increase in the input gain of the outer coil (see Figure 3.5) used for parametric amplification……..74

3.15. Graph comparing the ferromagnetic MEMS sensor's (device #1) output as a function of the input magnetic field for no feedback, parametric amplification, and AC input……..74

3.16. Graph comparing the MDS and the noise-floor for the device #1 and the device #2 using parametric amplification (PA) and no feedback (NF)……75

3.17. Graph showing the MDS and the noise-floor for device #2 (a) without feedback, and (b) with parametric amplification……..76

3.18. Graphical comparison of output from the ferromagnetic MEMS sensor (a) without feedback (b) with feedback for 0.07 and 0.8 nT input for device #1……77

3.19. A spectrum showing the amplitude variation with varying input to the coil. We measured the electronic RMS noise in the frequency range 800 Hz to 1.5 KHz, without using any active vibration control instrument……..77

3.20. Graphical comparison of the RMS noise-floor for the ferromagnetic MEMS sensor (device #1)……78

3.21. (a) Schematic representation and (b) optical image of the experimental set-up used to study the effect of temperature on the ferromagnetic MEMS magnetometer (device #2)……79

3.22. Variation in (a) the resonant frequency and (b) the temperature coefficient of the ferromagnetic MEMS magnetometer (device #2) for 28.8 and 0.8 nT input from the coil……80

4.1. Schematic representation of the PZT disc used for the fabrication of the magnetoelectric sensor……..94

4.2. Diagrammatic representation of the magnetoelectric magnetometer (a) without and (b) with neodymium magnet as a foot-mass……94

4.3. Optical image of the magnetoelectric magnetometer……....94

4.4. (a) Layout of the experimental set-up used for testing the magnetoelectric sensor (b) Optical image of the set-up……...95

4.5. Graphs showing variation in (a) the spectrum (b) the resonant frequency and, (c) the output for different foot-mass (permanent magnet) surface magnetic field…….96

4.6. Schematic of coupled beams with the permanent magnets in opposite polarity and the setup used to detect the output……97

4.7. Spectrum showing coupled response for the magnetoelectric sensors (N9 and N10)……..97

4.8. A graph comparing the output from the coupled resonator as a function of the coupling gap…….….98

4.9. Comparison of MDS for individual magnetoelectric magnetometers (device #1 and device #2) with the coupled-mode resonator……98

4.10. Spectrum showing variation of the resonant frequency and the amplitude with a) resonator-1 as driver and resonator-2 as detector b) resonator-2 as driver and resonator-1 as detector…….99

4.11. Graph showing variation of the spring constant with a) resonator-1 as driver and resonator-2 as detector b) resonator-2 as driver and resonator-1 as detector…….100

4.12. Graphical comparison of the output for best (N9&N10) and the worst (N1&N2) devices using (a) parametric amplification (b) no feedback……...101

4.13. Results comparing the MDS for parametric amplification and no feedback for (a) N9 and (b) N10…….……..102

4.14. Comparison of the output from N9 with RM-100 output at lower magnetic field…….103

4.15. Comparison of the (a) MDS (b) sensitivity for the various magnetoelectric sensors used. The output was extrapolated using 2nd order polynomial function……...104

ACKNOWLEDGEMENTS

To begin with, I would like to thank my advisor, Dr. Massood Tabib-Azar for providing me the opportunity to work on different projects. He has been a source of inspiration and support throughout my MS program at the University of Utah. His guidance and advice throughout the research helped me overcome many hurdles. The training provided by him in the laboratory helped me learn the art of sensor design, characterization and proper use of sophisticated equipment. I also would like to extend my gratitude to the other thesis committee members, Dr. Carlos Mastrangelo and Dr. Marc Bodson.

I would like to thank Olutosin C. Fawole, who helped me with most of the experimental set-ups. Be it LabVIEW programming, basic laboratory skills or complex instrument problems, he was always there to guide me, and I thank him for the same. I would also like to thank Rugved Likhite for fabricating the silicon nitride MEMS version of the sensor and working hard to get the devices ready on time. It was amazing brainstorming the problems with him to find perfect solutions for the research stopovers. Dr. Pradeep Pai was a constant source of inspiration and support, be it with device design or material considerations. I would like to thank him for his quick email replies and on call solutions whenever needed.

PREFACE

The ferromagnetic and magnetoelectric sensors have many advantages over magnetoresistive, Hall Effect and flux gate magnetometers. Their structures are relatively simple and easy to fabricate, and they are more sensitive. However, they are sensitive to temperature variations. They consist of a flexure and a permanent magnet that can be deposited by micro-fabrication technique. As we will show later, they can measure small magnetic flux densities (~40 fT) suitable for brain mapping. They can also be designed to have a wide operational bandwidth. Our main objective was to develop magnetometers for brain activity imaging. In order to map the magnetic field produced by the brain, it is important to understand the origin of this magnetic field. In **Chapter 1** we will discuss how neuron firings produce a magnetic field. Then, we will discuss the existing technologies for the magnetic field detection. We will then summarize the MEMS magnetometers reported in the literature.

Measuring ultra-low magnetic flux density (fT) produced by the neuron firings require a sensitive MEMS structure that produces large displacement (μm) for a rather small force generated by the field (pN-nN). In **Chapter 2** an overview of the ultra-low magnetic field sensor design and dynamics will be presented. We will discuss the materials suitable for the sensor structure and fabrication, keeping in mind robustness and sensitivity. We will also go through six signal improvement strategies, namely: spring constant adjustment, shielding and concentrators, vacuum, coupled resonators, parametric

amplification, and noise reduction used for improvement of the sensor resolution and sensitivity.

In **Chapter 3** we will discuss the ferromagnetic MEMS magnetometer. The sensor design, fabrication, characterization, and results will be presented. We designed four different structures, namely: plus bridge, 3-leg bridge, fixed-fixed bridge, and diaphragm, with varied dimensions (length -6 to 10 mm and width -1 to 4 mm). To improve the sensitivity of the sensor, a neodymium rare earth magnet was used as a foot-mass for the flexure. The sensor parameters including mass, spring constant, and damping coefficient were adjusted using external bias, parametric amplification and vacuum. The above-mentioned techniques helped in achieving maximum response (amplitude) for minimum magnetic force on the sensor. The force was produced by the magnetic field from a coil (Ø=3 cm), placed at a distance (2.5 -15 cm) from the sensor. We used external bias of varying flux densities (+28 mT to -28.75 mT) and studied its effect on the MEMS sensor response. The external bias modified the sensor response by applying and modifying tension of the bridge. When the internal tension was reduced by the external field, the sensors' response improved. Parametric amplification, external bias, electronic noise cancellation and vacuum improved the sensor resolution and sensitivity. The resolution of the MEMS ferromagnetic sensor was 27 pT, and the sensitivity was 0.67 mV/nT.

In addition to the ferromagnetic MEMS sensor, we also fabricated a PZT based magnetoelectric magnetometer. The magnetoelectric (ME) effect is the process by which a voltage is induced in a material (PZT in our case) when an external magnetic field is applied. The magnetoelectric magnetometer proved to be highly sensitive and had lower

noise than the ferromagnetic magnetometer. We will discuss the design, fabrication, experimental set-up, and results for the magnetoelectric magnetometer in **Chapter 4**. Ten sensors were fabricated using a 9.9 mm PZT disc. A copper box lined with high-Mu sheets, was used in the case of the magnetoelectric sensor, to shield the parasitic magnetic field. Parametric amplification was used to enhance the sensitivity (1.63 mV/nT) of the sensor. A vibration isolation system along with a pneumatic isolation workbench reduced the overall noise-floor. The use of a magnetoelectric sensor allowed the elimination of the optical detection method. The resolution of the magnetoelectric magnetometer was found to be ~40 fT with a sensitivity of 1.63 mV/nT.

The resolution and the sensitivity of the sensors discussed in this thesis can be further improved by optimizing the magnet mass, using coupled-mode sensors, and employing a three-axis external magnetic field cancellation system, for reducing the external direct current (DC) and alternating current (AC) magnetic field changes, using a three pair compensation coil system. We will discuss these techniques in the last section of Chapter 4. **Chapter 5** concludes the thesis by summarizing the sensor's structure, their fabrication, and sensitivities.

CHAPTER 1

INTRODUCTION

Ultra-sensitive, room temperature magnetometers with 10 femtoTesla (fT) minimum detectable signal (MDS) are required for magnetoencephalography (MEG), to image and connect our brain circuitry and firing patterns to our behavior. Atomic vapor, high-temperature, superconducting quantum interference devices (SQUIDs), and very high sensitivity micro-electromechanical systems (MEMS) magnetometers are being developed for these and related applications [1]. When compared to macroscale devices, the microelectromechanical systems (MEMS) based sensors are more compact, consume less power, have low cost, have large scale production capability, are easy to use and are more sensitive. The human brain consists of 10^{11} neurons [2] in the outermost layer called the cerebral cortex. These individual neurons form signal transfer pathways with 10^{14}-10^{15} synapses [2]. The information processing in the brain is the result of a series of chemical changes following an external stimulus. This processing and flow of information through neurons produces an electric current of the order of 0.1 nA per neuron. As we know from the Faraday's law, a current carrying conductor creates a magnetic field around it. The strength of the magnetic field generated by a single neuron is too weak and difficult to detect. However, if a bundle of neurons (~thousand) close to the skull is excited in unison, it can be detected using ultrasensitive, noninvasive detection mechanisms. A detail of the magnetic field produced by the brain follows in the

subsections below.

1.1 Magnetic Fields from the Brain

The human brain is a very intricate and complex structure that has inspired numerous path-breaking discoveries. As mentioned in the introduction, part of the brain that interests scientists most is the cerebral cortex layer, as it contains 10^{11} neurons. The cerebral cortex layer plays a key role in memory, thoughts, awareness, attention, perception, language, and consciousness. It is a 2-4 mm thick layer, gray in color and has a total surface area of about 2500 cm^2 (see Figure 1.1). Two types of currents arise, in response to a sensory stimulus in the human brain: primary current and volume current. The current produced in the neurons as a result of an ionic gradient is called the primary current. The surrounding medium, mainly consisting of cerebrospinal fluid, has the volume current, which neutralizes the ionic charge.

The body of a neuron is called the Soma [4] (see Figure 1.2). The Soma contains the nucleus and all other organelles that keep the cell alive and functioning. Neurons also have directionality associated with them. One end of the neuron contains the dendrites, which act as the signal source. The outputs (synapses) of surrounding neurons are connected to the dendrites. The other end is called the axon. The axon ends in synapses that connect to the dendrites of neighboring neurons. The axon is usually much longer than the Soma. There are some neurons with axons that extend the entire length of the human body. An action potential is an electric pulse that travels down the axon until it reaches the synapses. The resting potential of a neuron is around -70 mV when the neuron is inactive. When it is excited, the action potential travels along the axon in the form of a voltage spike (see Figure 1.3). A weak stimulus produces a lower rate of pulse

transfer than a stronger stimulus. Recording the magnetic fields produced by synchronized axon current (0.1 nA) is difficult, as it has a low intensity. Fortunately, neurons located near each other fire together, producing larger magnetic fields. The magnetic field of 10^6 neurons is around the order of 10 fT -10 pT [5], depending on the distance and the orientation. The magnetic field generated by the neural current is 10 fT for the cortical activity and 103 fT for the human alpha rhythm (see Figure 1.3). The magnetic field is less distorted than the electric field by the skull, scalp, and cerebrospinal fluid and hence, can be picked up by sensitive sensors, to map them without any alteration. The challenge involved in measuring the weak magnetic fields includes the need for an ultrasensitive sensor, and the elimination of the magnetic noise from the geomagnetic field variation, overhead power lines, electromagnetic waves and other parts of the body.

1.2 Background

The electrical conduction mechanism in the cerebral cortex of the brain is quite complex and highly anisotropic. The white matter of the cortical area, which gets its appearance due to the sheath on the axon part of the neuron, allows ten times faster pulse transfer along the axon than in the transverse direction. Many detection techniques take advantage of this directionality. Either by employing a particular material property like piezoelectricity [6-8], magnetostriction [6, 9, 10. 11], and ferromagnetism [12, 13], or by using the Hall Effect [11, 14, 15] and the Lorentz force [16-19], transduction can be achieved. We will discuss the use of specific material property or physical phenomenon mentioned above, for transduction that is currently in commercial use or reported in the literature, in the subsections.

1.2.1 Existing Detection Techniques

Electroencephalography (EEG) and Magnetoencephalography (MEG) measure the electromagnetic effect at the surface of the skull produced by the combined current in the neuron bundle [20]. The origin of EEG and MEG are very similar. The first recording of the electric field of the human brain was made by the German psychiatrist Hans Berger in 1924 in Jena, Germany. EEG is sensitive to both the tangential and the radial components of a potential source. EEG offers the advantage of having a higher temporal resolution as opposed to the spatial resolution. The spatial resolution is suppressed by the presence of multilayered tissue interfaces, such as the skull, cerebrospinal fluid and other cortical layers between the electrode and the neuron bundle [21]. By solving the inverse problem procedures, spatial maps from the measurements can be derived. Intersource interfaces and distributed activation centers pose complexity in the derivation of a perfect brain map using these mapping techniques [22, 23]. Figure 1.4a shows a typical EEG spectral response to external stimuli. Considering that the spatial resolution is lower for EEG, of the EEG electrode placement. Magnetoencephalography (MEG) measures the magnetic field produced by the current flow in the neurons that is generated directly by the neuron firings [25]. MEG has the potential to measure very high temporal as well as spatial resolution. Similar to EEG, it is entirely noninvasive. As mentioned before, the voltage spikes in the axon are produced due to a stimulus. These peaks become abnormal in the case of a disease, such as Parkinson's disease, and the effect of carcinogens, psychiatric disorders, etc. (see Figure 1.5). The magnetic field pattern can hence be studied to compare the response of an abnormal and a healthy brain. The Figure 1.5 pictorially represents the working of a typical MEG. As seen before, the magnetic field from the

neuron is similar to a current conducting wire, the direction of which can be represented by the “Right-hand rule”. The direction of the thumb will account for the direction of flow of the current, and the orientation of the finger curl represents the sense of the magnetic field generated by it. The field lines closer to the source are stronger, and they become weaker as the distance increases. Current MEG uses SQUIDs that are very sensitive, but have large sizes and require cooling.

Figure 1.6 briefly describes the operation of SQUIDs. The SQUID sensor consists of a superconducting path which gets separated into two, by the use of the “Josephson junction”. At the Josephson junction, current flows indefinitely long and is called the super-current. The uninterrupted current flow in a superconductor, without the application of a voltage difference, occurs due to the “Josephson Effect”. A weak link couples the two superconductors forming the “Josephson junction”. The weak link can consist of a superconductor–insulator–superconductor (SIS) junction, a short section of a non-superconducting metal, or a physical choke point that can weaken the superconductivity at the “Josephson junction”. The magnetic field lines intersecting the square hole of the SQUIDs sensor, determines the phase of electron waves circulating in the SQUIDs superconducting region (see Figure 1.6). The interference of these waves is proportional to the magnetic flux detected over the hole. Superconductors have no electrical resistance and hence the interference can be measured only by introducing an interference in the superconductor. The weak magnetic field from the neurons picked up by the sensors is given to the readout mechanism, as discussed later. The SQUID sensor also contains a feedback coil that gets magnetically coupled to the pickup coil. The MEG system uses computer programs to convert the data proportional to the current flowing

throughout the brain as a function of time, into maps. A typical SQUID sensor measures 10 to 100 micrometers on a side. The output from the sensor gets transferred to a series of preamplifiers and buffers that need shielding from the stray magnetic field, and hence, are kept inside a shielded room (see Figure 1.7). The primary electronics do not need shielding. They consist of a synchronous detector, PI controller, a phase shift compensation, a bias current control, a flux modulator, a reset, and an auto zero component. A proportional-integral (PI) controller is used to feedback a signal to the output (process variable). Applications of the MEG system include basic research of the perceptual and cognitive brain processes, localizing regions affected by pathology before surgical removal, determining the function of various parts of the brain, and neurofeedback. Another form of MEG is in testing, and is called SERF (spin exchange relaxation-free). SERF uses lasers to study the interaction between the alkali metal (Li, Na, K, etc.) atoms in the vapor phase and the magnetic field to be measured. In the case of SERF, the total angular momentum due to spin-exchange collision is preserved by two rapid collisions, thus eliminating a relaxation phase (relaxation-free). They can operate at near zero magnetic fields.

Apart from mapping the magnetic field of the brain using EEGs and MEGs, other applications of magnetometers are in the areas of archeology, mineral exploration, directional drilling in rigs, spaceships, biological signal sensing, and automation, to name a few. MEMS-based magnetometers find broad application in clinical practices, not only detecting a particular disease, but pinpointing the area of the brain causing neurological and psychiatric diseases. As neuropsychiatric disorders like mood disorders, stroke, epilepsy are among the most common neurodiseases, this mapping technique will further

help in the identification of effective therapeutic strategies, which will benefit the lives of millions of patients. We will now review the MEMS magnetometers reported in the literature. Some of them have been in commercial production, whereas most others are still in testing.

1.2.2 MEMS Magnetometers Reported in the Literature

To measure magnetic field variation, a physical parameter of the sensing material should change which can be measured. This change can be in resistance, stress, dimensions, spin orientation of atoms, etc. By developing methods to detect these changes, many magnetometers have been reported. The sensitivity and the minimum detectable signal (MDS) are the primary parameters that define the effectiveness of a sensor for transduction. The Lorentz force, the Hall Effect, AMR, GMR, magnetostriction, the magnetoresistive effect, and flux gate are some of the commonly used transduction techniques reported. Mo Li et al. [29] reported a Lorentz force magnetometer for an electronic compass with a resolution of 210 nT/√Hz operating using a DC supply of 2 V at 21.29 KHz resonance frequency. In the recent past, a new approach for sensor fabrication has been used. Marauska et al. [30] used magnetoelectric composites as a cantilever deposit to detect magnetic field as low as 30 pT with a sensitivity of 3800 V/T. Using a bias current of 7.245 mA, Kumar et al. [31] reported the sensitivity of a Lorentz force magnetometer device to be 2.107 mV/nT. They also used parametric amplification to increase their sensor's sensitivity. A Lorentz force, based, torsional resonant magnetometer has been reported by Ren et al. [32], that had a sensitivity of 400 mV/μT and a resolution of upto 30 nT in 10 Pa vacuum. Kadar et al. [33] reported a magnetometer with 1 nT resolution using a device with dimension 2800

μm × 1400 μm. The Lorentz force sensors have the advantage of being hysteresis free when compared to the magnetoresistive and the flux gate magnetometers. Various other methods have been used to report the sensing of magnetic field variation. Haned and Missous [34] used the Hall Effect to sense magnetic flux density change and were able to achieve 100 nT resolution. Bertoldi et al. [35] used anisotropic magnetoresistive effect (AMR) as the transduction technique to detect the magnetic field changes as small as 20 nT. Wang et al. [36] used the giant magnetoresistance effect (GMR) as the transduction technique to achieve a resolution level of 30 nT. Liakopoulos and Ahn [37] used the micro-fluxgate principle to detect a minimum of 60 nT signal, and they used 3D toroidal type planar coils for detection and excitation. Yabukami et al. [38] reported a high-frequency carrier-type sensor with 88 pT resolution using the giant magneto-impedance effect (GMI). Thus, the MEMS magnetometers as reported in the literature can be used to detect ultra-low magnetic fields. We will now compare the sensitivity and the minimum detectable signal (MDS) reported in the literature with our magnetometers in Table 1.1.

1.3 Our Approach and Methods

To understand a research problem at hand, one needs to review the literature and formulate a hypothesis. Additionally, a preliminary research design is needed. To address the issue of detecting ultra-low magnetic fields, possible relations between the variables involved are needed. From sensor design, material selection, experimental set-up, collection of data in various stages, and converting it to a numerical form, and to drawing conclusions, a sequential approach was adopted (see Figure 1.8). We fabricated a ferromagnetic MEMS sensor and a magnetoelectric sensor for the magnetic field detection.

The ferromagnetic sensor comprised of four different structures, namely: 3-leg bridge, plus bridge, fixed-fixed bridge, and diaphragm. The magnetoelectric magnetometer structure was a fixed-free beam. To maximize the output, our approach was to study the dynamics of the flexure beam structures and change the beam parameters electronically. According to the beam dynamics, the force (*F*) exerted on the beam is related to the amplitude of vibration *(x*), the spring compliance (*k*), the damping coefficient (*b*), the resonant frequency (ω) and the mass (*M*) as shown in the Equation below:-

$$F = M\ddot{x} + b\dot{x} + kx \tag{1.1}$$

$$\omega = \sqrt{\frac{k}{M}} \tag{1.2}$$

From Equation (1.1) it was deduced that there are mainly three parameters that can be modified to change the sensor's output (*x*) in response to an external force (*F*):

1) Mass (by changing foot-mass),
2) Damping coefficient (by introducing vacuum), and
3) Spring constant (using external bias, parametric amplification, and magnetic coupling).

Both the ferromagnetic and the magnetoelectric sensors used a permanent magnet (NdFeB) with 1 mT surface field intensity as a foot-mass. A coil placed at a distance (2.5-15 cm) from the sensor produced the magnetic field to be detected. Whenever there is a flow of current through a straight wire or a coil, a magnetic field is generated. The orientation of the magnetic field depends on the type (AC/DC) and the direction (clockwise/anti-clockwise) of input. The resultant magnetic field from an AC input

switches polarity as well as amplitude with time (see Figure 1.9), whereas the field created using a DC input is of constant amplitude and phase. The displacement produced by the force between the permanent magnet on the sensor and the coil was measured as change in its velocity using a Laser-Doppler vibrometer in the case of the ferromagnetic MEMS sensor, and as a voltage output from the PZT in the case of the magnetoelectric sensor.

Using the magnetic field generated by the coil as input (see Figure 1.9), the output response of the sensor was determined and measured. We chose to use a permanent magnet as a foot-mass for our sensor. The ferromagnetic materials (Fe, Co, Fe_2O_3, etc.) could also be used as the foot-mass. However, a ferromagnetic material needs to be magnetized. Depending on the residual magnetism in the ferromagnetic material the external magnetic field (*B*) would exert a force on it. The magnetization of a ferromagnetic material is not linear and requires a large magnetic field for saturation (1-1.5 T). To determine why permanent magnet serves better, we will first try and understand how a ferromagnetic material gets magnetized.

$$M' = \frac{\chi_m B}{\mu} \tag{1.3}$$

where '*M*'' is the magnetization in ferromagnetic material, 'χ_m' is the magnetic susceptibility, '*B*' is the applied magnetic field and 'μ' is the permeability of the ferromagnetic material. The permeability (μ) of the ferromagnetic material varies as $\mu = k_m \mu_0$, where 'k_m' is the relative permeability and 'μ_0' is the permeability of the free space. In the case of the ferromagnetic materials, 'χ_m' ranges from several hundreds to 100,000 ($\times 10^{-6}$ S.I unit). The relative permeability can be also related as: $k_m = 1 + \chi_m$,

using this in the permeability Equation, we get: $\mu = (1 + \chi_m)\mu_0$. Replacing 'μ' in the Equation 1.3, we get: -

$$M' = \frac{\chi_m B}{(1+\chi_m)\mu_0} \quad (1.4)$$

Considering '*B*' to be in the range ~0.1-10 nT, as used in our experiment '*M'*' will be in the range 10^{-5}-10^{-7} mT. Comparing this to the 1 mT surface field of the permanent magnet used, a ferromagnetic materials magnetization would be 10^5-10^7 times less. Hence, we used a permanent magnet instead of the ferromagnetic material, as a foot-mass.

After selecting the sensor design and foot-mass material, the sensors were fabricated using microfabrication techniques. The ferromagnetic MEMS magnetometer composed of a low compressive stress (-14 MPa) silicon nitride devices, with a neodymium rare earth magnet (NdFeB) as a foot-mass. The magnetic field was produced in a coil (Ø=3 cm) using input from network analyzer (0.07-8.5 nT). The output from the sensor was improved using the techniques as discussed in Chapter 2. The sensors' output was amplified along with a 90˚ phase shift and fed back to a second coil (Ø 6.5 cm). The feedback, parametrically increased the source magnetic field, improving the sensor's sensitivity by 350 times (from 1.9 µV/nT to 0.67 mV/nT) and its MDS by four orders of magnitude (from 1 µT to 27 pT). Our research group has reported a fiber optic magnetometer with sub pT sensitivity in the past (Pai et al. [39]), using a permanent magnet and fiber optics. To improve the sensor's sensitivity and MDS, we reduced its effective elastic constant by applying an external DC bias (±13.75 to ±28.75 mT). The electromagnetic noise was reduced by shielding the sensor with high-Mu sheet (0.006").

The magnetoelectric sensor was fabricated by trimming the PZT discs (Ø=9.9 mm) into flexure beams. Use of PZT-based sensor eliminated the need of an optical detection method. Using the magnetoelectric sensor, the MDS was improved by six orders of magnitude (~40 fT) and the sensitivity was enhanced by a factor of 2.5. The electromagnetic noise, in this case, was reduced by shielding the sensor using the copper plates (0.125") with the high-Mu sheets (0.006") attached to it. In the next chapter, a detailed discussion on the sensor dynamics, material, equipment, noise, and output improvement strategies are presented.

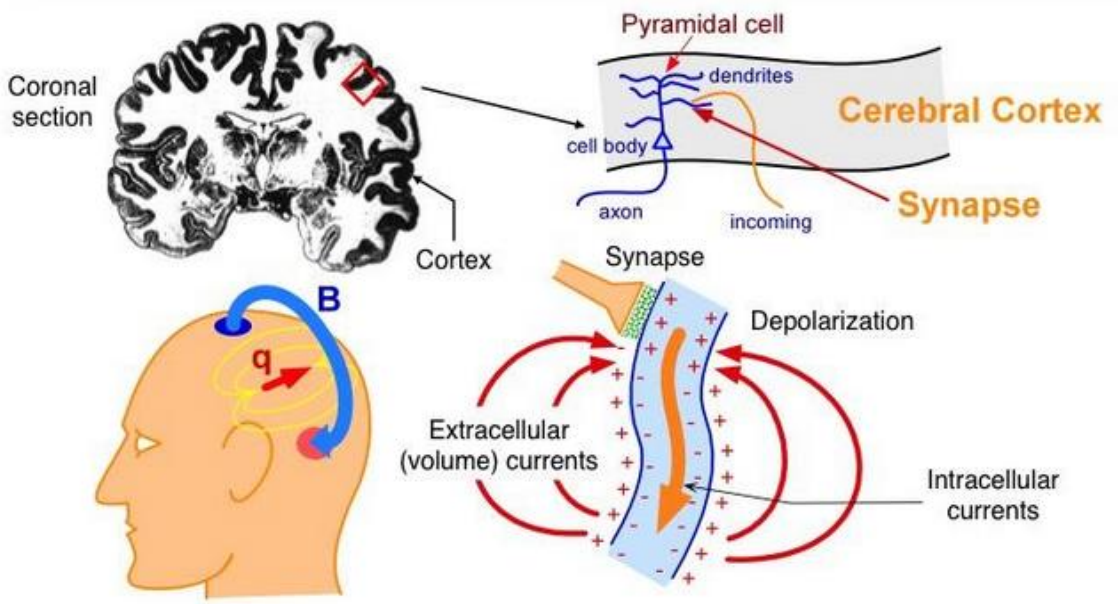

Figure 1.1. Hierarchy involved in the magnetic field production starting from a single neuron to the human brain as a whole [3].

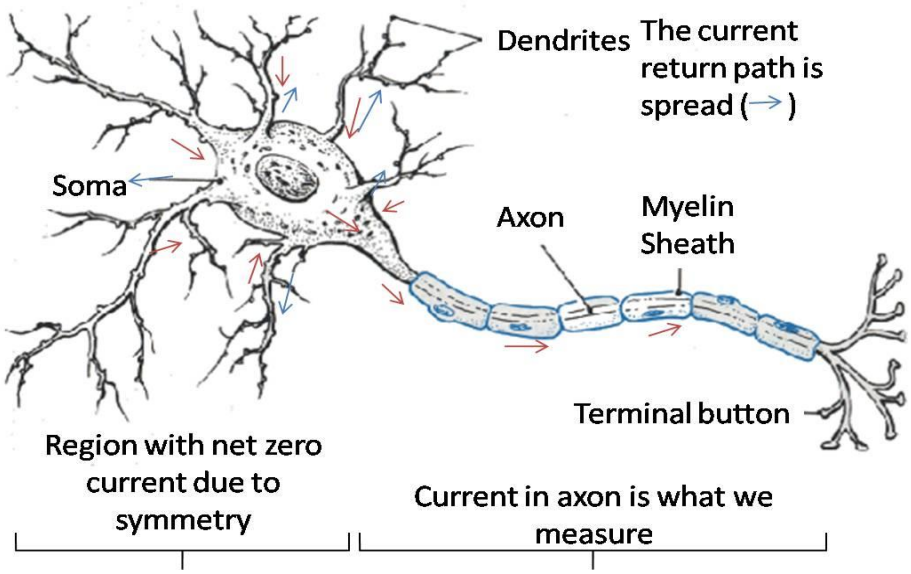

Figure 1.2. A single neuron, with parts labeled, showing the direction of flow of the current [4].

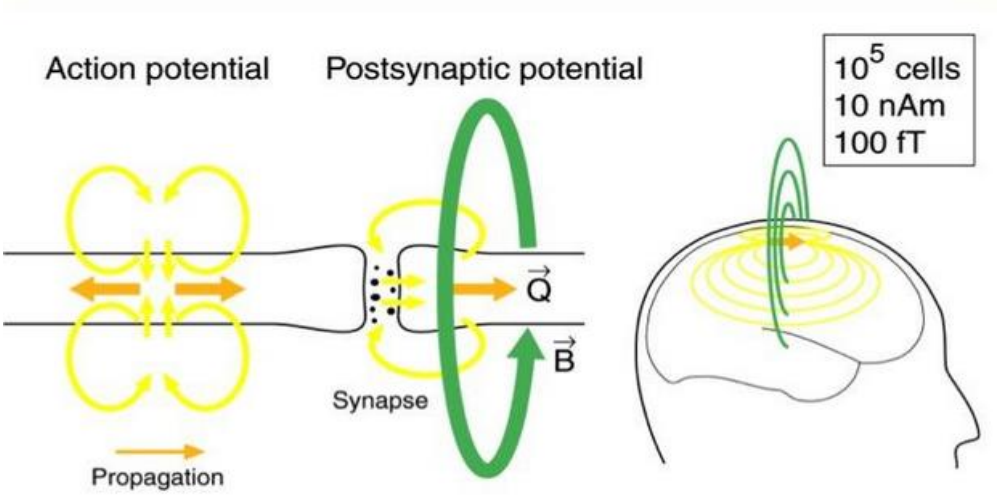

Figure 1.3. Comparison of field propagation in a single neuron and the human brain as a whole. Also, note the current and the magnetic field magnitude involved [5].

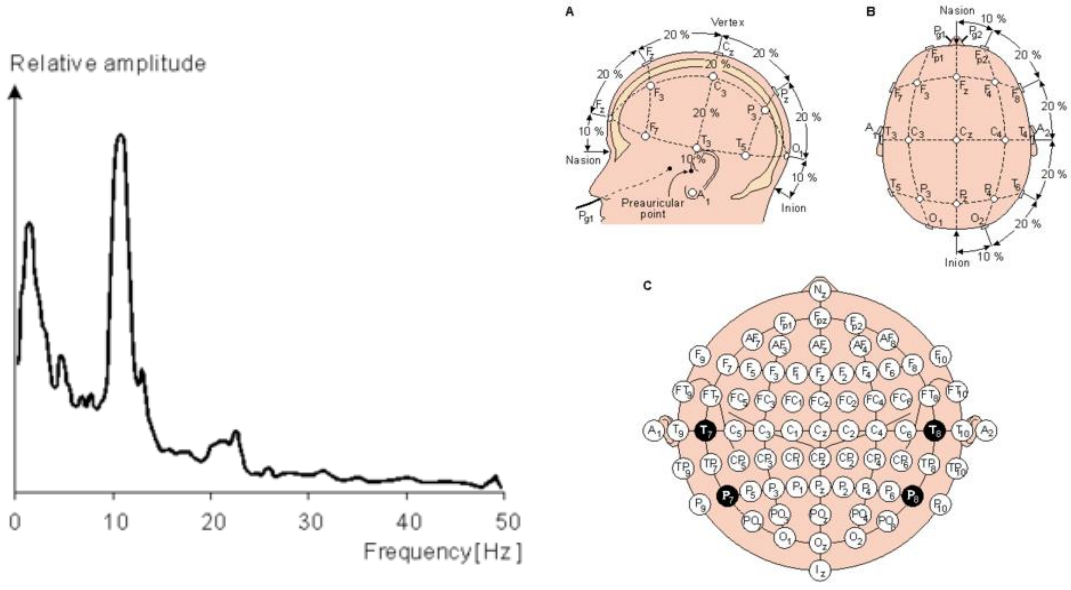

(a) (b)

Figure 1.4. (a) A typical spectral response measured using EEG (b) electrode placement for measurements [24].

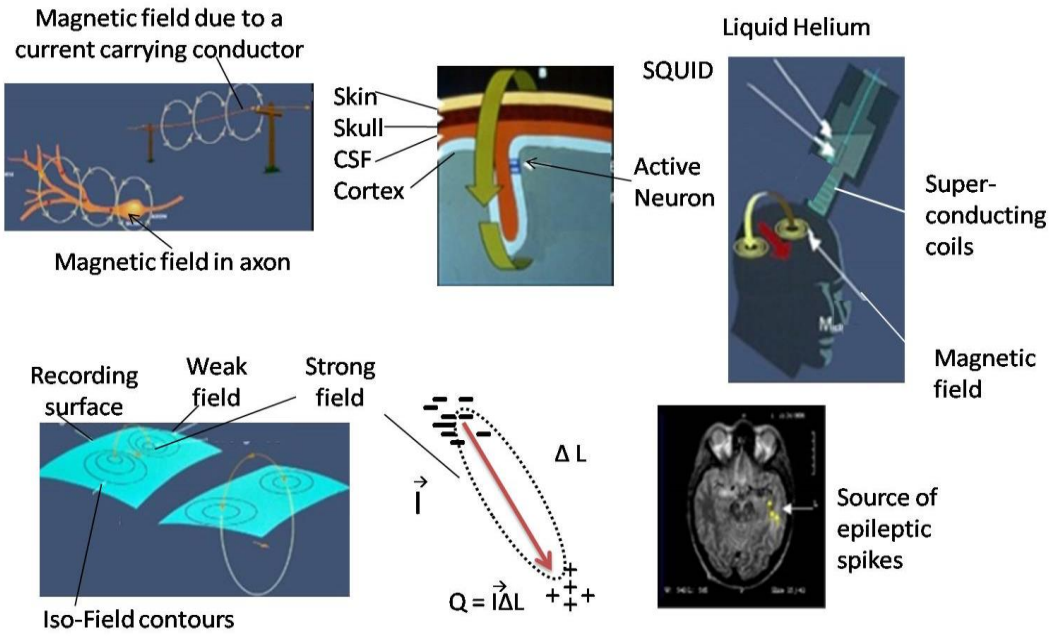

Figure 1.5. Schematic showing working principle of magnetoencephalography [26].

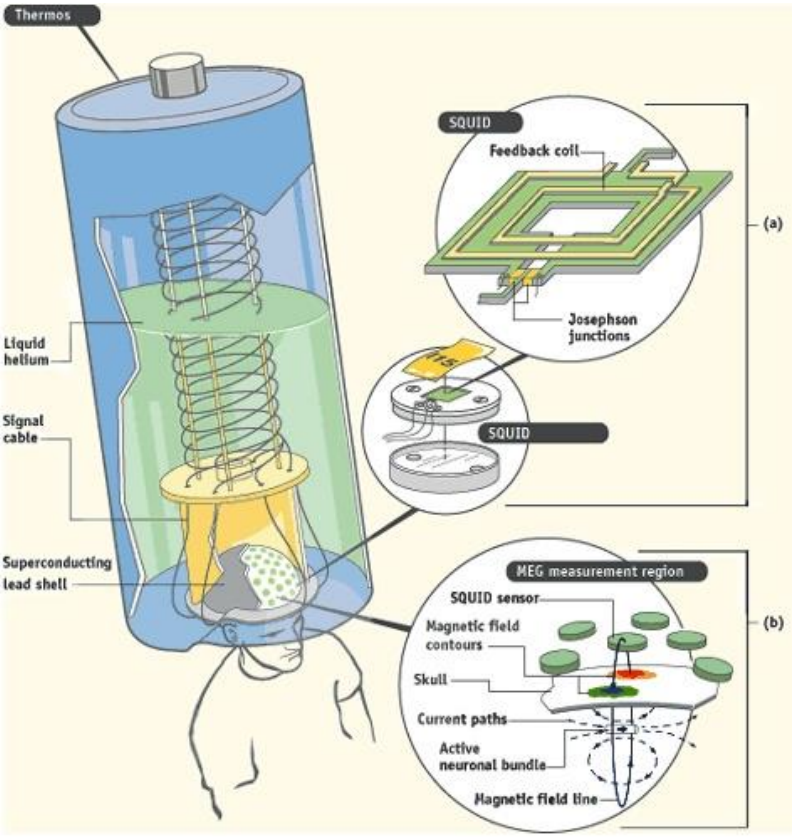

Figure 1.6. Schematic showing the working principle of SQUIDs a type of MEG, with (a) detailed look at the individual sensor (b) positioning of sensors on the human skull [27].

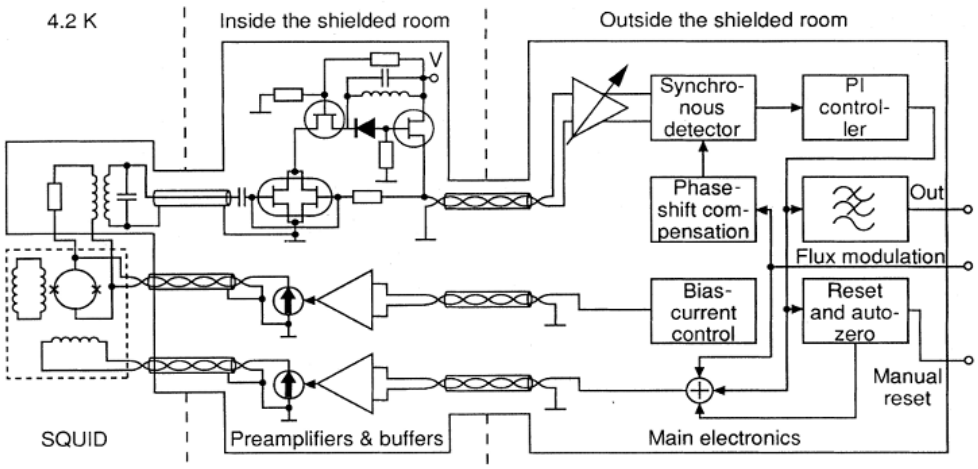

Figure 1.7. Schematic of a DC SQUID's electronics, based on flux modulation and phase sensitive detection [28].

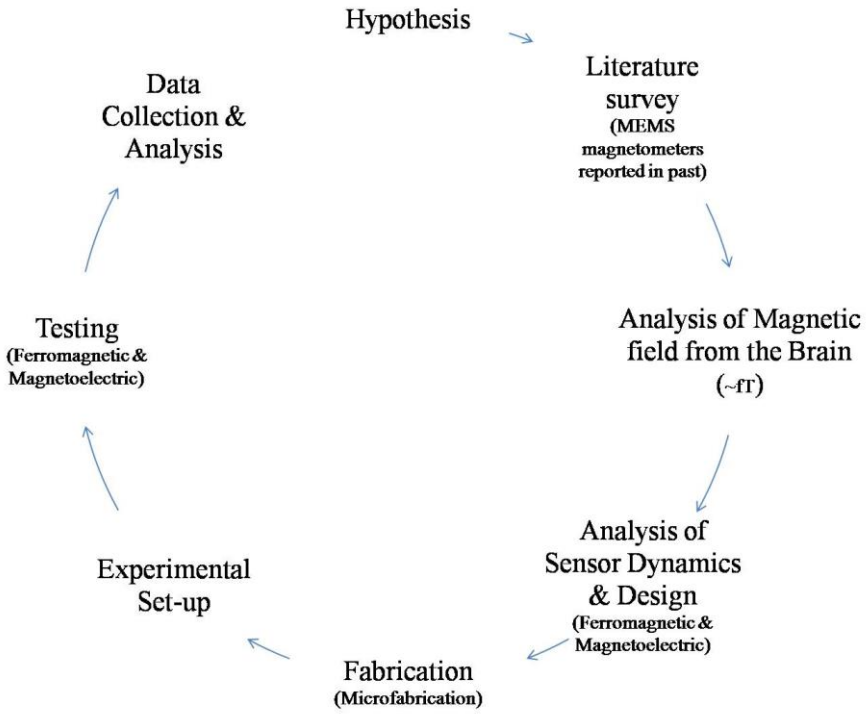

Figure 1.8. The approach used for the ultra-sensitive ferromagnetic (27 pT resolution) and the magnetoelectric (40 fT resolution) magnetometer.

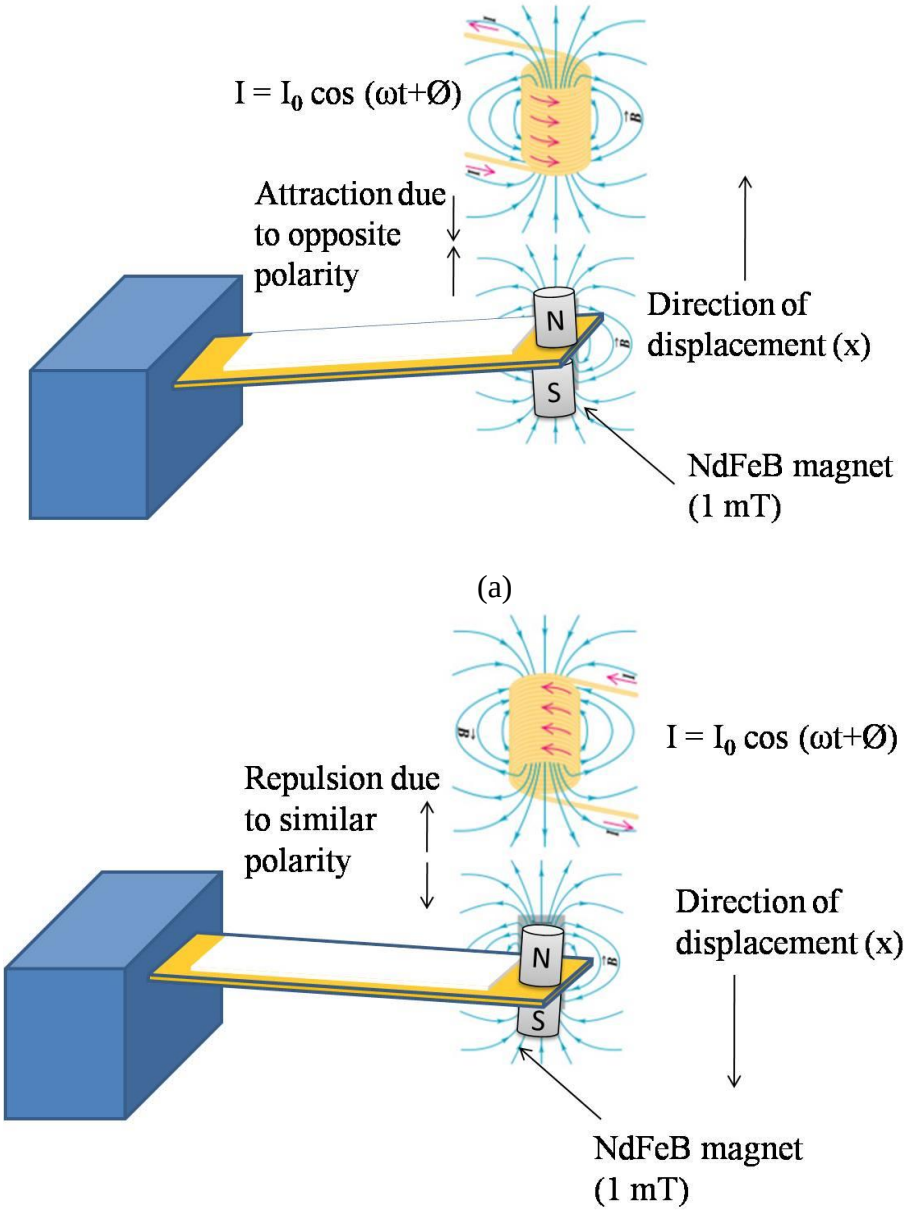

Figure 1.9. Schematic showing the interaction between the magnetic field from the permanent magnet used as a foot-mass on the sensor and the AC magnetic field produced by a coil to either (a) attract (b) repel the flexure.

Table 1.1. Comparison of the sensitivity and the MDS for the MEMS magnetometers reported in the literature.

S.no	Authors	Type	Sensitivity	MDS	Device Dimensions
1.	This work	Ferromagnetic	0.67 mV/nT	27 pT	8000 X 2000 X 1 $(\mu m)^3$
2.	This work	Magnetoelectric	1.63mV/nT	40fT	7000 X 1500 X 1.7 $(\mu m)^3$
3.	Marauska et al. *[30]*	Magnetoelectric	0.0038 mV/nT	30 pT	200 X 900 X 7.8 $(\mu m)^3$
4.	Yabukami et al. *[38]*	GMI	-	88 pT	5000 × 50 $(\mu m)^2$
5.	Kádár *et al*. *[33]*	Lorentz Force	23.7 V^2/mT	1 nT	2800× 1400 $(\mu m)^2$
6.	Bertoldi *et al*.*[35]*	AMR	10 mV/V/ mT	20 nT	1000× 1000 $(\mu m)^2$
7.	Wang *et al*. *[36]*	GMR	2.73 mV/ V/ Oe	30 nT	1400 × 1400 $(\mu m)^2$
8.	Liakopoulos and Ahn *[37]*	Micro-Fluxgate	0.008 mV/nT	60 nT	5000 × 2500 $(\mu m)^2$
9.	Kumar *et al*. *[31]*	Lorentz Force	2.1 mV/nT	0.28 pT	800 X 800 X 1.5 $(\mu m)^3$
10.	Ren et al. *[32]*	Torsional MEMS	0.4 mV/nT	30 nT	400 X 20 X 60 $(\mu m)^3$
11.	Mo Li et al.*[29]*	Torsional MEMS	1.03 $X10^{-5}$ mV/nT	60 nT	1060 X 800 X 30 $(\mu m)^3$

CHAPTER 2

DESIGN AND DYNAMICS OF MAGNETOMETER

In MEMS magnetometers, the sensor structure consists of a flexure and a magnetic region. The magnetic region can be ferromagnetic or a current-carrying coil. Moreover, the ferromagnetic region can be magnetized in the form of a permanent magnet. The external magnetic field (measurand) applies a proportional force to the magnetic region on the flexure causing its mechanical deformation. The deformation of the flexure is measured with a variety of transduction techniques such as capacitive, piezoelectric, optical etc. To maximize the MEMS magnetometer's sensitivity, the flexure deformation should be maximized and a very sensitive transduction technique with very small inherent noise should be used. Magnetometer designs using cantilever beams [30, 39] and toroidal coils [37] have been reported in the literature. In this chapter, we will discuss the sensor dynamics and design. Following that, a brief description of the strategies to improve output from the sensor is discussed in the Section 2.3. Experimental procedures (Section 2.4) will conclude the chapter.

2.1 Structural Dynamics of the Sensor

The dynamics of a MEMS structure [40-42] as shown in Equation (1.1) (Chapter 1), can be modified and represented as Equation (2.1). Damping coefficient, spring constant and mass are the parameters that can be adjusted by the external magnetic field

[43]. The Equation (2.1) provides an expression for the factors affecting the beam dynamics (see Figure 2.1).

$$F = F_0 \cos \omega t + F_1 = M\ddot{x} + b\dot{x} + k_{equv}x \tag{2.1}$$

where '*F*' is the overall force acting on the device, $'F_0 \cos \omega t'$ is the force due to the AC input applied to the coil, '*M*' is the mass of the sensor, $'b'$ is the damping coefficient, '*k*' is the spring constant, and '*x'* is the net displacement. A change in either of the parameter, introduces an additional force term 'F_1' that affects the sensor dynamics. If the displacement of the sensor is represented by $\left(x = x_0 e^{i(\omega t+\emptyset)}\right)$, then differentiating it with respect to time, we can get the velocity ($\dot{x}$) and the acceleration ($\ddot{x}$) terms as:

$$\begin{aligned} x &= x_0 e^{i(\omega t+\emptyset)}, \\ \dot{x} &= i\omega x_0 e^{i(\omega t+\emptyset)} = i\omega x, \\ \ddot{x} &= -\omega^2 x_0 e^{i(\omega t+\emptyset)} = -\omega^2 x, \end{aligned} \tag{2.2}$$

Using the Equation (2.2) in (2.1), if $F_1 \propto \ddot{x}$, then one can see that the effective mass will be modified. This is accomplished by providing a feedback. From the Equation (2.2), $\ddot{x} = -\omega^2 x$, hence, a 180° phase shift will be introduced, that can either increase or decrease the output. On the other hand, if we consider $F_1 \propto b'\dot{x}$, 'b'' being the effective damping coefficient, the resultant damping of the sensor can be manipulated. In this case, since, $\dot{x} = i\omega x$ as shown in the Equation (2.2), a 90° phase shift will be introduced, that can either suppress or amplify the output. A third case occurs when a force is introduced by external biasing. The biasing can be either introduced by a permanent magnet or another coil excited by a DC input source. In our experiments, damping was decreased by using

the -Z polarity of external bias and increased for the reverse polarity, as we will see in the next chapter. The higher the mass of the neodymium (NdFeB) magnet used as a foot-mass, the larger the damping will be. For a large displacement, this parameter needs to be as small as possible, considering $F_3 \propto k'x$, 'k'' being the effective Hooke's constant. Equations (2.1) and (2.2) above tell us about the external force that can be intentionally introduced to improve the output response, apart from the magnet to magnet force seen by the sensor. All the Equations discussed here are valid for both the ferromagnetic and the magnetoelectric magnetometers, as both of them use the force between the two magnets as the sensing principle.

We will now look at the mathematical representation of the force between a permanent magnet and an electromagnet. The relation between the force (F_0) acting on the sensor's foot-mass, with a magnetic dipole '*M´'* and an external magnetic flux density '*B'* (see Figure 2.2) is given by:

$$F_0 = \nabla(\overrightarrow{M'}.\vec{B}) \tag{2.3}$$

In our experiments, the permanent magnet used as a foot-mass of the sensor was placed directly above the coil's geometric center. So now, we can use only the z-component of '*B'* and '*M´'* and replace $'\nabla'$ operator with $'\frac{\partial}{\partial z}'$, neglecting the x and y components. The magnetic flux density (B_s) of a disk-shaped permanent magnet along its axis (z-component) is approximately given by:

$$B_{zmagnet}(surface) = B_s = \frac{\mu_0 M'}{V_m} \tag{2.4}$$

where 'V_m' is the volume of the permanent *magnet* and 'μ_0' ($4\pi\times10^{-7}$ H/m) is the vacuum

permeability. The surface magnetic flux density (B_s) in our devices was around 1 mT. We will now move on to the magnetic field along the axis of a coil with '*N'* turns and radius '*r'*. The magnetic field is given by:

$$B_{zcoil} = \frac{\mu_0 NI}{2} \frac{r^2}{(r^2+z^2)^{\frac{3}{2}}} \equiv \frac{r^3 B_0}{(r^2+z^2)^{\frac{3}{2}}} \quad (2.5)$$

where '*z'* is the distance between the sensor's magnet and the center of the coil, $B_0 = \frac{\mu_0 NI}{2r}$ is the magnetic flux density at the center of the coil. $I = \frac{V_0 \cos(\omega_0 t)}{R}$ represents the current passed through the coil, in series with a resistor (*R)* at radial frequency (ω_0) connected to a voltage source with peak output voltage of 'V_0'. Using the Equations 2.3-2.5, the force on the sensor can be represented as:

$$F_{z-sensor} = \frac{\partial (V_m B_s B_{zcoil}/\mu_0)}{\partial z} = \frac{-3zr^3 V_m B_s B_0}{\mu_0 (r^2+z^2)^{\frac{5}{2}}} \quad (2.6)$$

The negative sign here indicates that the force decreases as a function of the distance from the coil. The force has a '$\frac{1}{z^4}$' dependence. It is easy to see that for B_0*~1 nT, r~5 cm, z~2 cm,* V_m*~1 mm*^{3}*,* B_s*~ 1 mT,* we get *F~1 nN*. So the sensor should be sensitive enough to produce an output voltage above the noise level with *1 nN* force, as proved by simulation in Chapter 3. The displacement of the center of the bridge and the applied force follow the relation: *x~F/k.* So, to have a large displacement (response), we need to have a small spring constant '*k'*.

For our measurements, we used a network analyzer as shown in the experimental set-up in Chapter 3. The magnetic field from the coil was generated using input from the network analyzer, and the output from the sensor was analyzed using the network

analyzer. Since the network analyzer had a lower output limit of 0.07 nT/0.707 mV, we increased the distance between the coil and the sensor (2.5-15 cm), keeping the number of turns (18) and the radius of the coil (Ø=3 cm) constant, to obtain lower magnetic field (~0.1 nT). A calibration curve was obtained using a sensitive magnetometer (RM-100 NanoTesla meter) for the coil's output magnetic field. The sensor sensitivity (*S*) can be defined as:

$$S = \frac{|x|}{|B|} = \frac{|x|}{|F|}\frac{|F|}{|B|} \tag{2.7}$$

where the first part of '*S'* is simply '*1/k'* and the second part (*|F|/|B|)* is related to '*B'* from Equations 2.3-2.6. For the ferromagnetic sensor, the sensor output was obtained using a Laser Doppler vibrometer that produced a signal proportional to the velocity of the bridge (|*dx/dt*|). In the case of the magnetoelectric sensor, the output voltage from the PZT was proportional to the displacement of the beam (*x*) as discussed in Chapter 4. We will now look at the various parameters that affect the sensor design.

2.2 Sensor Design

The parameters that affect the dynamics of the sensor as seen in Section 2.1 are mass, damping coefficient, and spring constant. From Equation (2.7) it was evident that the mass (*M*) and the spring constant (*k*) of the sensor should be kept small. In our case, mass of the permanent magnet mounted on the sensor was much higher than the mass of sensor, hence, that was considered to be the effective mass (12-24 mg). Other parameters were obtained using the resonant frequency and spring constant's mathematical representation. The ferromagnetic MEMS magnetometer characterized, had four different structures, namely: fixed-fixed beam, 3-leg bridge, plus bridge and a diaphragm.

Equation (2.8) provides an expression for the spring constant of the fixed-fixed beam structure [44]:

$$k = \frac{16Et^3w}{\ell^3} \tag{2.8}$$

where *'k'* is the spring constant, '*E*' is the Young's modulus of the material used (Si_3N_4), '*w*' is the width of the beam, 't' is the thickness and $'\ell'$ is the length of the sensor. From Equation (2.8) it is evident that to keep '*k*' low, the thickness has to be kept as small as possible ($k \propto t^3$). Using the MEMS fabrication technique, as explained in Section 3.2, Si_3N_4 thickness of 1 μm was achieved. By reducing the thickness of the sensor, the output can be improved as: *x~F/k*. The width too had to be kept small ($k \propto w$) and to test the same we fabricated some sensors with variable width (1-4 mm). The length was inversely proportional to *'k'* ($k \propto \frac{1}{\ell^3}$) and hence, was needed to be large (6-10 mm). For brain mapping application the sensor resonant frequency should be in the 10-100 Hz range.

$$\omega = \sqrt{\frac{k}{M}} = \sqrt{\frac{16Et^3w}{M\ell^3}} \tag{2.9}$$

'*M*' in the above case is the total mass, but it is limited to the mass of the permanent magnet (12-24 mg) used as the foot-mass. Increasing the mass decreased the resonant frequency by the relation $\omega \propto \sqrt{\frac{1}{M}}$. The other structures used for sensing had a foot-mass at the center, with legs supporting it to the silicon frame (see Figure 2.3). The approach for the spring constant calculation, in this case, was to consider the ends near the foot-mass fixed. Hence, the approximate term for spring constant can be given as:

$$k = \frac{AEt^3w}{\ell^3} \tag{2.10}$$

'*A*' here represents the number of legs that were 3 and 4 in our case. Using these design considerations, the ferromagnetic sensor was fabricated. The effectiveness of the design parameters were pushed to the limit. Using signal improvement strategies, the output from sensor was improved, as discussed in the Section 2.3.

The magnetoelectric sensors characterized were fabricated using piezoelectric discs (Ø 9.9 mm) and shaped in the form of flexure beams. Using the PZT beam Equations (2.11-2.15) the optimum dimensions of the sensor were determined.

$$\mathrm{f} = \frac{\nu_n^2}{2\pi}\sqrt{\frac{0.236\mathrm{D_p w}}{(\ell - \ell_m{}^2)^3(\mathrm{m_e} + \mathrm{m_p})}} \tag{2.11}$$

$$\nu_n = 1.875 \tag{2.12}$$

$$\mathrm{m} = \rho_p t_p + \rho_s t_s \tag{2.13}$$

$$\mathrm{m_e} = 0.236\mathrm{mw}(\mathrm{l} - \frac{\ell_m}{2}) + \mathrm{mw}\frac{\ell_m}{2} \tag{2.14}$$

$$\mathrm{Dp} = \frac{(E_p^2 t_p^4 + E_s^2 t_s^4 + 2E_p E_s t_p t_s (2t_p^2 + 2t_s^2 + 3t_p t_s))}{12(E_p t_p + E_s t_s)} \tag{2.15}$$

where, 'E_p' is the Young's modulus of piezoelectric material, 'E_s' is the Young's modulus of brass, 'ℓ_m'is the length of the foot-mass (1.52 mm), 'ℓ' = 'ℓ_b' is the length of the beam (9 mm), '*w' = 'w_b' = 'w_m'* is the width of the beam, 't_p' is the thickness of piezoelectric material (0.12 mm), 't_s' is the thickness of substrate (0.05 mm), 'm_p' is the mass of the permanent magnet (12-24 mg), 'ρ_p' is the density of piezoelectric material, and 'ρ_s' is the density of brass. Using the parameters mentioned above the PZT disc was cut in different dimensions keeping the length and thickness constant. Thus, the only

parameter that was varied was the width of the sensor. Sensor with different substrate thickness was initially tested, with a 0.05 mm thick substrate giving the best response. We will now discuss the strategies employed to enhance the output from the sensors.

2.3 Strategies to Improve the Sensor Signal

In order to improve the output from the sensor, we used six strategies that will be discussed in this section. Electronics spring constant modification of the sensor will be discussed in the Subsection 2.3.1. We will then look at the use of shielding and concentrators in the Subsection 2.3.2. In the Subsection 2.3.3 theoretical analysis of parametric amplification will be done. Use of coupled resonators to improve the sensor sensitivity, will be presented in the Subsection 2.3.4. Following coupled resonators, we will look at the different noise reduction techniques in the Subsection 2.3.5. The Subsection 2.3.6 concludes this section by discussing how introducing a vacuum improves the sensor response.

2.3.1 Spring Constant Modification

From the Equation (2.2) in the Section 2.1, it can be seen that the displacement of the sensor is a time dependent function of the input signal applied. Subsequent parts of the Equation (1.2) show the dependency of velocity and acceleration on phase. Similarly, the Equation (2.1) shows the force acting on the sensor is a time dependent cosine function of the input frequency. Using the Equations (2.1), and (2.2) an expression for displacement of the device can be represented as shown in the Equation (2.16).

$$x_0 = \frac{F_0/k_{equv}}{\left[\left(1-\frac{\omega^2}{\omega_0^2}\right)+i\left(\frac{\omega}{Q\omega_0}\right)\right]} \tag{2.16}$$

The above Equation gives the amplitude of vibration with its real and imaginary parts. From the Equation (2.16), it can be observed that in order to get a large amplitude (*x*) for a small input force produced by the external bias, the Hooke's constant (*k*) of the device needs to be small. For the denominator to be small, we need the resonant frequency to be small. Since $\omega_0 = \sqrt{\frac{k_{equv}}{M}}$, for a small Hooke's constant, the mass of the device needs to be small too. The quality factor (*Q*) on the other hand $\left(Q = \frac{M\omega_0}{b}\right)$ depends on the damping coefficient The weight of the device in our case was considered same as the magnet mass (12-24 mg), as the magnet mass mounted on the device was much greater than the silicon nitride mass (0.02-0.3 mg).

$$f_0 = \frac{1}{2\pi}\sqrt{\frac{k_{equv}}{M}} \text{Hence, } k_{equv} = M(2\pi f_0)^2 \quad (2.17)$$

where $'f_0'$ is the resonant frequency of the sensor [42]. From the Equation (2.17) it can be concluded that as long as the ratio between '*k*' and '*M*' are kept constant, the 'f_0' will be constant. Note: we now use the term $'k_{equv}'$ and not $'k'$. We only determined the spring compliance variation for the ferromagnetic MEMS sensor. We used a plus-bridge (device #1) for our studies, and it can be schematically represented (see Figure 2.3a.) as a centerpiece hooked by 4 springs, each with a Hooke's constant '*k*', giving an effective Hooke's constant of '*4*k*'. Similarly, for the device #2, the 3 legs of the sensor would account for an effective Hooke's constant of '*3*k*' (see Figure 2.3b). The amplitude of displacement ($|x_0|$) can be represented by the Equation 2.18. To achieve higher sensitivity, $\left|\frac{x_0}{F_0}\right|$ needs to be as large as possible. For a low value of magnetic field (B_{ext}), the equivalent force too will be small. Hence, the Hooke's constant needs to be small.

$$|x_0| = \frac{F_0/k_{equv}}{\left[\sqrt{\left(1-\frac{\omega^2}{\omega_0^2}\right)^2+\left(\frac{\omega}{Q\omega_0}\right)^2}\right]} \tag{2.18}$$

$$\emptyset = \tan^{-1}\left[\frac{\left(\frac{\omega}{Q\omega_0}\right)}{\left(1-\frac{\omega^2}{\omega_0^2}\right)}\right] \tag{2.19}$$

The above Equation relates the phase of vibration to the resonant frequency (ω) and quality factor (Q). Now, as seen in the Section 2.2 using the Equations (2.8-2.10) spring compliance control is possible by design, but limited to the choice of material and foot-mass. Hence, the $'k_{equv}'$ term can be checked if an external force on the center mass levitates the whole sensor, thereby changing the overall force acting on the sensor (reducing/increasing) according to the polarity. From the Equation (2.1) if there is no input given to the coil, the force on the sensor is $F = Mg$. When an external bias is applied, it can either pull or push the magnet on the sensor, used as a foot-mass. The force between two magnets [45] is given by (F_{mm}):

$$F_{mm} = \frac{\pi\mu}{4} M'^2 R^4 \left[\frac{1}{z^2} + \frac{1}{(z+2h)^2} - \frac{2}{(z+h)^2}\right] \tag{2.20}$$

where 'M'' is the magnetization of the permanent magnets, 'z' is the distance between them, 'R' is the radius of the magnets, and 'h' is the height of the magnets. The effective dipole moment (m) of the magnet given by $m = M'V$, 'V' is the volume of the magnet. Hence, the total force on the sensor becomes $'F \pm F_{mm}'$. The pull-down force due to the magnet mass and built-in-stress resulted in the effective compliance of 'k_0' (see Figure 2.4a). We used external bias of varying flux densities (+28.75 mT to -28.75 mT) to study the effect on the sensor amplitude. The output increased for one polarity of the external

bias with a decrease in the resonant frequency, and a reverse effect on both the parameters ('k' and 'M') was observed for the opposite polarity. $K_1 < K_0$ (see Figure 2.4b) resulted in the levitation of the magnet placed on the device. Since, the magnet was attached to the silicon nitride bridge, the whole structure was levitated, relieving it of the built-in stress effect. On the other hand, for $K_2 > K_0$, as seen in Subsection 3.5.2.1, resulted in reduced amplitude. Due to the external magnet either levitating the device or putting it under more stress, determined by the polarity, the effective spring constant was either increased or decreased (see Figure 2.4). The equivalent value of spring constant 'k'', was also decreased by removing a leg of the plus bridge (see Figure 2.3b), resulting in a reduced resonant frequency and a much larger amplitude.

2.3.2 Shielding and Concentrators

To minimize the effect of stray magnetic fields in our measurements, we used high permeability sheets (80% nickel, 15% iron, and 5% molybdenum alloy). A magnetic shielding material works by redirecting the magnetic field away from the shielded item. The magnetic field is not eliminated or destroyed by using high-Mu sheets, but a more feasible path is provided to complete the loop. We can quantify shielding using a relation between the magnetic flux density and the thickness of the shielding material [46].

$$B_{shield} = \frac{DB_0}{\mu t} \tag{2.21}$$

where 'B_{shield}' is the magnetic field density of the shield material, 'D' is the diagonal length or diameter of the shield, 'μ' is the permeability of the material, 'B_0' is the magnetic flux density to be shielded, and 't' is the thickness of the shield. The ratio of the

input magnetic field to the magnetic field shielded is termed as 'attenuation' (A= $\frac{B_0}{B_{shield}}$). Thus, higher the thickness of the shield or more the number of shield layer ($B_{shield} \propto \frac{1}{t}$), higher will be the attenuation ($A \propto t$).

High-Mu sheets were used as the base of the overall set-up. A high-Mu sheet (0.006" thick) in the shape of a cone was also placed directly above the sensor. An increase in attenuation is possible by the use of multiple high-Mu sheets (see Figure 2.5). A small opening was provided at the top, for the laser to reflect from the ferromagnetic MEMS magnetometer. The small opening, acted as a concentrator as well and allowed maximum magnetic field lines to fall on the sensor, enhancing the output. In the case of the magnetoelectric magnetometer, the whole experimental set-up was enclosed in a 25 cm × 25 cm copper (0.125") box. The use of copper, helped in shielding the radio frequency (or RF), which typically is the frequency level above 100 KHz. Copper has a high conductivity, and little or no magnetic permeability that shields RF. The copper plates were wrapped with high-Mu sheet (0.006" thick). There was an improvement in the magnetic noise detected by the sensor, due to shielding (~37%) for the magnetoelectric sensor. An increase in the input magnetic field increased the attenuation making the shielding more effective. We, however, used only a single layer of high-Mu sheet for shielding.

2.3.3 Parametric Amplification

For parametric amplification, we developed a feedback loop that produced a 90^o out of phase signal (see Figure 2.6) with respect to the sensor's output, at the resonant frequency. The parametric amplification works by redirecting the output from the sensor

to a secondary coil (Ø=5.5 cm) placed right above the sensor. The gain of this input is varied to achieve maximum output. The phase of the signal fed to the secondary coil plays a significant role in determining the band-pass selection, to maximize the amplitude of vibration. The secondary force term 'F_1' in the Equation (2.1), will amplify or suppress the output amplitude, depending on the phase and gain of the input to the secondary coil. The magnetic field sensed by the sensor will now have an added component ($B_{feedback}$). This changes the force ($F_{z-sensor}$) and amplifies the sensor response.

$$F_{z-sensor} = \frac{\partial(V_m B_s[B_{zcoil} + B_{feedback}]/\mu_0)}{\partial z} \tag{2.22}$$

The effective current producing this magnetic field ($I = \frac{V_0 \cos(\omega_0 t)}{R} + \frac{V_{out} \cos(\omega_0 t + \emptyset)}{R}$), is manipulated by the output from the sensor (V_{out}) and a phase component ($\emptyset$) is introduced. The gain of this signal was varied to achieve the highest possible sensor output while maintaining its stability. In our experiment, by passing the laser vibrometer output through a pre amplifier, we generated the parametric feedback signal. The signal was then provided to the second external coil with larger diameter (Ø=5.5 cm), as shown in the experimental set-up in the next chapter. By adjusting the band-pass characteristic of the Preamplifier, we introduced a 90^o phase shift in the output of the Preamplifier (see Figure 2.6), which in turn excited the larger secondary coil. The band-pass frequency used in our case was 100 Hz.

2.3.4 Coupled Resonators

Coupling can be of numerous types. Mechanical, electrostatic and magnetic are few types of coupling that helps in enhancing the output from the sensor and reducing its noise. The effect of non-linear elasticity on the coupling between bulk modes of a MEMS resonator was shown by Yang et al. [48]. They used two modes for studying the effect of coupling: driving mode and a detection mode. They argued that due to the strain induced in one of the resonators; a nonlinear coupling mode can be achieved, that in turn affects other modes. Xu et al. [49] demonstrated a strongly mechanically coupled bulk Lame-mode, silicon-based, MEMS resonator using a piezoresistor as the coupling spring. They achieved a 28 dB increase in transduction preserving the quality factor of 10^6. Erbes et al. [50] demonstrated three different mechanical coupling schemes, including 1D, cyclic and cross coupling in silicon resonator. They used coupling to study variation in motional resistance. A nine resonator system was used, that helped achieve 2.7 times improvement in mean motional resistance. They also studied the vibration of a mechanically coupled, double-ended tuning fork resonator [51]. A -25 dBm input was given to the DC grounded body, whereas the sensor electrodes used a +9 V DC voltage bias. The quality factor obtained for the two was 33083 and 31372.

Umesh et al. [52] demonstrated capacitive coupling on a fixed-fixed beam resonator. An AC signal was applied to the resonating beam, whereas the fixed beam was actuated using a DC voltage. A quality factor of 14000 was achieved using this coupling mechanism. For capacitive coupling, the DC voltage creates the electrostatic actuation whereas the AC signal produces oscillation. An energy-based mode shape sensitivity analysis, was done for a coupled symmetric resonant system by Manav et al. [53]. At

higher degrees of mode localization, the sensitivity to nonlinearity was found to be higher. Higher sensitivity to nonlinearity was due to lower coupling strength.

Apart from the electrical and mechanical coupling, magnetic coupling too has been demonstrated. Pai et al. [54] demonstrated mode localized magnetically coupled resonators. They used a neodymium magnet as the foot-mass on the resonators which produced the coupling. To set the sensor in motion, electrostatic transduction was used. They used one of the resonators as the driver, and the other as the sensor. The output from each resonator was determined both in the sense and drive mode. Spletzer et al. [55, 56] fabricated an array of mechanically coupled resonators and argued having achieved two to three orders magnitude shift in Eigen function. Manufacturing two identical structures in a resonator is difficult. However, the small variation in structure plays a vital role in determining the variation in Eigenstates through coupling [56]. Our aim was to improve the sensitivity of the sensor using mode-localized resonators. The identical resonators with permanent magnet, interacted with the magnetic field from the coil, to produce the electromagnetic coupling (see Figure 2.7). The magnetization components of the resonators (M_1 & M_2) along with the electrical field components (E_1 & E_2) gave the

$$C_c = \frac{\iiint \varepsilon E_1 E_2 dv}{\sqrt{\iiint \varepsilon |E_1|^2 dv \times \iiint \varepsilon |E_2|^2 dv}} + \frac{\iiint \mu H_1 H_2 dv}{\sqrt{\iiint \mu |H_1|^2 dv \times \iiint \mu |H_2|^2 dv}} \quad (2.23)$$

coupling coefficient (C_c). In Equation 2.23; 'C_c' is the coupling coefficient, 'ε' is the relative electrical permittivity, ' E_1& E_2' are the electrical field strength component of the resonators per volume, 'μ' is the relative magnetic permeability, and 'H_1 & H_2' are the magnetic field strength component of the resonators per volume [57]. The first part of the Equation gives the electrical coupling ($\frac{\iiint \varepsilon E_1 E_2 dv}{\sqrt{\iiint \varepsilon |E_1|^2 dv \times \iiint \varepsilon |E_2|^2 dv}}$) and the second part

represents the magnetic coupling ($\frac{\iiint \mu H_1 H_2 dv}{\sqrt{\iiint \mu |H_1|^2 dv \times \iiint \mu |H_2|^2 dv}}$). The magnetic field strength of the permanent magnets (H_1 & H_2) can be represented in terms of the magnetization (M_m) and the magnetic flux density (B_m) using [58]:

$$B_m = \mu(H_m + M_m) \tag{2.24}$$

With an increase in gap between the resonators the effective 'B_m' magnetic field strength of the permanent magnets used, decreased. As $C_c \propto H_m \propto B_m$, the coupling between the resonators decreased.

The effective spring constant of the sensor varied because of coupling and affects the output (see Figure 2.8). The amplitude of the sensor in common mode was reduced, whereas in the opposite mode of vibration, it improved the amplitude by 2-5 times as shown by other groups [48-57]. The sensors used for the coupled-mode response needed to be similar. Figure 2.8 shows the underlying principle used for the coupled sensor. The mass m_1 and m_2 (see Figure 2.8) were required to be as close as possible. For anundamped response, the coupled system can be represented as:

$$m\ddot{x_1} + kx_1 + k_c(x_1 - x_2) = 0 \tag{2.25a}$$

$$m\ddot{x_2} + kx_2 + k_c(x_2 - x_1) = 0 \tag{2.25b}$$

We tested the coupled mode response for the magnetoelectric magnetometer. We considered the mass of the permanent magnet (0.12 gm) as the effective mass of the sensor, i.e., $m_1 = m_2 = m$ = 12 mg. Apart from mass being the same, the spring constant of the two needed to be the same. Hence, $k_1 = k_2 = k$. 'K_c' here represents the coupled mode effective spring constant of the sensor. Keeping the dimensions of the individual

sensors similar, we were able to match the two spring constants. As the mass and the spring constant of the two sensors were same, the resonant frequency of the two sensors was very close to each other ($\omega_1 \approx \omega_2$). We used permanent magnets (NdFeB) on the two resonators for magnetic coupling. Using Equations 2.25a and 2.25b, the in-phase and out-of-phase response of the coupled mode resonator can be understood. The coupled-mode helps in eliminating the effect of external vibration, and variation in temperature and pressure.

2.3.5 Noise Reduction Techniques

To control noise in the sensor two techniques were employed: active and passive. Active noise reduction curbed noise by the use of parametric amplification (electronics) and will be discussed in the next chapter. The noise-floor for the two cases (active and passive) was measured at frequencies away from the resonant frequency. The calculation used for determining the minimum detectable signal (MDS) of the sensors, depended extensively on the noise-floor for the ferromagnetic MEMS magnetometer. For passive noise reduction, a vibration isolation workbench was used. The output from the oscilloscope was used to study the difference between the noise-floor for different cases. The output as seen on the oscilloscope decreased continuously with better techniques. The cases that we used for noise analysis were: the vacuum pump in ON/OFF state, shielding using high-Mu sheet, and use of TS-150 for vibration isolation (see Figure 2.9). The whole experimental set-up was on the pneumatic isolation system. The advantage of using a magnetoelectric magnetometer over ferromagnetic is the elimination of the optical detection method. We also observed the remarkable reduction in the noise-floor (~10 times) while using the piezoelectric transduction (for the magnetoelectric

magnetometer) (see Figure 2.10). There was a reduction in the noise level due to shielding (~38%) and the vibration isolation system added (~18.5%) to the experimental set-up. For electronic (active) noise control, the output from the laser was provided to a coil of larger diameter (Ø=5.5 cm) as shown in the experimental set-up in the next chapter. Output was measured for two different inputs 0.07 nT (0.707 mV) and 0.8 nT (7.07 mV). Active noise control method helped in improving the amplitude of vibration as well as reducing the noise-floor (see Figure 2.9a). The Figure 2.9a shows a decrease in amplitude when the vacuum pump was switched OFF, as the vibration from the vacuum pump adds not only to the sensor amplitude but to the noise-floor as well. A reduction in 3 mV of noise was achieved at each step, as measured using the oscilloscope. In the next section, we will look at the advantage vacuum brings in the dynamics of the sensor.

2.3.6 Vacuum

The density of air is ~1.225 kg/m^3 at sea level at 15 ˚C. As we know, air is comprised of tiny particles that dampen the motion of the flexure structure. We used vacuum to reduce the effect of damping and acoustic coupling. From Equation (2.1) it can be seen that introducing a vacuum reduces the factor 'b' thereby increasing the overall sensitivity of the sensor ($S = \frac{|x|}{|B|}$, *and* $\dot{x} \propto \frac{1}{b}$). A vacuum was introduced in the vacuum chamber, containing the sensor, to increase the quality factor (Q) of the sensor by reducing the damping coefficient (b).

$$Q = \frac{M\omega_0}{b} = (2\pi)^{\frac{3}{2}} \frac{M}{A_e} \left(\frac{g_0}{s}\right) \sqrt{\frac{RT}{M_m}} \frac{1}{P} \tag{2.26}$$

where 'M' is the mass of the sensor, 'ω_0' is the resonant frequency of the sensor, 'b' is

the damping coefficient, 'M_m' is the molar mass of air, 'P' is the ambient pressure, 'A_e' is the area of the electrode, 'g_0' is the gap between the electrodes, 's' is the perimeter of the electrode, 'R' is the universal molar gas constant (8.31 kg $m^2/(s^2K)$, and 'T' is the temperature. By introducing a vacuum (1 mTorr), we reduced the factor 'P'. As, $P \propto b$, a reduction in the ambient pressure reduced the damping coefficient (b).

Due to the inverse relation between the damping coefficient and the quality factor $b \propto \frac{1}{Q}$, there was an increase in the quality factor of the sensor. The output of the ferromagnetic MEMS magnetometer was increased by two times, when the sensor was subjected to 1 mTorr (Atmospheric pressure = 1 Torr) pressure inside an aluminum sample holder with an optical window. The optical window allowed the laser from the Laser Doppler vibrometer to reflect from the sensor for output measurement.

2.4 Experimental Procedures

The choice of material for sensor fabrication depends on the Young's modulus and density component as shown in the Equations 2.8-2.15. We used silicon nitride (Si_3N_4) for the ferromagnetic MEMS magnetometer supported by a silicon frame, as we will see in detail in the next chapter. To fabricate the magnetoelectric magnetometer, piezoelectric discs (Ø 9.9 mm) were shaped to form the beams (detailed in Chapter 4). A rare earth neodymium (NdFeB) magnet was used as a foot-mass, to enhance the sensitivity of the sensor. High-Mu sheets (0.006") were used attached to thick copper plates (0.125") of dimension 25 cm × 25 cm, to reduce the effect of stray magnetic fields. Coils made out of copper were used to produce the excitation magnetic field (Ø=3 cm) and a parametric feedback signal (Ø=5.5 cm). A plexy-glass frame was used to support the coils (see Figure 2.11). Nonmagnetic connectors were used to assemble the Laser-Doppler

vibrometer system. Agilent Network/Spectrum/Impedance Analyzer (4395A) was used to study the spectrum and provide the excitation input. Polytec Laser Doppler Vibrometer was used to sense the resonance from the ferromagnetic MEMS magnetometer. A signal generator (BK Precision 4052) was used to produce higher magnetic field from the coil to optimize the placement of the permanent magnet on the sensor right at the center of the coil. The TS-150 and the Newport pneumatic isolation systems reduced the effect of vibration. Preamplifiers (SR-560) were used for impedance matching and selecting band-pass frequency ranges for the parametric amplification.

The coil (Ø=3 cm) used to produce the low magnetic field, was calibrated using a highly sensitive RM-100 NanoTesla meter (see Figure 2.12). The coil was placed in the shielded copper box to eliminate the effect of stray magnetic field. Since, the input to the coil was AC, output from the coil was analyzed using an oscilloscope as well as a network analyzer. The input was maintained at 510 Hz, away from the 60 Hz harmonics. The range (0.1-100 μT) of the equipment was varied with the level of magnetic field to be detected. The calibrated output was then extrapolated to give lower values of magnetic field. However, for calibration using the network analyzer, the minimum input to the coil was 0.707 mV, which was sufficient to reach the detection limit (0.1 nT) of the instrument. The detection limit of the instrument was limited to 0.1 nT. A different range was selected (0.1 to 100 μT) to determine the magnetic field from the coil.

2.5 Transduction Techniques

The output from a sensor can be measured in a number of ways, depending on the parameters (resistance, capacitance, temperature, etc.) that vary with time. The material used in the fabrication of the sensor also determines the transduction technique that can

be used. Various other techniques such as capacitive and optical can be used for the detection of small variation in the output. Superconductivity is used in SQUIDs as seen in Chapter 1; using the current induced in the pickup coil, a changing magnetic field can be detected. By vibrating a magnetic material in the vicinity of a coil, current can be generated. Piezoelectricity, magnetostriction, the Hall Effect [32], AMR [33], GMR [34], magnetoresistive effect [35, 36], flux gate [37], magnetoelectric [30], and the Giant magneto-impedance effect (GMI) [38] have been used to transduce magnetic field variation to electrical signals. In our experiment, we used three different transduction techniques, namely: optical, piezoelectric, and magnetostrictive.

2.5.1 Optical Transduction

The ferromagnetic MEMS magnetometer was characterized using a Laser-Doppler vibrometer system. A 633 nm laser was used at a range of 5 mm/s/V. The maximum frequency range of the system was set at 100 KHz and the tracking filter was set at 'slow'. Since the resonant frequency to be measured was below 5 KHz, the lowest value of low pass filter (LPF) was used (5 KHz). The Laser-Doppler vibrometer is an optical transducer capable of determining the vibration velocity as well as displacement. The principle behind the transduction is the "Doppler effect" [59]. According to this principle, a wave reflected from a resonating object results in a change in frequency (Δf) and can be represented by:

$$\Delta f = 2\,\frac{v}{\lambda} \tag{2.27}$$

where 'v' is the velocity of the object and 'λ' the wavelength of the emitted wave. To measure the frequency shift, the laser beam is split into two. One of the beams

(measurement beam) is incident on the resonator and the other acts as a reference (reference beam). Any variation in the object's position, produces a change in the interference pattern. The modulation frequency of the interference pattern is proportional to the velocity of the object and can be determined by the vibrometer. The output from the Laser Doppler in our case was given to the network analyzer and recorded.

2.5.2 Piezoelectric Transduction

The magnetoelectric sensor used the "piezoelectric effect" as the transduction technique. Piezoelectricity is the process by which charge is produced in a certain material (PZT, Quartz, etc.) when an external mechanical stress is applied. It is a reversible process and hence the application of a voltage difference across the material brings a deformation.

$$Piezo\ coefficient\ = \frac{mechanical\ input}{electrical\ output} \tag{2.28}$$

$$D\ = \in E \tag{2.29}$$

where '*D*' is the electric displacement, $' \in '$ is the permittivity of the material and '*E*' is the applied or generated electric field. Thus, from Equation (2.29) the voltage output can be calculated ($E = V/t$) for a PZT of thickness '*t*'. The electrical displacement (*x*) in the case of the magnetoelectric sensor and displacement in the ferromagnetic MEMS magnetometer is produced due to the magnetostrictive transduction that is discussed in the next section. Other techniques such as the capacitive and the piezoresistive transduction, will also be discussed to sum up the important transduction techniques used in research.

2.5.3 Magnetostrictive Transduction

Magnetostriction is the property of the ferromagnetic materials by which there is a change in its shape or dimension, when an external magnetic field is applied.

$$magnetostriction = \frac{magnetic}{mechanical} \tag{2.30}$$

Magnetostriction was used by both the ferromagnetic MEMS magnetometer and the magnetoelectric magnetometer. The magnet-magnet force brought about a displacement in the flexure structure. The inputs to the inner coil (Ø=3 mm), placed at a distance (2-4.5 cm) from the permanent magnet on the sensors, produced the magnetic field. This exerted a force (attractive/repulsive) on the permanent (NdFeB) magnet placed on the sensor. The resultant displacement was then transduced to an electrical output using the piezoelectricity or the optical transduction.

2.5.4 Capacitive Transduction

Capacitive transduction has been widely used in the magnetic field detection. A change in the dielectric permittivity of the material, the area of the electrode or gap between the electrodes is used to measure the change in capacitance. Zyatkov et al. [60] used change of the capacitance of an active dielectric (ferrofluid) due to the magnitude of magnetic field. The capacitive element from the ferrofluid changed the sensitivity with different dispersion of magnetic particles. They, then determined the threshold of the sensitivity and the sensitivity of a measuring cell with ferrofluid by a changing magnetic field.

$$C = \frac{\varepsilon\varepsilon_0 A}{d} \tag{2.31}$$

In the Equation 2.31, 'A' is the area of electrodes, 'd' is the distance between electrodes, 'ε_0' is the dielectric constant of free space, and 'ε' is the dielectric permeability of the medium filling the space between the plates. They measured the sensitivities of 0.47 fF/μT for the parallel orientations of the external magnetic and electrical fields between the electrodes and 0.14 fF/μT for the perpendicular orientations of the external magnetic and measuring the electrical fields. Ahmad et al. [61] proposed a CMOS MEMS resonant, magnetic field sensor, with a differential electrostatic actuation and capacitive sensing. Their device had an overall dimension of 780 μm × 660 μm with a thickness of 45 μm. This formed the main sensing structure and using Equation 2.31 the output was calculated. Stifter et al. [62] demonstrated a Lorentz force actuated magnetic field sensor using capacitive transduction. They fabricated a U-shaped cantilever actuated using an AC source (Vac) along with a polarization DC bias (Vdc). The change in capacitance ($\frac{dC}{dt}$) was used to sense the force (F) due to an external magnetic field.

$$F = \frac{1}{2}\frac{dC}{dt}(V_{ac} + V_{dc})^2 \tag{2.32}$$

Thus, capacitive transduction too can be used as an effective transduction mechanism as shown in the literature.

2.5.5 Piezoresistive Transduction

A change in the electrical resistance of certain material (amorphous/polycrystalline silicon, germanium, nickel, etc.) when subjected to an external mechanical stress is termed as the "piezoresistive effect". The change in resistance can be induced by an external magnetic field, direct force or pressure. The piezoresistive coefficient (ρ_σ) can

be related to the change in resistance ($\frac{\Delta R}{R}$) and the strain induced in the material ($\epsilon = \frac{\Delta L}{L}$) as:

$$\rho_\sigma = \frac{\frac{\Delta R}{R}}{\epsilon} \tag{2.33}$$

$$R = \rho \frac{L}{A} \tag{2.34}$$

where 'L' is the length of the piezoresistive material, 'A' is the area of the piezoresistive material, 'ρ' is the resistivity, 'ΔR' is the change in resistance, and 'R' is the initial resistance. Using Equation 2.33 and 2.34 the change in resistance can be estimated. Liu et al. [63] used piezoresistive microcantilevers to sense the magnetic field. A thin film nickel was used as the piezoresistive material. A change in resistance of 2.6 Ω was recorded for an 18 mT external magnetic field. Beroulle et al. [64] used a U-shaped cantilever actuated by Lorentz force to sense external magnetic field. Using the technique, a maximum change in resistance ($\frac{\Delta R}{R}$) of 800 Ω was demonstrated when a 110 mT magnetic field was applied.

Apart from the transduction techniques mentioned above, other techniques that can be used are magneto-impedance effect, and magnetoelectric effect, etc. Magneto-impedance is a large variation in the electrical parameter (real and imaginary component) of some material (FeCoSiB, FeSiB, etc.) in the presence of a changing magnetic field. Tan et al. [65] used the magneto-impedance effect integrated with a thin film permanent magnet to sense the bias field. They used $Co_{85}Nb_{12}Zr_3$ as the resistor and measured the variation in impedance (Z) for different magnetic field inclination. When an external electric (or magnetic) field induces magnetic (or electric) polarization in a material (Cr_2O_3,

multiferroics, etc.) it is called the “magnetoelectric effect”. Kiser et al. [66] used the magnetoelectric effect in doubly clamped ferromagnetic magnetostrictive Metglas resonators. The electrical and magnetic frequency response in their case was reconfigurable. A change in uniaxial stress due to magnetostrictive strain induced a change in resonant frequency. Using the same material, metglas ribbons, Gillete *et al*. [67] achieved a zero bias sensitivity of 7.43 mV/Oe under a reference magnetic field of 10 mOe. The magnetoelectric material was attached to a piezoelectric tube to increase strain generation.

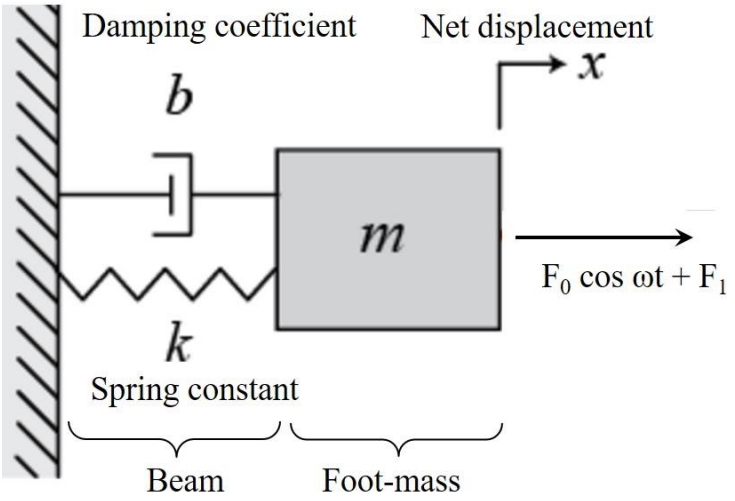

Figure 2.1. Schematic showing the sensor with the parameters affecting its dynamics.

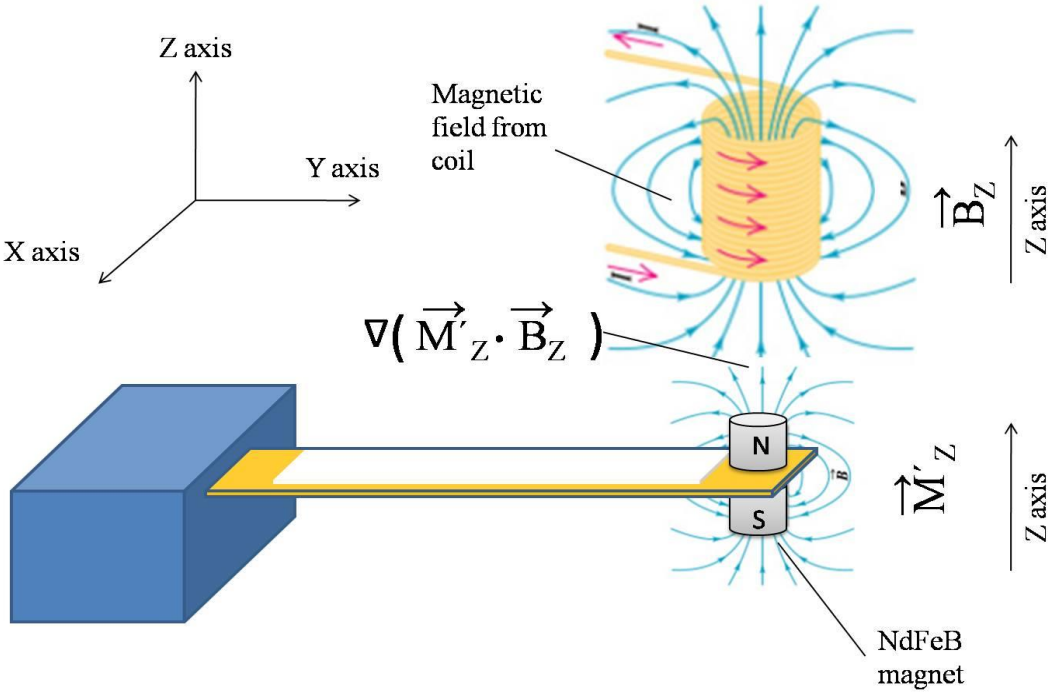

Figure 2.2. Schematic showing the interaction between the magnetic field (B) produced by the coil and the permanent magnet (M´) used as a foot-mass.

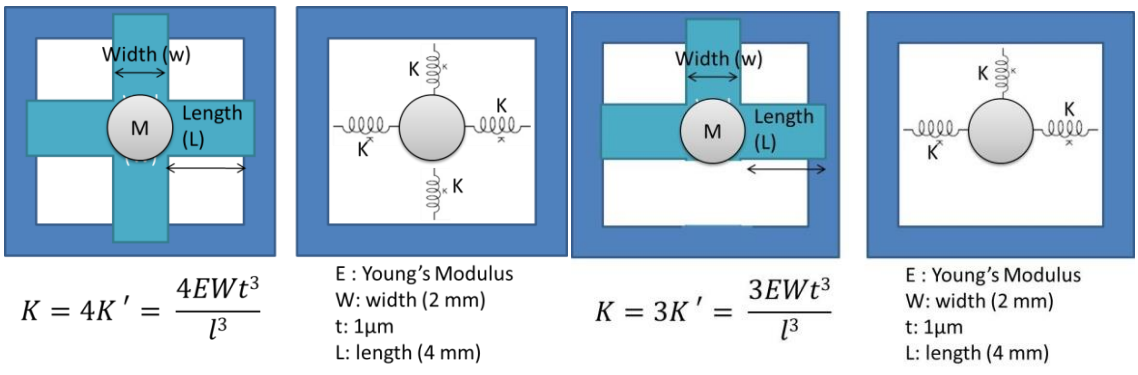

(a) (b)

Figure 2.3. Representation of the ferromagnetic MEMS sensor (a) device #1 (b) device #2 showing the effective Hooke's constant.

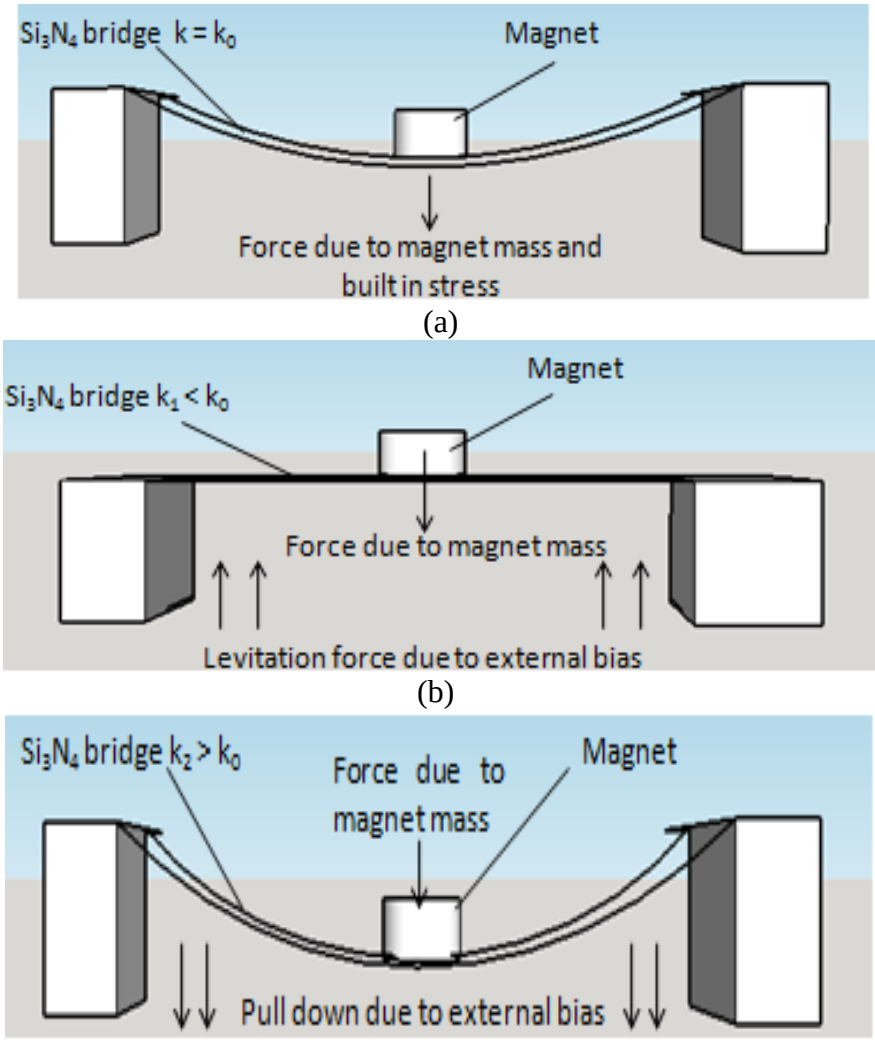

Figure 2.4. The effective force on the ferromagnetic MEMS sensor subject to (a) no external bias (b) +13.75 mT (c) –13.75 mT bias.

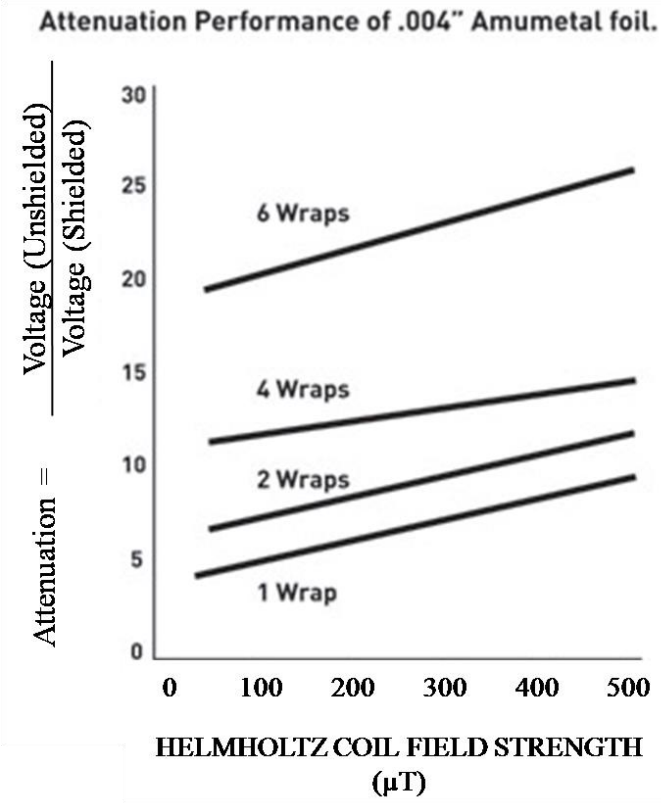

Figure 2.5. Graph showing improvement in attenuation by increasing high-Mu sheet thickness [47].

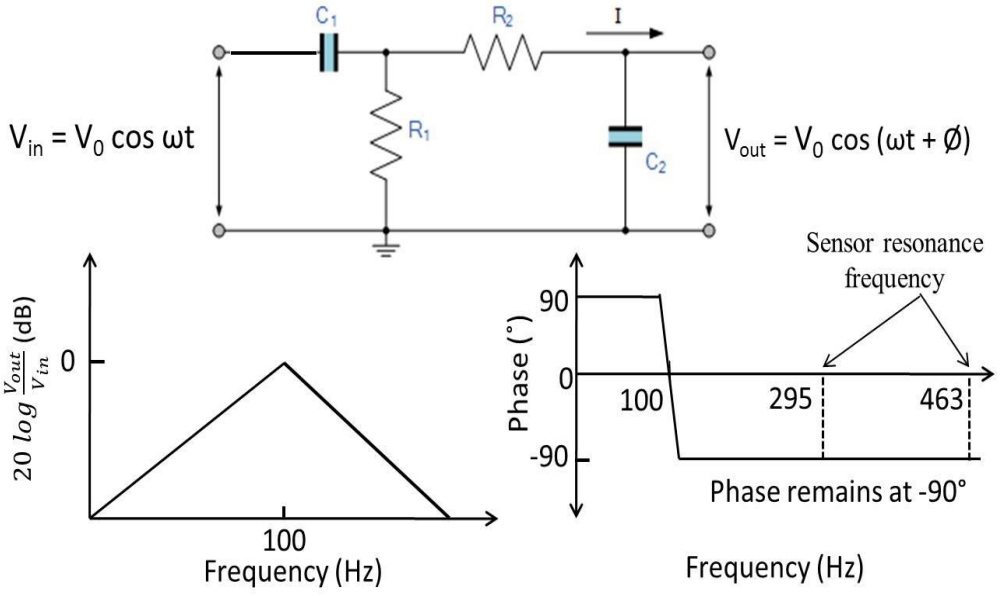

Figure 2.6. Representation of the principle of operation used in parametric amplification. We optimally selected the band-pass frequency for maximum output.

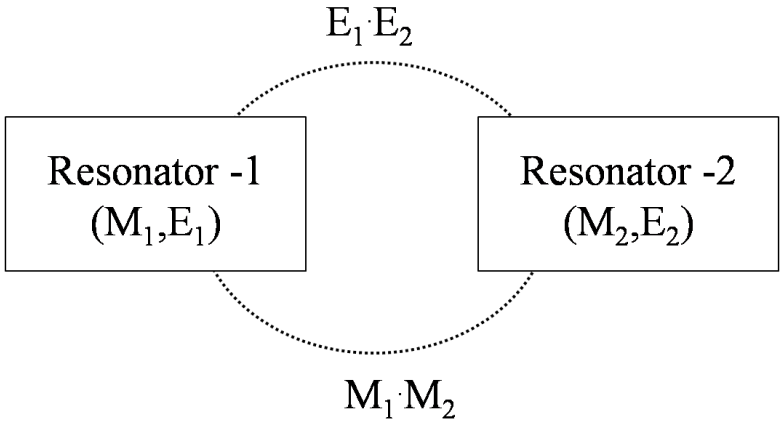

Figure 2.7. Diagram showing the electromagnetic coupling between the resonators.

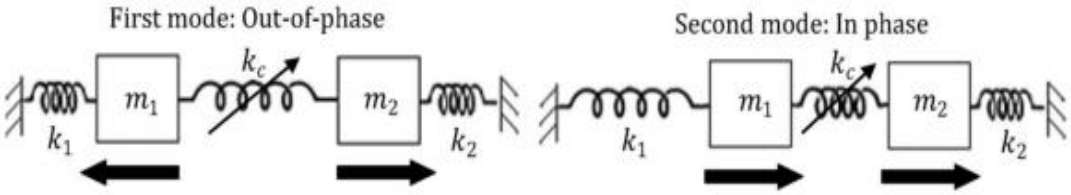

Figure 2.8. Schematic showing the out-of-phase and in-phase motion of the coupled resonator.

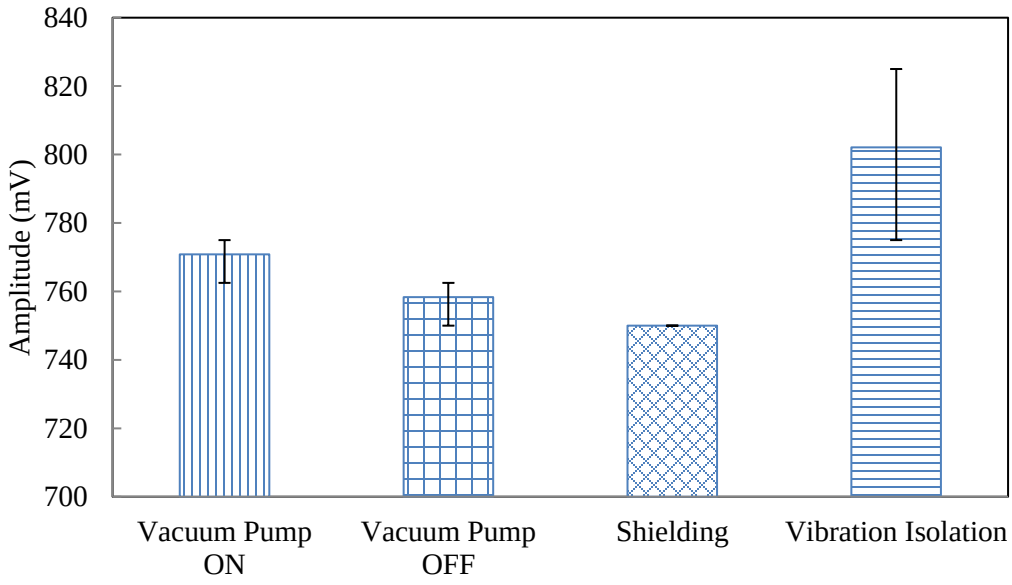

(a)

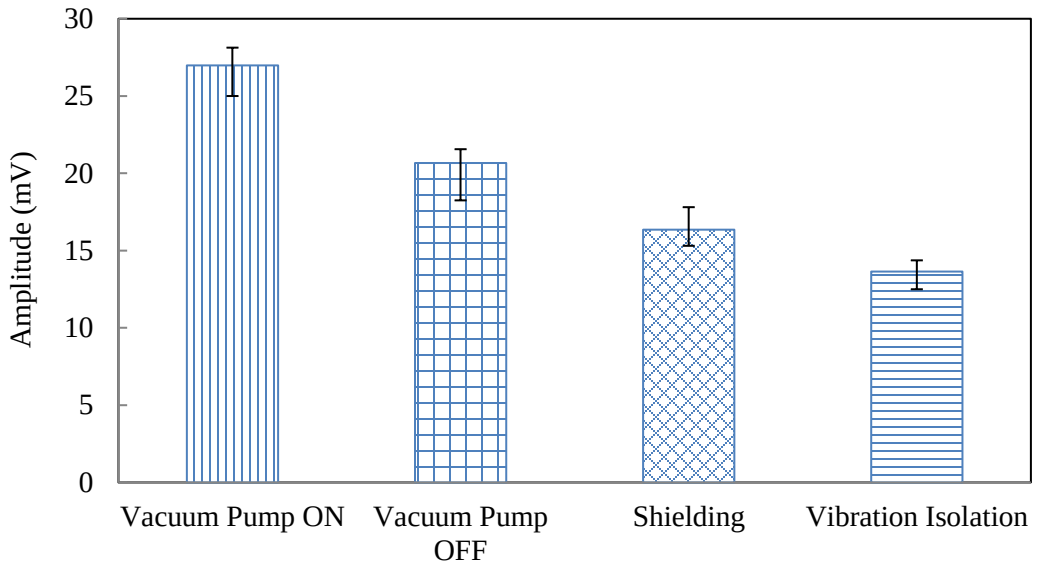

(b)

Figure 2.9: Graphical comparison of (a) the output and, (b) the noise-floor from the magnetoelectric sensor for different working conditions.

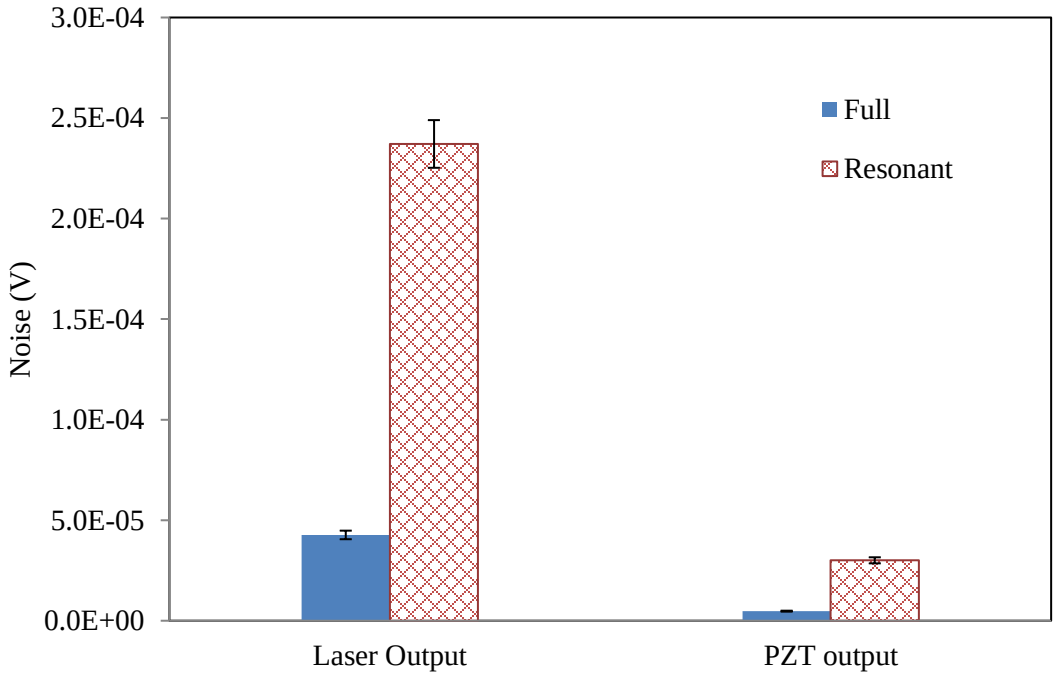

Figure 2.10. Graphical comparison of the electronic noise from the magnetoelectric sensor for optical and piezoelectric transduction at 0.07 nT and 0.8 nT input.

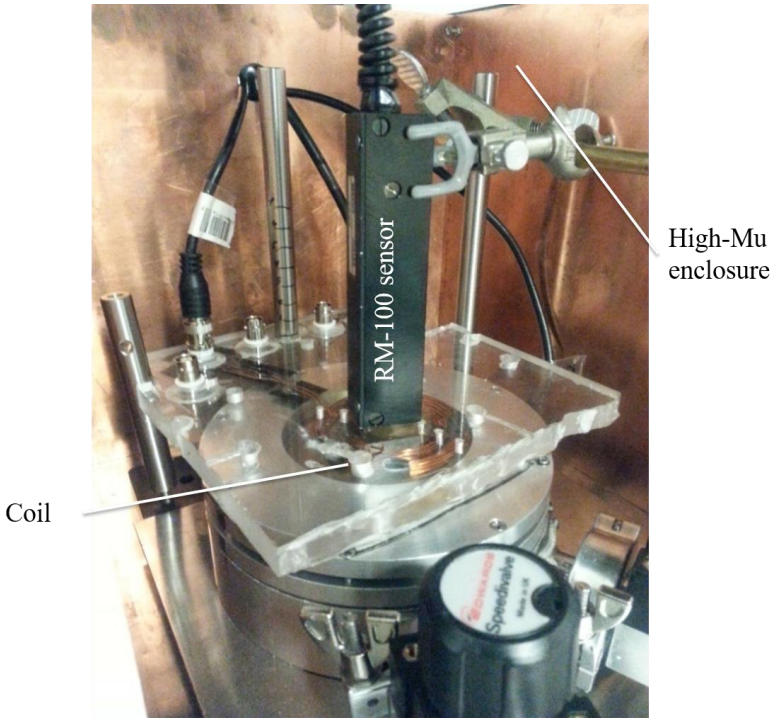

Figure 2.11. Pictorial representation of the setup used for calibrating the coil using RM-100 NanoTesla meter.

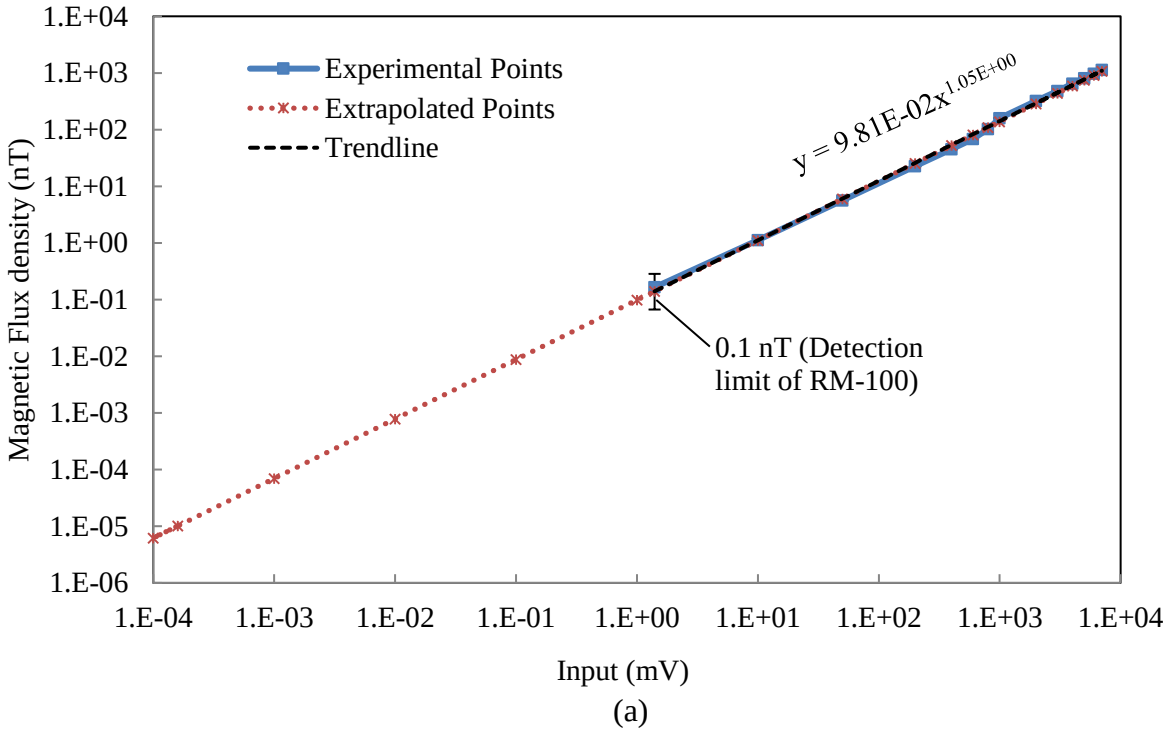

(a)

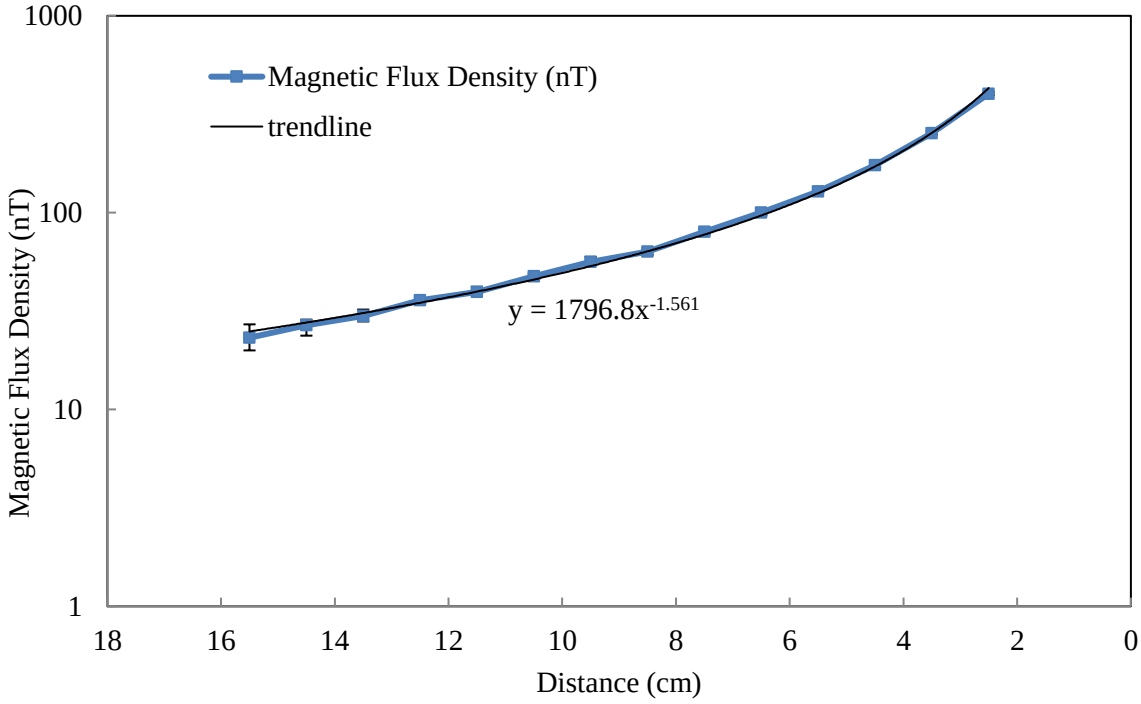

(b)

Figure 2.12. The magnetic field produced by the coil with varying (a) input voltage, and (b) stand-off distance calibrated using RM-100 NanoTesla meter.

CHAPTER 3

27 pT FERROMAGNETIC MEMS SENSOR

In this chapter, we will discuss the ferromagnetic MEMS magnetometer's design in the Section 3.1, the fabrication in the Section 3.2, the simulation in the Section 3.3, the experimental set-up in the Section 3.4 and the results in the Section 3.5 in detail. In the Section 3.5 we will discuss the main results that include the improvement in sensor's MDS by 16.8% (2.28 μT to 1.9 μT) using external bias, and by 19 times (1.9 μT to 100 nT) using a vacuum. We achieved an MDS of 27 pT by using external bias, vacuum, parametric amplification, electronic noise cancellation and shielding simultaneously.

3.1 Sensor Design

We designed four different structures for the ferromagnetic MEMS sensor (see Figure 3.1). The MEMS sensor consisted of a bridge (plus, three leg and simple bridge) and a diaphragm silicon nitride flexure Section (see Figure 3.1). We then attached a neodymium permanent magnet. The magnet's weight ranged from 12-24 mg and was larger than the nitride flexure weight (0.02-0.3 mg). The device #1, a plus shaped bridge (see Figure 3.1a), was found to have a more stable output response, whereas the device #2, a 3-leg bridge gave the maximum output (see Figure 3.1b). The device #3, a fixed-fixed bridge (see Figure 3.1c), though gave smaller resonant frequency, was unstable due to the magnet mass and resulted in the loss of laser reflection at resonance, and hence was

not used. The device #4, a diaphragm structure (see Figure 3.1d) was stable too, but the resonant frequency of the structure was high and as the sensors were tested in a vacuum, it required a separate mount to equalize the pressure. The spring constant of the structure ($k = \frac{AEt^3w}{\ell^3}$) varied with the number of legs from the foot-mass. For plus bridge A=4 ($k = \frac{4Et^3w}{\ell^3}$), whereas, for the 3-leg bridge A=3 ($k = \frac{3Et^3w}{\ell^3}$). The structural dimension of the devices varied from 6-10 mm in length, 1-4 mm in width to 1 μm in thickness.

3.2 Fabrication

The sensors were fabricated on a double sided polished Si wafer (see Figure 3.2) that was cleaned using a piranha solution followed by a buffered oxide etch (BOE). The wafer was thermally oxidized to form 500 nm of SiO_2 by wet oxidation at 1050 ˚C. This layer had a compressive stress of 300 Mpa. This was followed by a low pressure chemical vapor deposition (LPCVD) to deposit 1-2 μm thick silicon rich nitride layer at 825 ˚C. The stress in this layer was 128 Mpa tensile. The oxide and nitride had a combined compressive stress of ~14 MPa. The stress in the thin film was measured using Tencor P-10 surface Profilometer. The wafer was tested at every step of processing for the stress induced in the thin film. The nitride was then patterned and free-standing structures in the form of cross bridges, bridges and diaphragms were obtained using 50 sccm of CF_4 and 5 sccm of O_2 at 15 ˚C. Finally, using an Al metal mask on the back, the wafer was subjected to DRIE using SF_6 and C_4F_8 until the structures were released completely. The devices were diced using Disco DAD-641. Subsequently, a small (1 mm^3) neodymium magnet was attached to their center (see Figure 3.1). The devices of varied dimensions (length – 6 to 10 mm and width -1 to 4 mm) were fabricated and characterized.

3.3 Simulation

The experimental results were compared to the COMSOL simulated results [credit: Ming Gao]. A force of 200 nN was used for simulations to enact the effect of the external bias (see Figure 3.3). The resonant frequency for the simulation was off by 0.45 Hz. The material parameters were adjusted to match the experimental results (see Figure 3.4). The plus bridge (device #1) was characterized as seen in the Section 3.5 by varying the external magnetic bias from +28.75 mT to -28.75 mT, as using experimental results in following section. The same external bias could not be used for the device #2, as the resultant force produced by it could damage the sensor. Hence, the device #2 was characterized only using excitation coil and no external bias was applied to it. Even without an external bias the device performed much better than the device #1. Simulated data allowed us to understand the force needed to levitate the structure. The built-in stress and gravitational force gave a displacement of 6.7 μm (see Figure 3.3). When an external stress of 4.1E+8 (N/m^2) was applied, the displacement reduced by 0.08 μm.

3.4 Experimental Set-up

We tested the sensors in a 1 mTorr vacuum inside an aluminum sample holder with an optical window (see Figures 3.5 and 3.6). The optical detection techniques for non-contact displacement measurement include beam triangulation [68], interferometry [69-71], and Doppler vibrometry [72]. All the techniques use a laser reflected from the sensor for measurement. We focused the laser beam over the region in the sensor that gave the largest possible signal. The network analyzer was used to produce an input magnetic field in the coils and the output from the sensor was detected using the Laser Doppler vibrometer. The diaphragm (device #4) structure had a smaller amplitude of vibration and

as the device was tested in vacuum needed a raised platform for pressure equalization.

The resonant characteristic of the plus bridge (device #1) was more stable than the fixed-fixed bridge as observed using laser Doppler vibrometry. However, the 3-leg bridge structure gave the best response. In order to improve the output from the sensor, signal improvement strategies, as discussed in Chapter 2, were used.

3.5 Results

We applied 0.07-1.1 nT (14-200 μA) excitation using the inner coil (Ø=3 cm) (see Figure 3.5) for measuring the sensor's response. There was no external bias used for the initial case, so the effective spring compliance of the structure (see Figure 2.4a of Chapter 2) was affected only by the built-in stress and magnet mass. In the Section 3.5.1 we will look at the extended spectrum for the noise-floor calculation and in the Section 3.5.2 the results obtained by using the signal improvement strategies will be discussed.

3.5.1 Extended Spectrum

The sensor's output for a 50 Hz to 3 KHz frequency sweep (see Figure 3.7), was used to determine the noise-floor. The amplitude of the sensor was smaller, in this case, as higher bandwidth (30 Hz) was used for measurement. For all other measurements, a bandwidth of 2 Hz was used. The input to the inner coil (see Figure 3.5) was fixed at 0.07 nT (0.707 mV). We calculated the RMS noise level for the frequency range of 638 Hz to 3 KHz. The motive of this spectrum was to show the decrease in noise level as the sweep goes away from the resonant peak. For all the noise reduction techniques used, we tried to reduce the noise level near the resonant spectrum. Stray magnetic field from overhead power lines, nearby instrument, earth's magnetic field, environmental vibrations, and

electromagnetic noise (see Figure 3.7) added to the noise-floor. To improve the sensor's sensitivity, noise-floor was needed to be as low as possible.

3.5.2 Strategies to Improve the Sensor Signal: Results

The results obtained for the spring constant modification of the sensor will be discussed in the Subsection 3.5.2.1. We will then look at the improvement in the electronic noise using shielding and concentrators in the Subsection 3.5.2.2. In the Subsection 3.5.2.3 we will discuss the improvement in sensor's response by the introduction of a vacuum. In the Subsection 3.5.2.4 results obtained for the parametric amplification will be presented. We will conclude the section with a detailed analysis of the noise reduction in the Subsection 3.5.2.5.

3.5.2.1 Spring Constant Modification

External magnets were used to enable in-situ tuning of the Hooke's constant. The external bias results in either an increase or a decrease in the overall Hooke's constant of the device (see Figures 2.4b and 2.4c). The external bias changed the effective spring constant (k_{eff}) of the sensor either increasing or decreasing it. On the other hand, the resonant frequency increased by 14 Hz in the first case, and decreased by 5 Hz in the second case (see Figures 3.8a and 3.8b). The external bias, improved the sensor's output by 11-24 μV ($x \sim F/k_{eff}$). The sensor's output was 139 μV, without any external bias applied, and the resonant frequency was 463 Hz. The external DC bias (B_{bias}), produced by using the permanent magnets, was varied from –28.75 mT to +28.75 mT in the z-direction ($F_{z-sensor} = \frac{\partial(V_m B_s[B_{zcoil} \pm B_{bias}/\mu_0)}{\partial z}$). The external bias either pulled down (see Figure 2.4c) the sensor, increasing its in-plane stress (case 1) or pushed it up, (see Figure

2.4b) thereby floating the magnet and reducing its in-plane stress (case 2). The resonant frequency increased from the center frequency (463 Hz) as the number of magnets increased for +Z polarity of external bias, whereas decreased for –Z polarity (see Table 3.1). The spectrum as shown in the Figure 3.8, is for the plus-bridge structure (device #1). We also tested a 3-leg bridge (device #2), but using lower external bias, as -28.75 mT to +28.75 mT exerted a force enough to damage the sensor.The -Z polarity of external bias decreased the resonant frequency (ω) as $\omega \propto \sqrt{(k_{eff})}$, and increased the amplitude (x) as $x \propto 1/k_{eff}$ (see Figures 3.9 and 3.10). It was, however, not linear with the increasing external bias. The size of the permanent magnet (2 mm^2) mounted on the device was very small in comparison to the biasing external magnets (20 mm^2), which resulted in an angular torque on the sensor causing the inconsistencies observed.

The plus-bridge (device #1) was characterized to provide a relation between the external magnetic flux density and sensor's output and the resonant frequency. The output of the device increased for both polarities of the external bias (see Figure 3.9). However, for the +Z polarity of external bias, the amplitude remained below the amplitude attained without the use of any external bias (139.55 µV). Simulations were performed to match the experimental results in order to determine the parameters affecting the resonance and amplitude of the sensor. The results were almost similar with a stand-off distance of 1.3 cm and using the magnet of dimension 780 µm × 780 µm. For simulation, the Poisson's ratio of the neodymium magnet was set at 0.24 with 7400 kg/m^3 density.

There was an inbuilt compressive stress of -14 Mpa in the thin film [credit: Rugved Likhite]. The external bias levitating the sensor was shown to increase the amplitude by

reducing the built-in-stress of the sensor. The lower '*k*' resulted in improved vibration amplitude (x $\propto 1/k_{eff}$) of the sensor for a given input magnetic flux density. The built-in stress was measured using the Tencor P-10 surface Profilometer (see Figure 3.11). After each step of fabrication, the stress was tested so that the thickness of the next layer could be manipulated to reduce the stress (~0 Mpa). The Tencor P-10 has a vertical range of 50 Å to 130 μm and can determine the surface roughness, waviness, and the step height on curved surfaces. It can measure samples up to 350 mm wide, 57.2 mm thick and 2.2 Kg in weight [74]. The resonant frequency depends on the stress in the thin film. Qu et al. [75] gave a relation between the resonant frequency of the sensor and stress: -

$$f(\in) = f(0) \cdot \sqrt{1 + \gamma_n \cdot \in \cdot (1 - \nu^2) \cdot \left(\frac{\ell}{w}\right) 2} \qquad (3.1)$$

where '$f(0)$' is the resonant frequency without any stress, '$f(\in)$' is the resonant frequency with stress, 'γ_n' is a constant associated with mode shape, '$\in$' is the stress, 'ν' is the Poisson's ratio, 'ℓ' is the length, and '*w'* is the width of the resonating structure. To keep '$f(\in)$' minimum we needed to keep the built-in stress minimum $f(\in) \propto \sqrt{\in}$. At the radius of 45 mm and bow of 9.3 μm, a compressive stress of -14 Mpa was measured.

3.5.2.2 Shielding and Concentrators

80% Nickel-Iron alloy designed especially for magnetic shielding applications was used to improve the noise-floor (see Figure 3.12). Increasing the permeability (μ) of the material surrounding the sensor, decreased the stray magnetic field around the sensor ($B_{shielded} \propto \mu$). The high-Mu sheets shield most of the stray magnetic field (see Figure 3.12a). We used high-Mu sheet in the shaped of a cone, which covered the ferromagnetic

MEMS magnetometer from all sides. An opening at the top allowed the laser to be reflected from the permanent magnet used as a foot-mass in the sensor. This particular design of the high-Mu sheet (0.006") used ($B_{shielded} \propto t$), also worked as a concentrator. The high-Mu sheets allowed the magnetic field to pass only through the hole left at the top left for the laser reflection. The magnetic noise detected by the sensor was observed to decrease by the use of shielding and the concentrator. A comparison of the shielding used for the ferromagnetic MEMS magnetometer and the magnetoelectric magnetometer has been shown in the Figure 3.12. Apart from the device shielding, in case of magnetoelectric magnetometer a copper box (25 cm × 25 cm), layered with high-Mu sheets on all sides, was used. In the case of the magnetoelectric magnetometer, we shielded the hole at the top of the copper box, as the optical detection was no longer used.

3.5.2.3 Vacuum

The ferromagnetic MEMS magnetometer was initially characterized under atmospheric pressure (1 atm). To improve the damping coefficient (b) as seen in Chapter 2, we tested the sensor in a vacuum (1 mTorr). The introduction of a vacuum into the vacuum chamber containing the sensor, reduces the pressure (P) as $P \propto b$ using Equation 2.26. This in turn increases the quality factor (Q) of the sensor by reducing the damping coefficient $\left(Q = \frac{M\omega_0}{b}\right)$. Since the mass of the sensor (12-24 mg) remains the same, the factor that gets affected is the quality factor (Q) as $\left(Q \propto \frac{1}{b}\right)$. The output for the ferromagnetic MEMS sensor improved by a factor of ~2 (see Figure 3.13) in a vacuum as $F \propto 1/b$. The vacuum chamber used, had an optical window for the laser to reflect from the sensor. A normal-bridge (device #3) of dimension 7 mm × 2 mm × 1 μm was used for

testing (see Figure 3.13a). Apart from the device #3, the output from a plus-bridge (device #1) was also determined (see Figure 3.13b). There is a little variation in the resonant frequency as well (see Figure 3.13). Hence, the quality factor is determined by the overall change in the resonant frequency as well as the damping coefficient.

3.5.2.4 Parametric Amplification

To improve the sensitivity of the sensor we used parametric amplification. The term parametric amplification or parametric resonance is an electronic feedback technique that improves both the output ($F \propto B_{eff}$) and the noise-floor, in resonant structures ($B_{eff} = B_{zcoil} + B_{feedback}$). It provides an alternative method that can actuate the resonators, as opposed to the external signal that directly drives the resonator. The spring constant of the resonator varied which in turn modulated the sensor's response. We then subjected the cross bridge (device #1) to a 0.07 nT (0.707 mV) input for parametric amplification, and the response of the sensor with increasing gain was studied (see Figure 3.14b). The amplitude increased almost linearly with increasing gain until it saturated at a gain of 200. For the device #2 the gain was increased while increasing the distance between the coil and the device. For a given stand-off distance (2.5-15 cm), the output was studied only for the maximum gain. Hence, no such relation as shown in the Figure 3.14 was obtained for the device #2. We observed maximum output from the sensor at a gain of 200, above which it saturated (see Figure 3.14). The change increased initially, but saturated at higher gain. The input to the smaller coil (Ø=3 cm) was kept constant at 0.07 nT (0.707 mV). We used an averaging of 3 and a bandwidth of 2 Hz for the measurements. Only the device #2 was used to study the effect of parametric amplification. The resonant frequency of the device was 295 Hz, and the amplitude was

six times that of the device #1, used for initial characterization. The device dimension was 4 mm × 2 mm × 1 μm (see Figure 3.1b) from the center of gravity. With just three legs, the Hooke's constant of the device was smaller and the amplitude obtained was much higher, satisfying the Equation (2.16). For parametric amplification measurement, we used 0.07 nT (0.707 mV) as the input to the primary coil, and a bandwidth of 10 Hz. Since, the output was better in the case of 3-leg bridge (device #2), the input magnetic flux density response was studied for lower values by increasing the distance (2.5-15 cm) between the coil and the device. The gain was then adjusted from 10-5000, as the distance was increased from 2.5 cm to 15 cm until it saturated. Using 0.07 nT (0.707 mV) input with 2.5 cm stand-off distance (magnetic flux density of 0.2 nT), the MDS for plus bridge (device #1) was 12.6 nT without feedback and 7 nT for parametric amplification. For the same input excitation and standoff distance between the coil and the device, the MDS for the 3-leg bridge (device #2) were 2 nT and 1 nT which was improved by further decreasing the input magnetic flux density. The amplification used was significant for both the device #1 and the device #2. For the device #1 apart from the parametric amplification, an AC input was also used as a feedback (see Figure 3.15). For AC input, coil-2 was excited using a signal generator output at 20 Vpp ($V_{secondary} = V_{out}\cos(2\omega_0 t)$) with frequency either kept double ($2\omega_o$) the resonance frequency of the sensor or half the value ($\omega_o/2$) ($V_{secondary} = V_{out}\cos(\omega_0 t/2)$). The amplification achieved in this case was not as high as the parametric amplification.

The device #1 being a more stable structure was excited with higher magnetic flux density. The device #2 was subjected to lower magnetic flux densities (see Figure 3.16) by varying the distance between the coil and the device. Parametric amplification was

useful as a feedback technique and can be used for many applications in order to increase the MDS of sensors. The effect of external biasing on the inbuilt stress was also shown, using it to increase the amplitude of vibration of the sensor. The output from the network analyzer was limited to 0.07 nT (0.707 mV). Increasing the distance reduced the magnetic field, but for a large distance, a larger shielding box was needed. To obtain the sensor MDS, we extrapolated the sensor output down to its noise-floor (signal-to-noise ratio of 1). We then repeated this procedure with different extrapolation methods (power and logarithmic) (see Figure 3.17). The MDS of 27 pT was obtained using linear extrapolation. The MDS range for device #2 was 61 pT-533 pT without feedback and 1 pT-176 pT with parametric amplification. The output, in this case, was for the maximum gain used for each measurement. At 15 cm coil to sensor distance, the minimum input magnetic field detectable was observed. Below 0.02 nT the output of sensor was indistinguishable with noise level. As the input magnetic field decreased, maximum gain at which output saturated increased for the parametric amplification loop. For 0.1 μT the gain used was just 10, however, for 7 nT, 1 nT, and 0.5 nT input the gain used was 100, 500, and 5000 respectively. The extrapolated output for device #2 intersected the noise-floor to give the MDS. The noise-floor, in this case, was measured using the RMS frequency data around the resonant peak, maximizing the effect of parametric amplification. The RMS noise-floor around resonant peak was 77 μV for parametric amplification (PA) and 67 μV without any feedback (NF), as the amplitude was higher for PA. Away from the resonant peak, noise-floor was 18.5 μV for PA and 81.7 μV for NF (see Figure 3.18).

3.5.2.5 Noise Reduction Techniques

As seen in Section 2.3.5 noise affects the minimum detectable signal calculation. The main source of the noise is environmental vibrations, earth's magnetic field, overhead power lines, etc. Complete elimination of the electronics, as well as environmental noise, is a tedious task. However, it can be reduced. We observed that using a high input voltage for measurement increased the noise-floor (see Figures 3.19 and 3.20) by a factor of 1.2 for the device #2. We then calculated the average noise-floor by taking the RMS value of amplitude from 800-1500 Hz. Not only the input, but the bandwidth selected for measurements also affected the noise-floor. A 2 Hz bandwidth gave a much lower noise when compared to a 30 Hz bandwidth. Therefore, for all our measurements we used 2 Hz bandwidth. For electronic noise cancellation, parametric amplification was used. The Figure 3.18 shows the reduction in noise-floor using parametric amplification. At higher input a 37% decrease in noise level was observed, whereas by using lower input value noise level decreased by 17%. It also shows an increase in amplitude (~50%) due to the same. This was the case of active noise control. Passive noise control was done using a vibration isolation system as well as shielding the sensor with high-Mu sheets as discussed in the Section 3.5.2.2.

3.6 Temperature Dependence

In the previous description, all the factors were calculated without considering planar stress and thermal expansion. Planar stress is a special case that occurs very frequently in thin-film materials used in MEMS devices. The linear thermal expansion coefficient of a material, is denoted by 'αT', and it can be defined as the rate of change of uniaxial strain ($\in_x$) with temperature, where 'T' is temperature. For moderate temperature excursions,

$'\alpha T'$ can be treated as constant for the material.

$$\in_x (T) = \in_x (To) + \alpha_T \Delta T \quad (3.2)$$

From Equation (3.2) above, it can be seen that the strain of thin film can change with temperature variation (ΔT). With an increase in temperature, the thin film has more strain, which in turn introduces a resonant frequency shift. This resonant frequency change depends on the Young's modulus, Poisson's ratio, strain, and stress when there is an external temperature variation.

The resonant frequency of the ferromagnetic MEMS structure fabricated varied with temperature. The change was found to be 0.05 Hz/˚C for most part. For this part of experimentation, the sensor was mounted on an iron block with two cavities in the center. A heater was used to heat the iron block, and to actively detect the temperature at run time, we used a *k*-type thermocouple (see Figure 3.21a). One end of the thermocouple was placed in the heating block, whereas the other ended in a temperature controller. For all readings, the set-point was set in the temperature controller (40 ˚C, 60 ˚C, 80 ˚C, and 100 ˚C). The device was mounted on the heater block using a thermal conductive paste. Since, the overall setup had to be enclosed in the vacuum chamber, we used copper tape as the bridge between the inner and outer electrical connections (see Figure 3.21b). The block used to heat the device increased the gap between the coil and the device and hence in this case the coil was placed at the top of the vacuum chamber, 2.5 cm from the device. There was an initial increase in the resonant frequency of the device as opposed to the expected decrease. This was due to the expansion of the silicon frame supporting the device, instead of just the silicon nitride structure. The thermal conductivity (149

$W \cdot m^{-1} \cdot K^{-1}$) of silicon is more than silicon nitride (30 $W \cdot m^{-1} \cdot K^{-1}$), hence, the silicon frame expands first. The temperature change, varies the Young's modulus ($E \propto \frac{1}{T}$) as well as the length of the structure ($\omega \propto \sqrt{k} \propto \frac{1}{l^{\frac{3}{2}}}$). This resulted in an increase of the resonant frequency. The change was 0.05 Hz/°C resulting in a 12 pV/pT/°C variation in temperature coefficient for 28.8 nT (224 mV) input (see Figure 3.22). These values were obtained by finding the sensor sensitivity at each temperature (seven different temperatures as shown in the Figure 3.22 and calculating its average. We repeated the measurements with lowest and highest available excitation voltages to check for nonlinearities or abnormalities at very small (0.8 nT) and very large excitation levels (28.8 nT).

Once the effect of frame expansion was saturated, the effect of bridge expansion became significant. The coefficient of thermal expansion for silicon (2.6e-6 $°C^{-1}$) however, is smaller than silicon nitride (3.3e-6 $°C^{-1}$). Now, as the length of the structure increases the spring constant goes down ($k \propto \frac{1}{l^3} \propto \omega^2$), resulting in a decrease in the resonant frequency. The reverse change was seen again, at around 80 ˚C indicating further expansion of the silicon frame. The effect of temperature on the resonant frequency can be used for remote sensing of temperature in food processing, cancer cells, consumer products, etc. and the output can be picked up using inductively coupled coils.

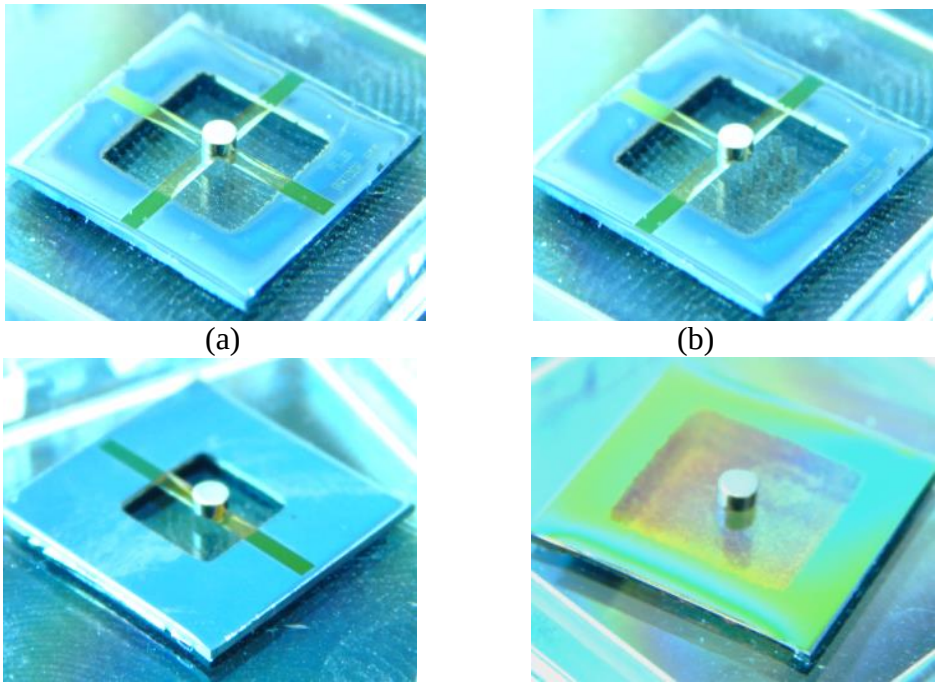

(a) (b)

(c) (d)

Figure 3.1. Optical image of the ferromagnetic MEMS sensor structures, namely: (a) plus-bridge (device #1) (b) 3-leg bridge (device #2) (c) normal bridge (device #3), and (d) diaphragm (device #4).

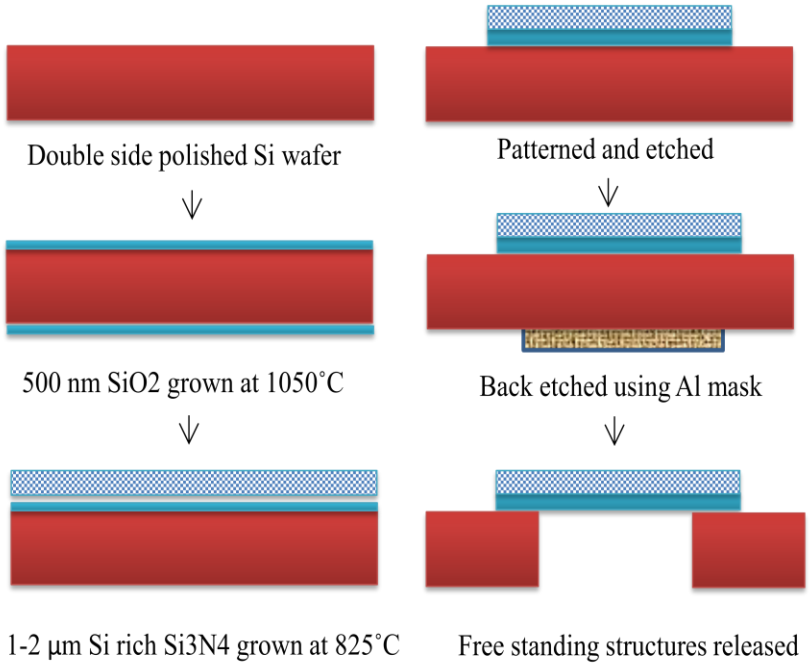

Figure 3.2. Representation of the fabrication steps used for the silicon nitride based ferromagnetic MEMS magnetometer [credit: Rugved Likhite].

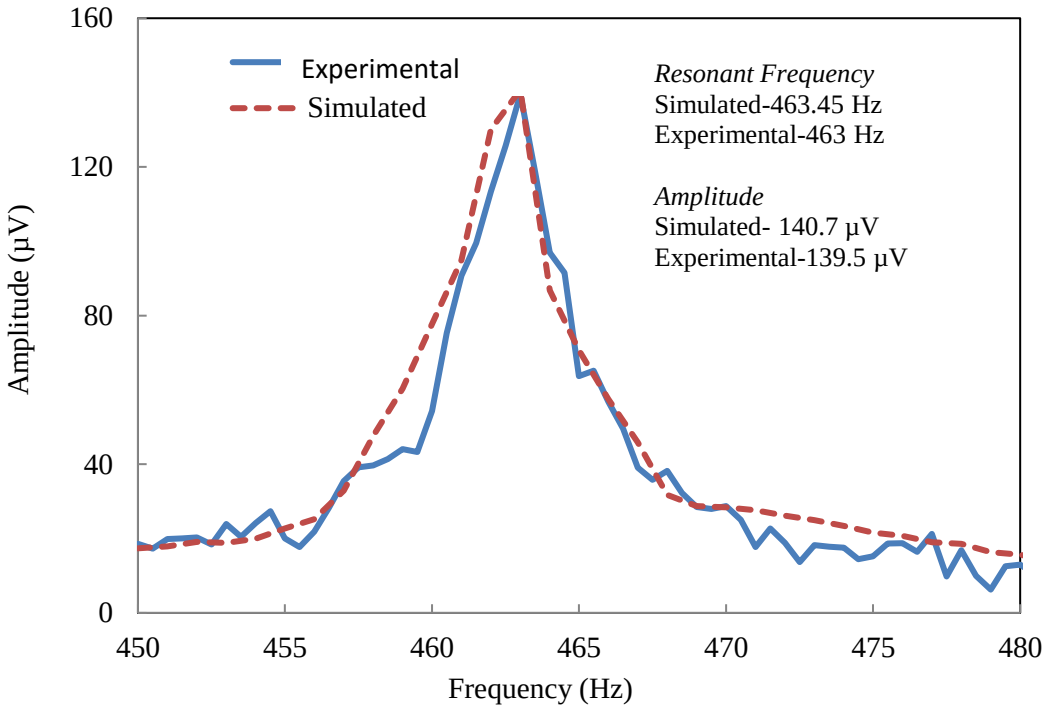

(a)

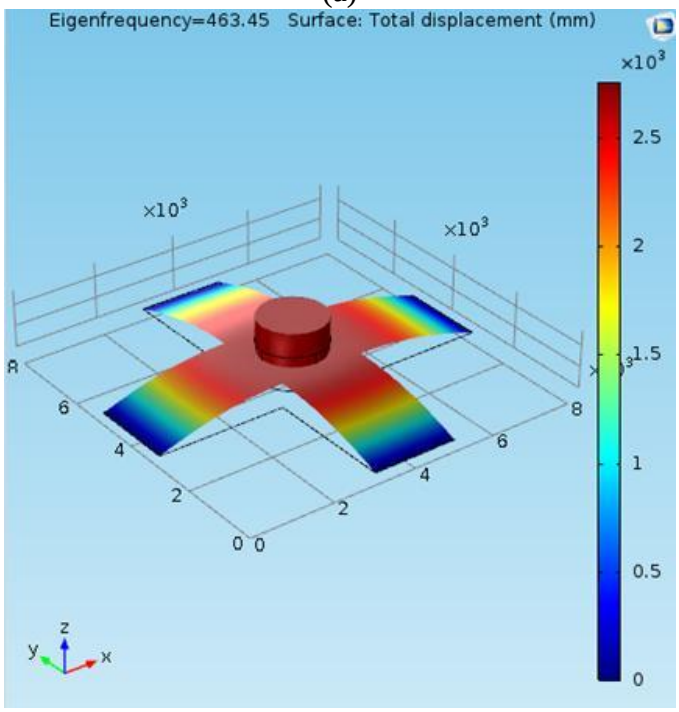

(b)

Figure 3.3. (a) Graphical comparison of the experimental and the simulated output for the device #1 with 0.07 nT input from the coil and, (b) the simulated frequency and the displacement for 200 nN force.

Name	Expression	Value	Description
CrossBridgeL	8[mm]	0.008 m	
CrossBridgeT	1[um]	1E-6 m	
CrossBridgeW	2[mm]	0.002 m	
ExternalMagnetH	4.92[mm]	0.00492 m	Measured
ExternalMagnetR	10[mm]	0.01 m	Measured
Gap	1.3[cm]	0.013 m	Measured
MagnetH	780[um]	7.8E-4 m	
MagnetR	780[um]	7.8E-4 m	

(a)

	Property	Name	Value	Unit
☑	Density	rho	3200[kg/...	kg/m³
☑	Young's modulus	E	297e9[Pa]	Pa
☑	Poisson's ratio	nu	0.27	1
	Electrical conductivity	sigma	0[S/m]	S/m
	Coefficient of thermal expansion	alpha	2.3e-6[1/K]	1/K
	Heat capacity at constant pressure	Cp	700[J/(kg*...	J/(kg·K)
	Relative permittivity	epsilonr	9.7	1
	Thermal conductivity	k	20[W/(m*...	W/(m·K)

(b)

Figure 3.4. Table showing (a) the device parameters and (b) the material properties used for simulation [credit: Ming Gao].

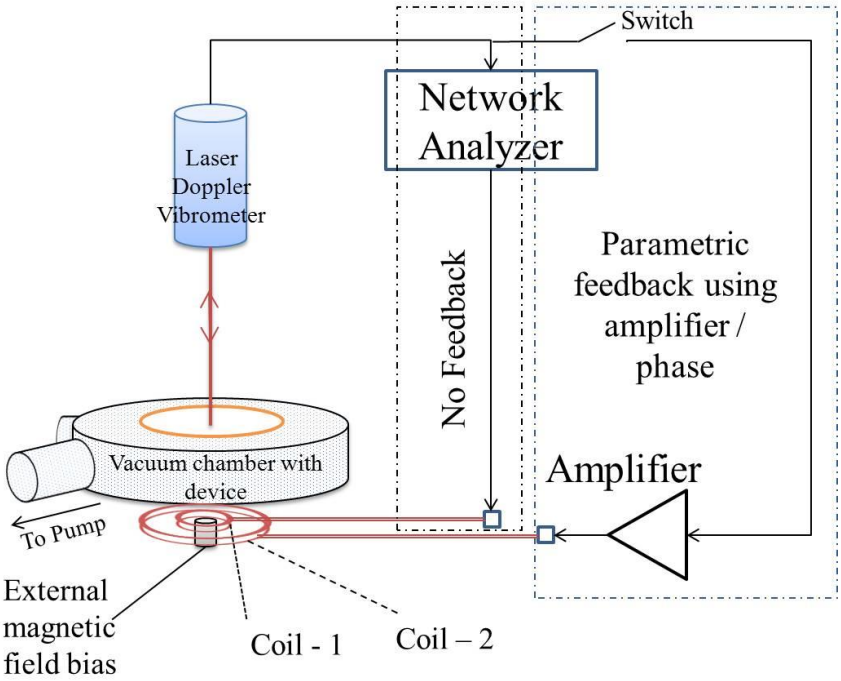

Figure 3.5. Schematic showing the experimental set-up used for the ferromagnetic MEMS magnetometer characterization. [73]

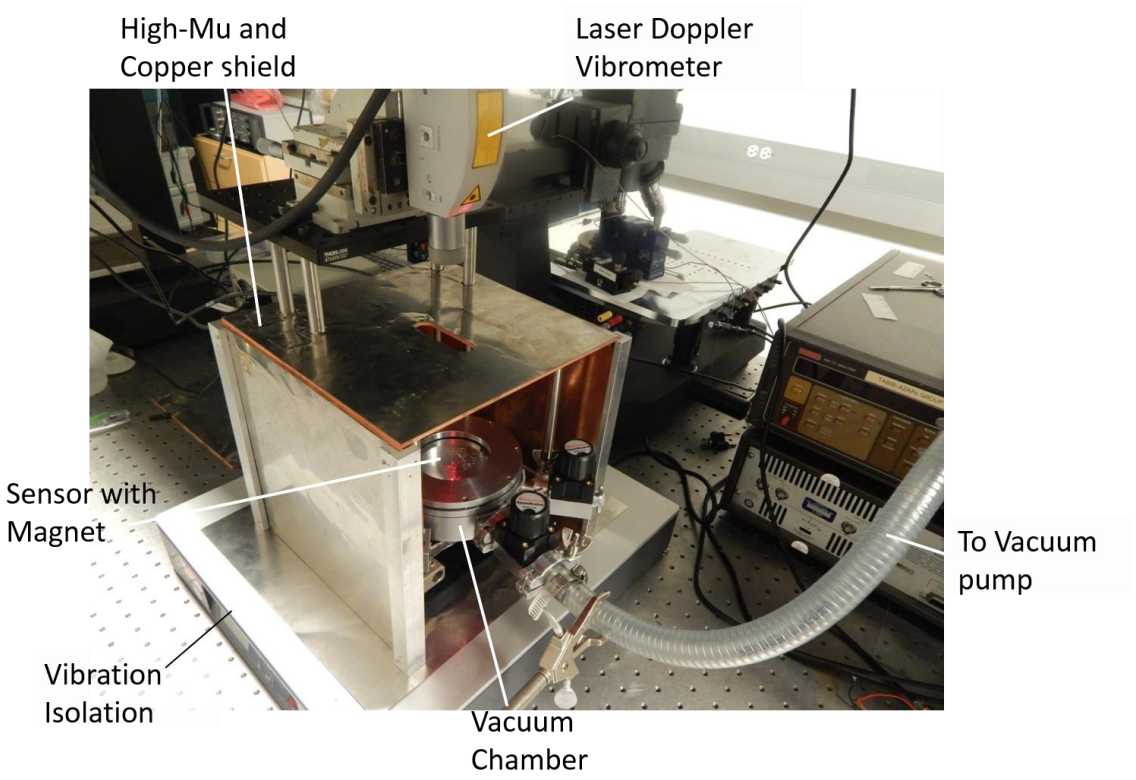

Figure 3.6. Optical image of the experimental setup used for the ferromagnetic MEMS sensor characterization.

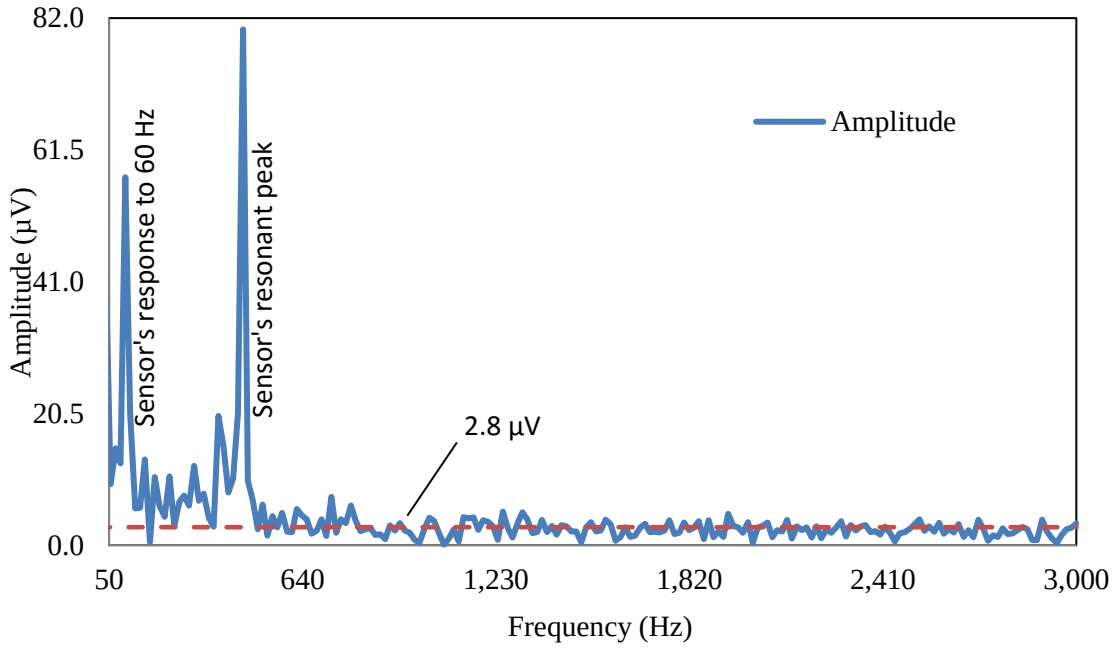

Figure 3.7. A spectrum showing the RMS noise level of 2.8 μV for the device #1. The input to the inner coil (see Figure 2.5) was fixed at 0.07 nT. The bandwidth used was 2 Hz. We calculated the RMS noise level from 638 Hz to 3 KHz.

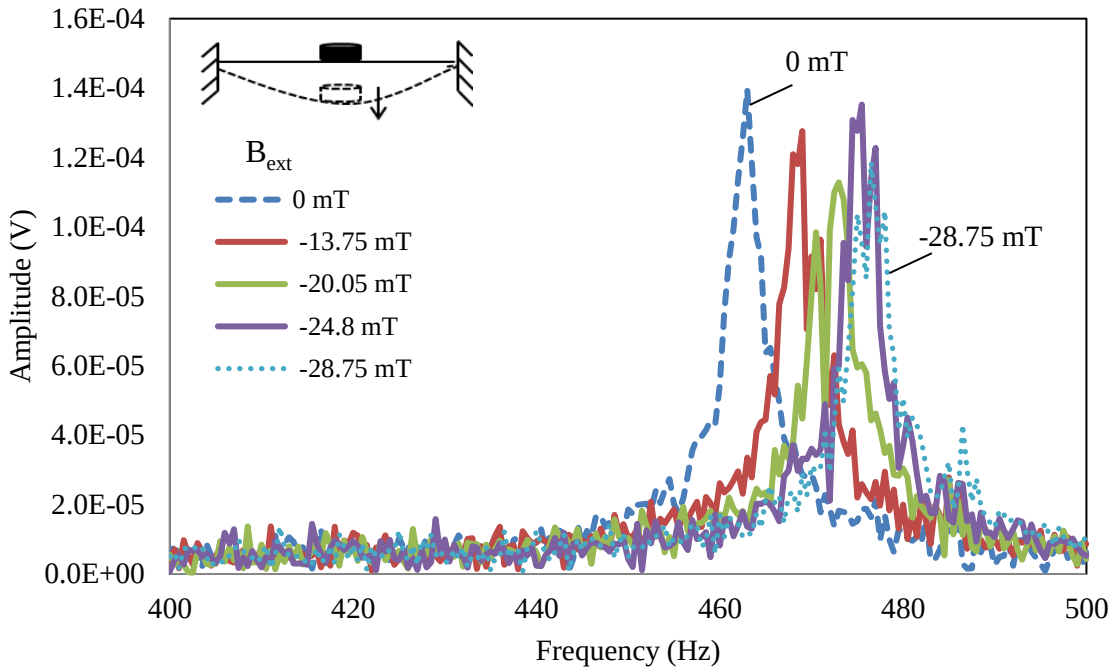

(a)

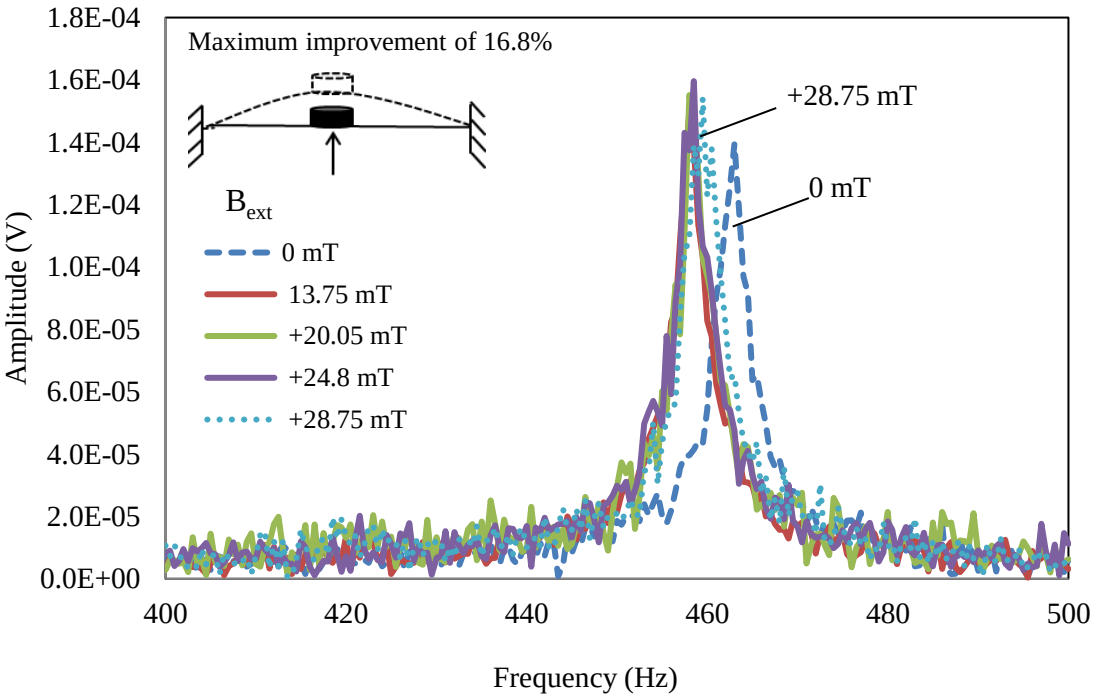

(b)

Figure 3.8. Graphical representation of effect of the external bias with (a) -Z polarity (b) +Z polarity on the amplitude and the frequency for the device #1.

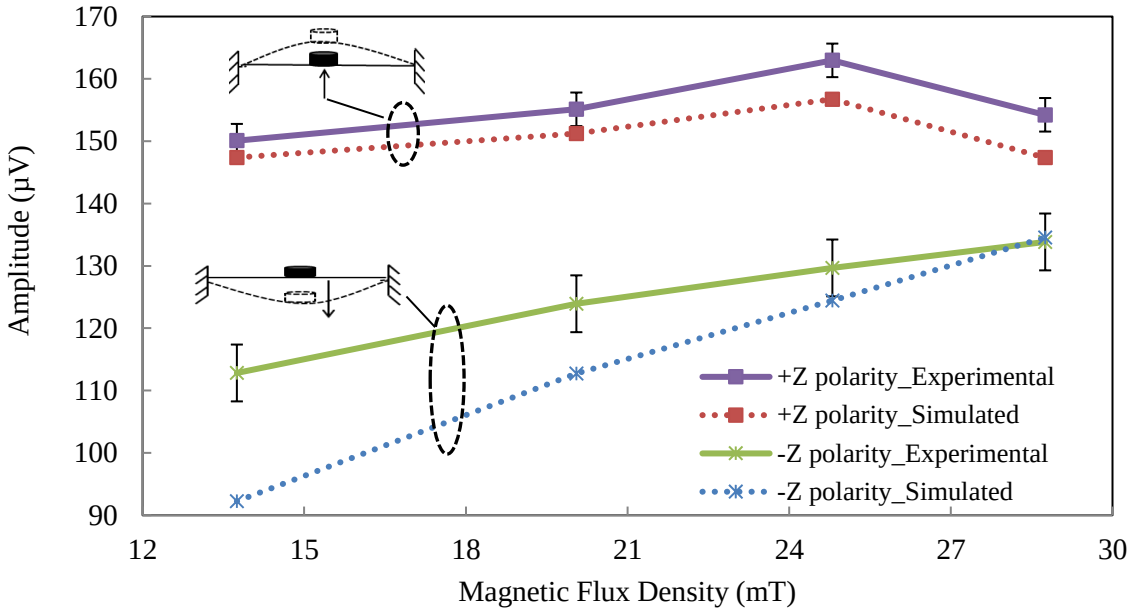

(a)

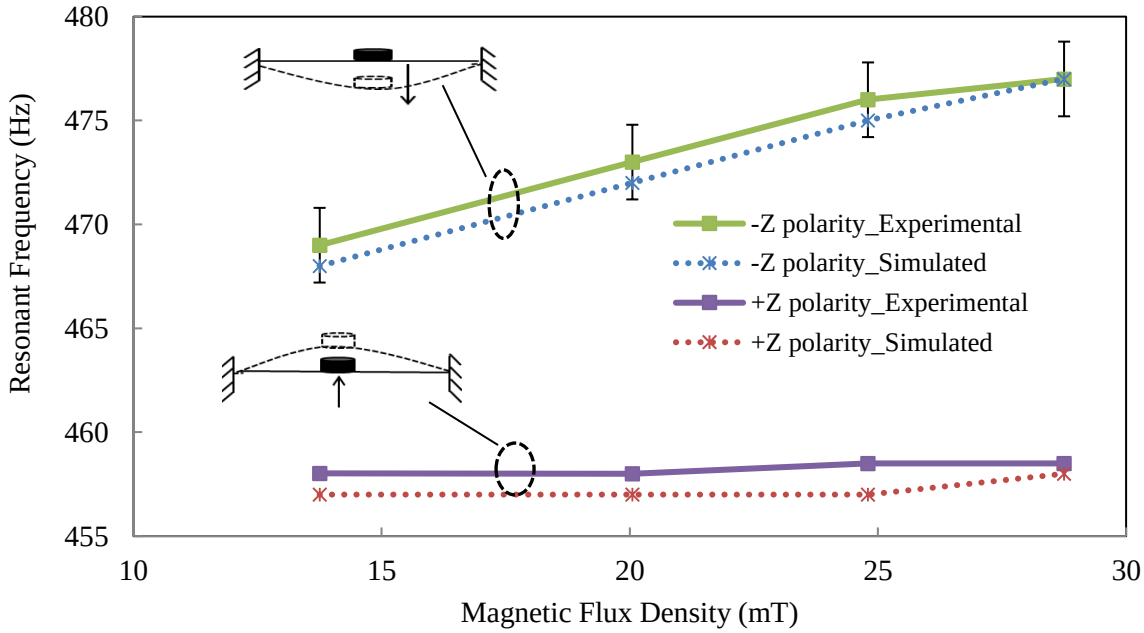

(b)

Figure 3.9. Graphical representation of the variation in (a) the amplitude and (b) the resonant frequency with varying external bias.

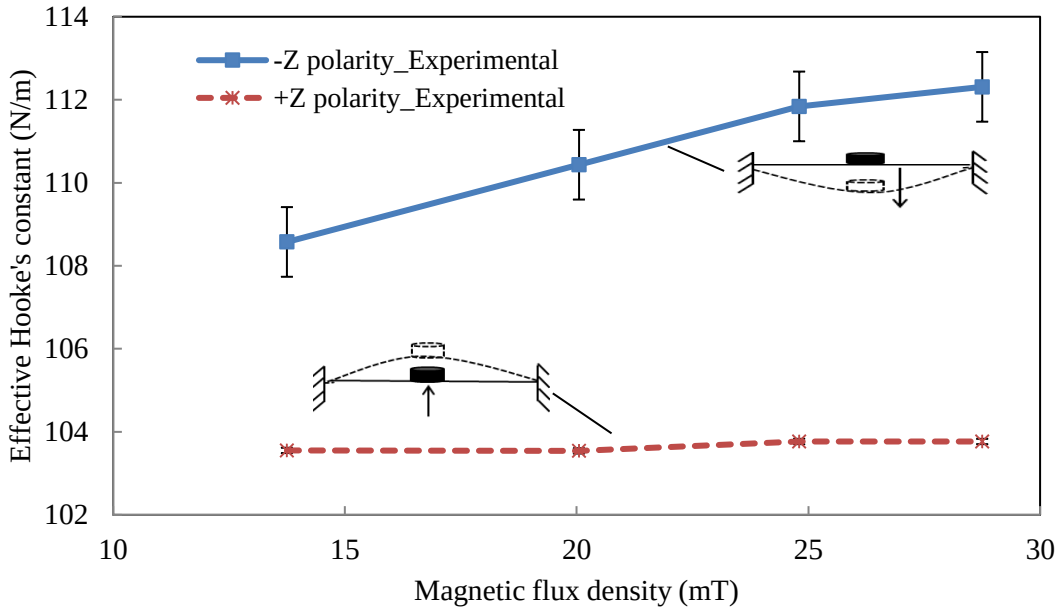

Figure 3.10. Graph showing the effect of external bias polarity and strength on the spring constant of the ferromagnetic MEMS magnetometer.

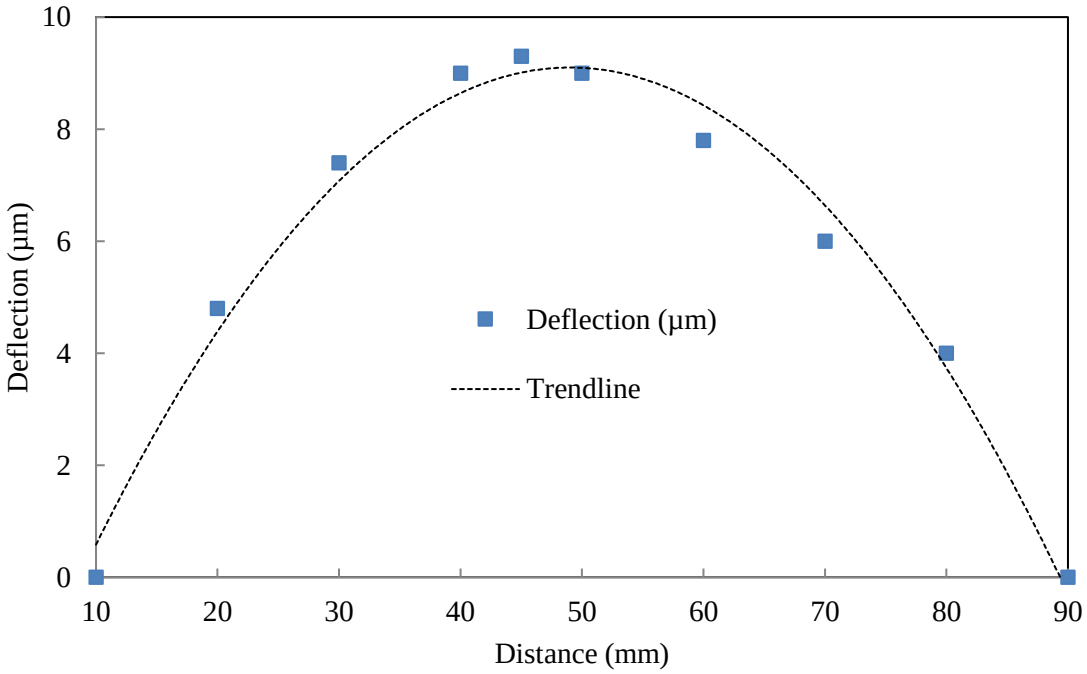

Figure 3.11. Graph showing the deflection in the wafer as a function of distance measured using Tencor P-10 Profilometer [credit: Rugved Likhite].

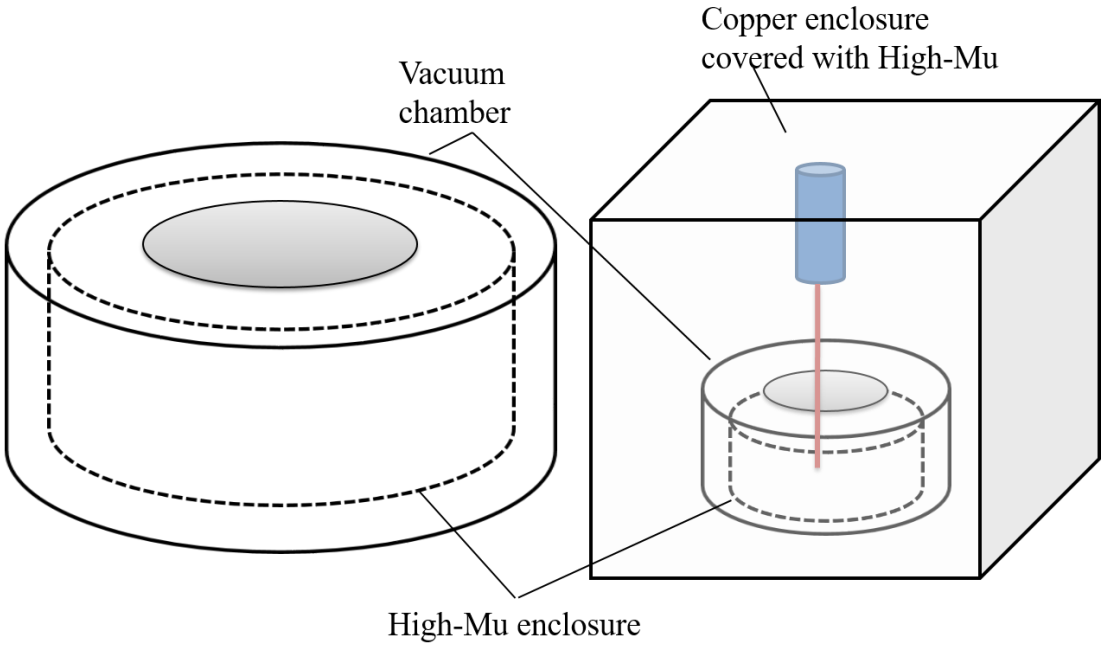

(a) (b)

Figure 3.12. Schematic of High-Mu enclosure used for (a) the ferromagnetic MEMS magnetometer and (b) the magnetoelectric magnetometer.

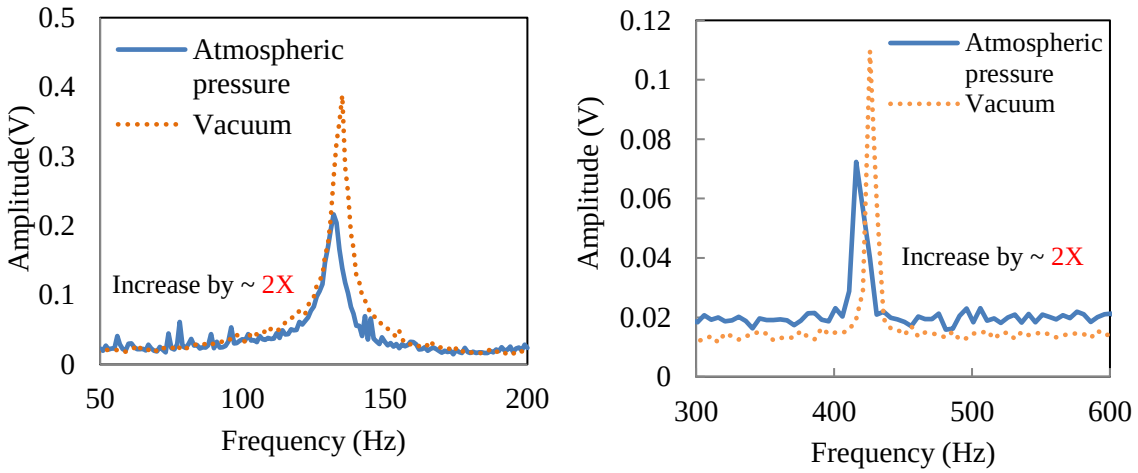

(a) (b)

Figure 3.13. Graphs showing the comparison of output under atmospheric pressure and vacuum (1 mTorr) for (a) 7 mm normal-bridge, and (b) 10 mm cross-bridge.

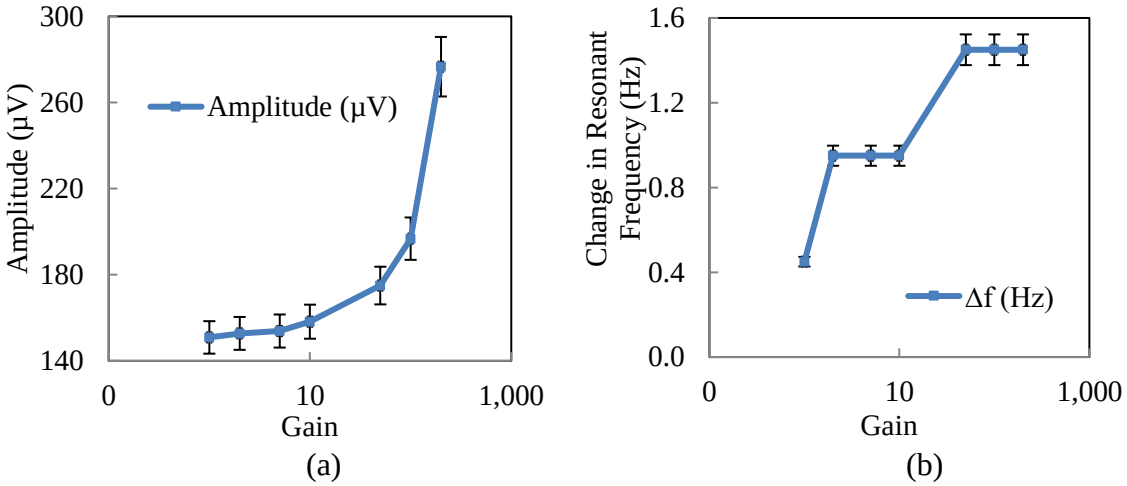

Figure 3.14. Graphs showing variation in (a) the amplitude and (b) the change in resonant frequency for the device #1, with an increase in the input gain of the outer coil (see Figure 3.5) used for parametric amplification.

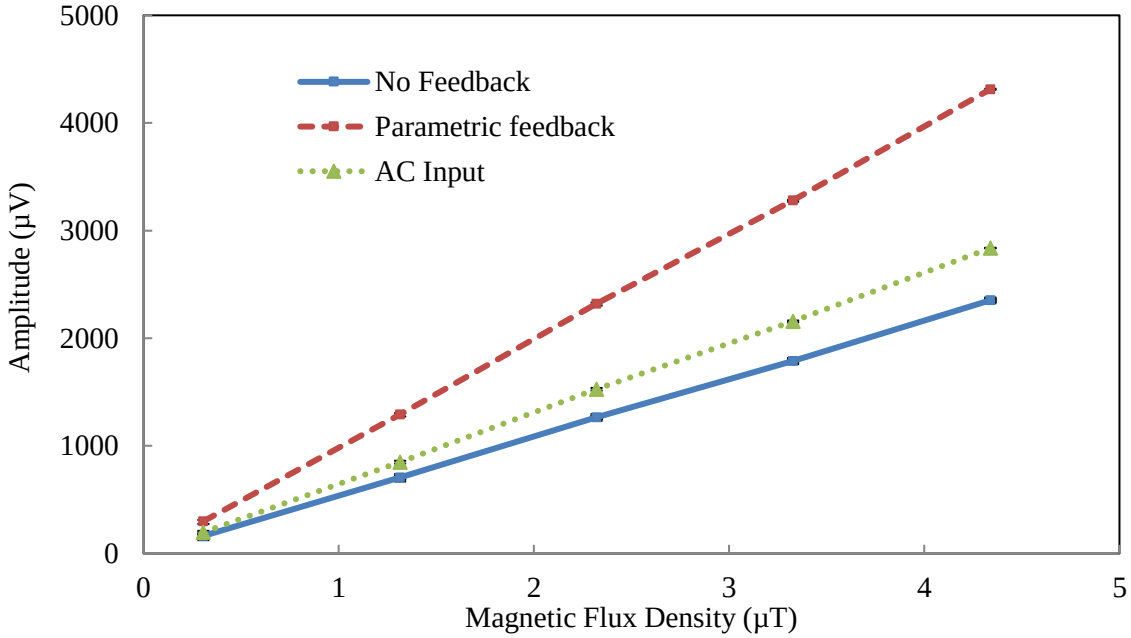

Figure 3.15. Graph comparing the ferromagnetic MEMS sensor's (device #1) output as a function of input magnetic field for no feedback, parametric amplification, and AC input.

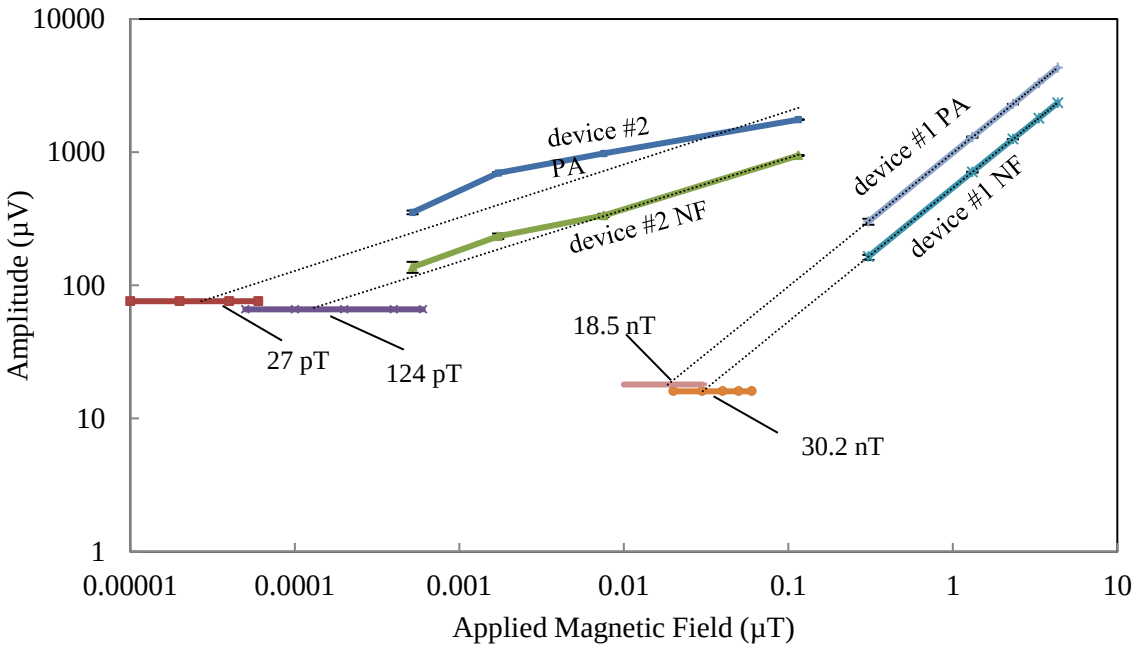

Figure 3.16. Graph comparing the MDS and the noise-floor for the device #1 and the device #2 using parametric amplification (PA) and no feedback (NF).

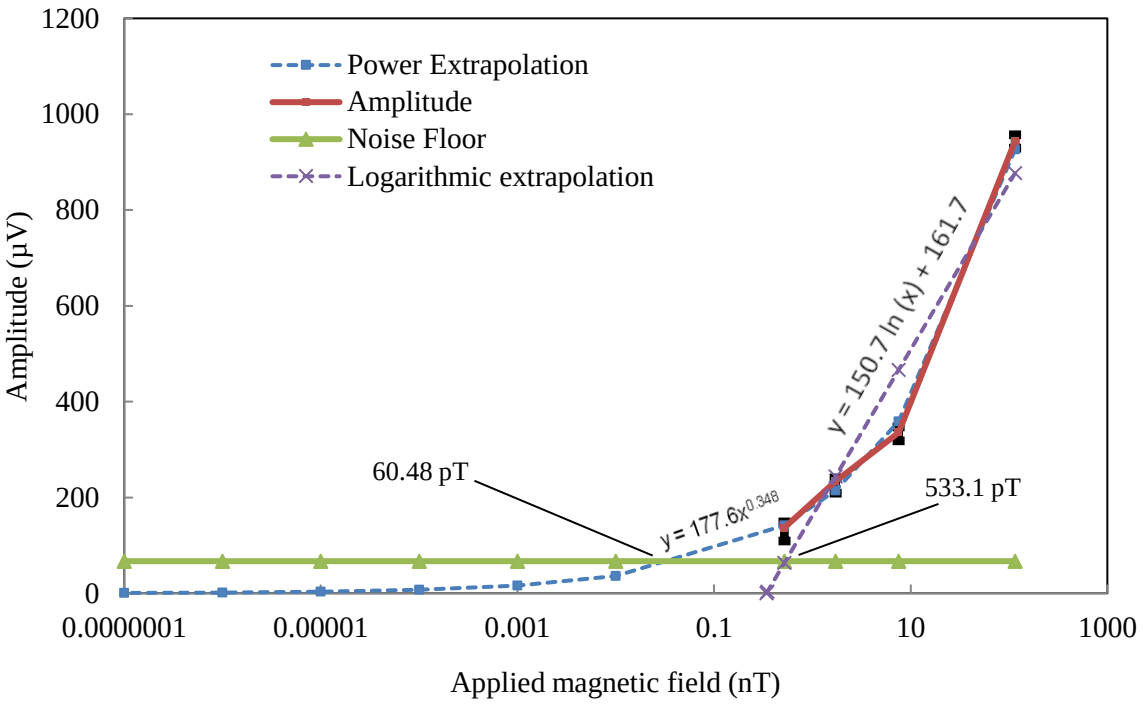

(a)

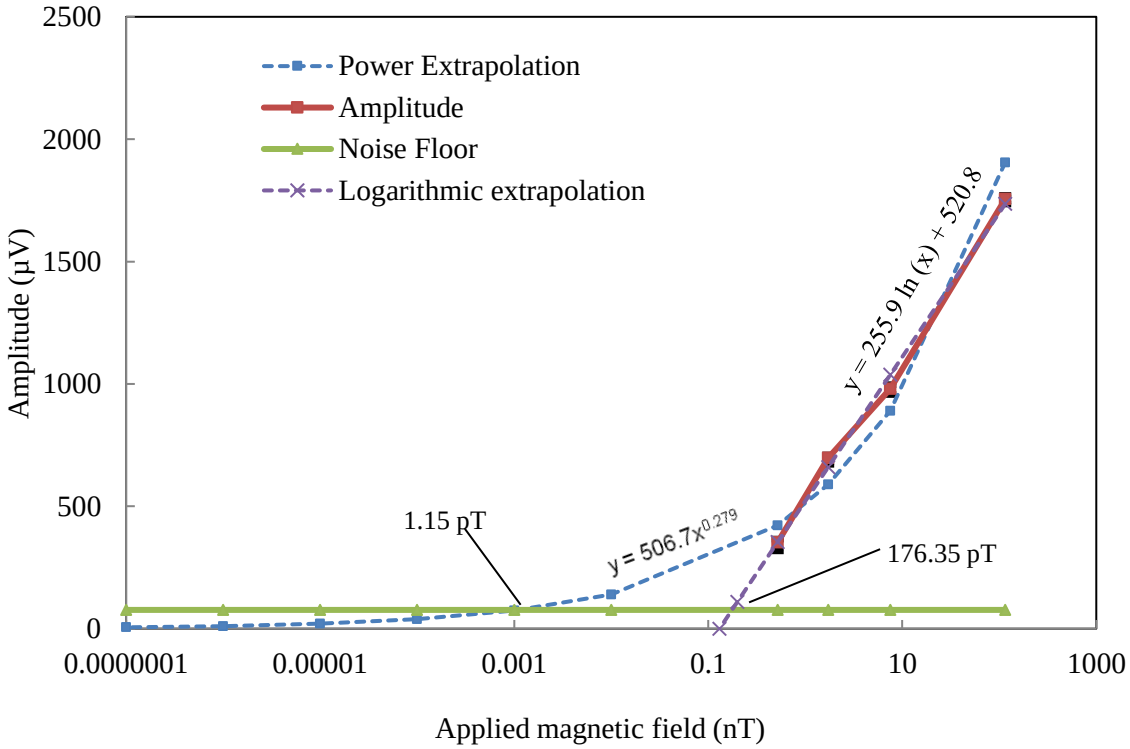

(b)

Figure 3.17. Graph showing the MDS and the noise-floor for the device #2 (a) without feedback, and (b) with parametric amplification.

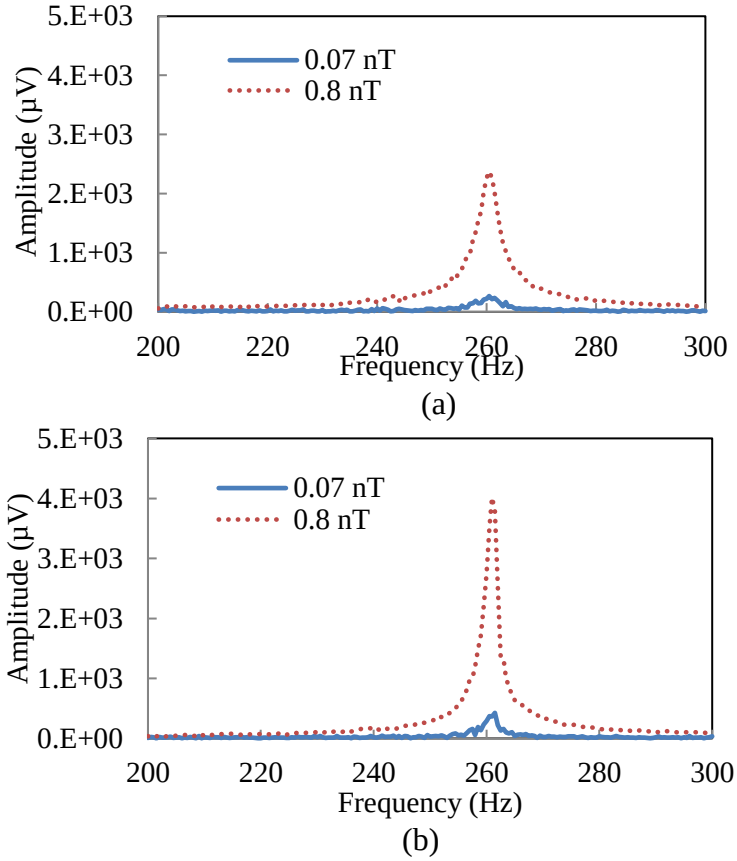

Figure 3.18. Graphical comparison of output from the ferromagnetic MEMS sensor (a) without feedback (b) with feedback for 0.07 and 0.8 nT input for the device #2.

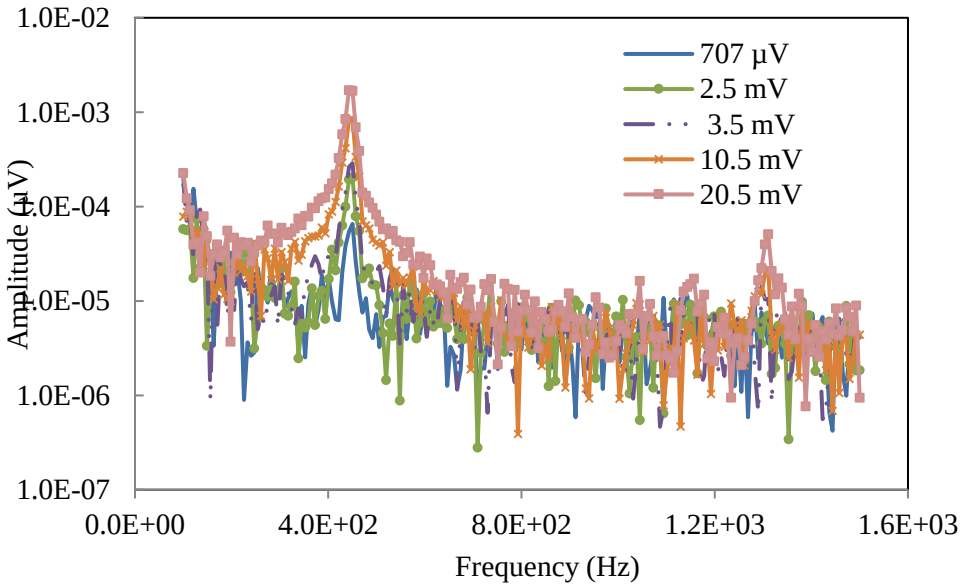

Figure 3.19. A spectrum showing amplitude variation with varying input to the coil. We measured the electronic RMS noise in the frequency range 800 Hz to 1.5 KHz, without using any active vibration control instrument.

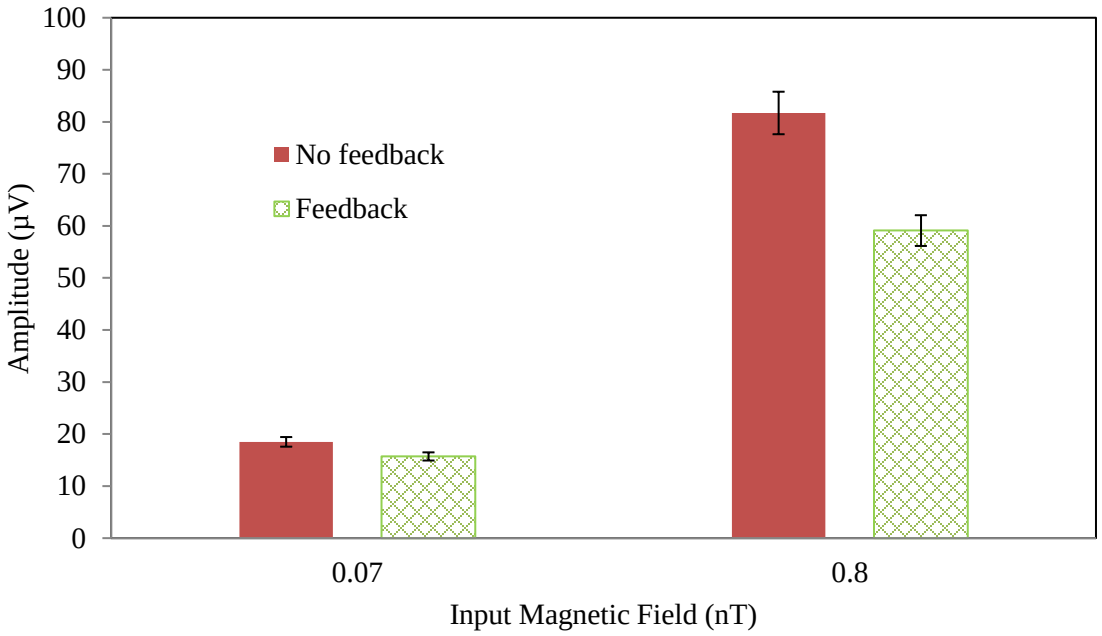

Figure 3.20. Graphical comparison of the RMS noise-floor for the ferromagnetic MEMS sensor (device #2).

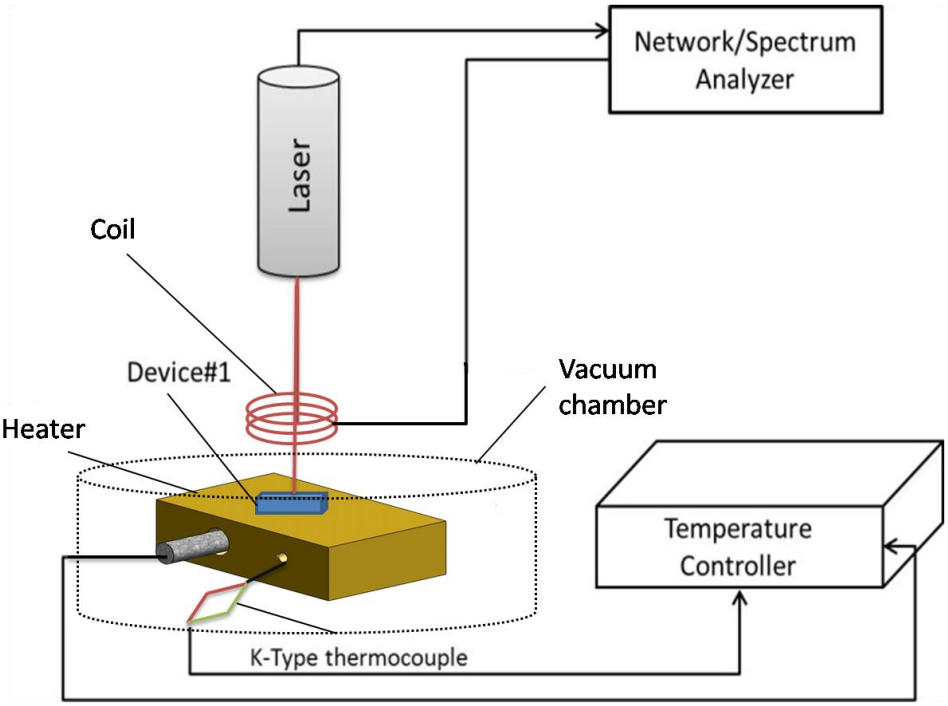

(a)

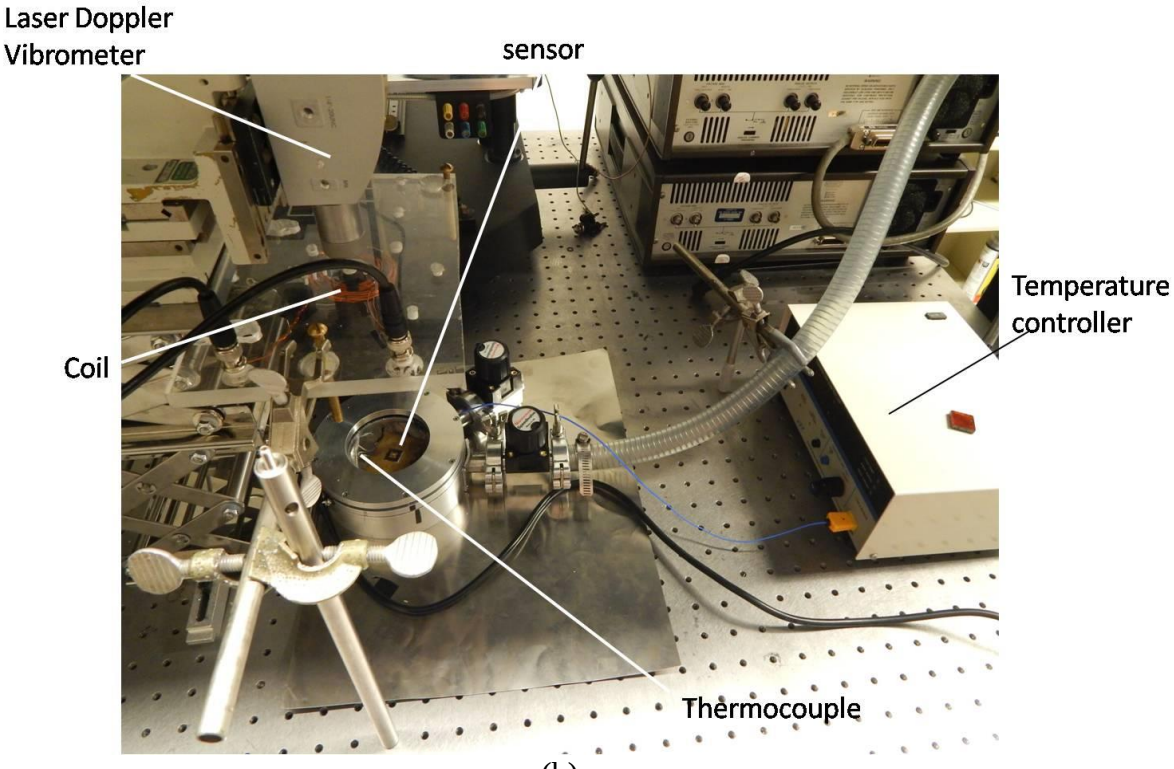

(b)

Figure 3.21. (a) Schematic representation and (b) optical image of the experimental set-up used to study the effect of temperature on the ferromagnetic MEMS magnetometer (device #2).

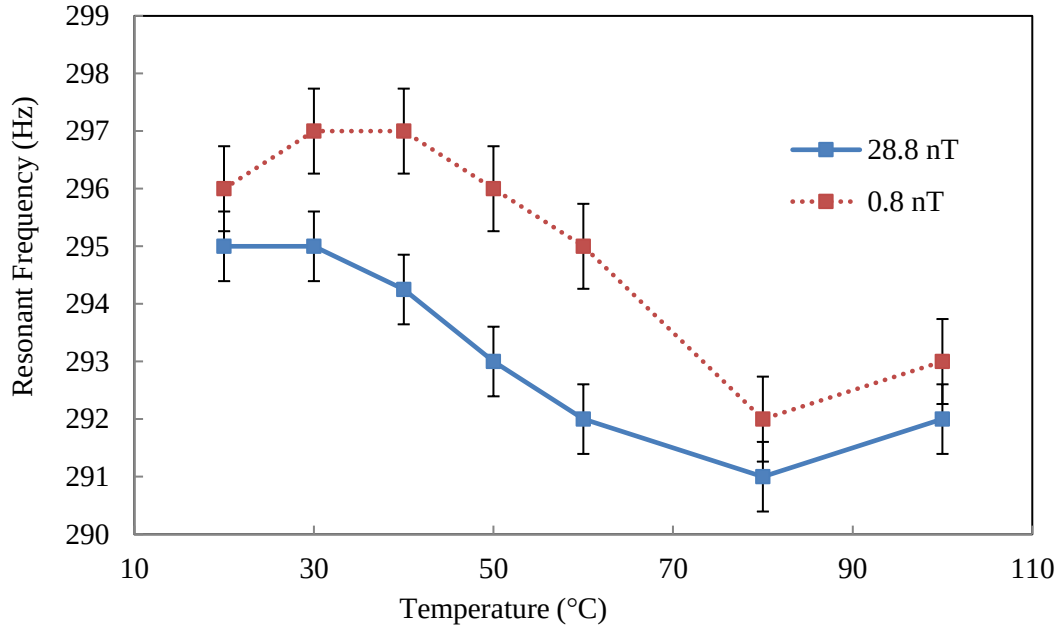

(a)

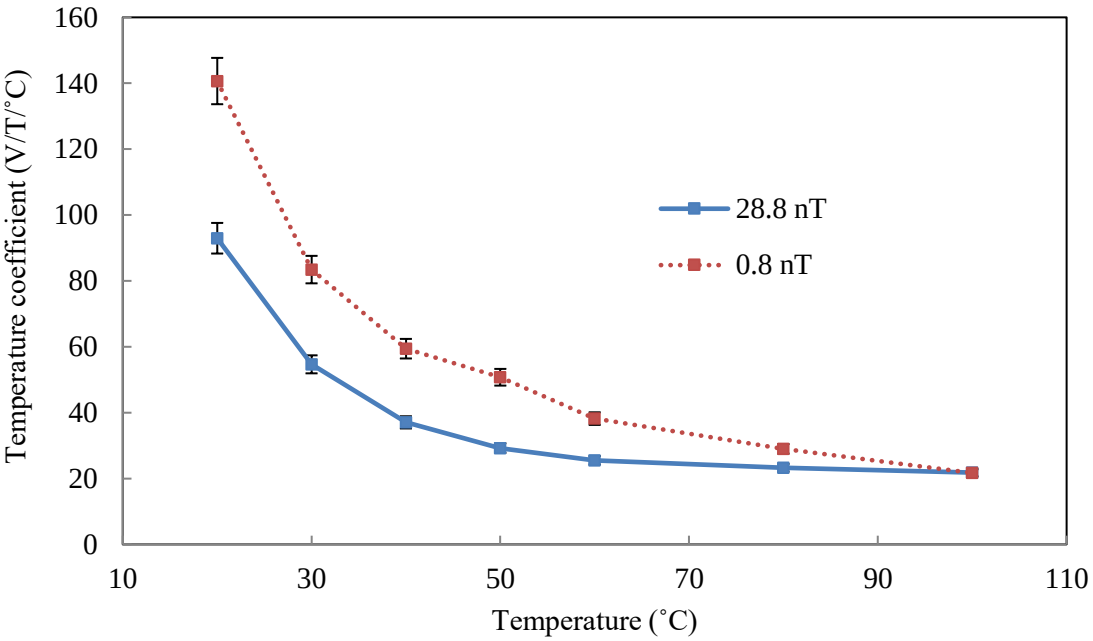

(b)

Figure 3.22. Variation in (a) the resonant frequency and (b) the temperature coefficient of the ferromagnetic MEMS magnetometer (device #2) for 28.8 and 0.8 nT input from the coil.

Table 3.1. The effect of external bias on the resonant frequency and the amplitude of the ferromagnetic MEMS magnetometer (device #1).

External Magnets	Magnetic Flux Density (mT)	Amplitude (μV)		Resonant Frequency (Hz)	
		-Z Polarity Experimental	+Z Polarity Experimental	-Z Polarity Experimental	+Z Polarity Experimental
0	0	139.55	139.55	463	463
1	13.75	112.83	150.08	469	458.03
2	20.05	123.93	155.12	473	458
3	24.8	129.67	162.97	476	458.5
4	28.75	133.84	154.24	477	458.5

CHAPTER 4

40 fT MAGNETOELECTRIC MAGNETOMETER

The magnetoelectric (ME) effect is the process by which a voltage is induced in a material by the application of an external magnetic field and, inversely, the application of a voltage produces a magnetic field. Using this principle, we fabricated mechanically-resonant magnetoelectric devices. The coupling induced between the electrical (PZT) and the magnetic (field from the coil) component is called magneto-electric coupling. The magneto-electric coupling induces a strain in the PZT layer (electrical component) that generates a voltage proportional to the displacement of the foot-mass (magnetic component). Now, in order to push the MDS to the fT level, we needed a large displacement for low magnetic field produced by the external coil, which was excited by an AC signal. A permanent magnet (NdFeB) was used as the foot-mass, as it has a high output magnetic flux to mass ratio, comes in different sizes and shapes, and is readily available.

4.1 Overview

The magnetoelectric effect is the cumulative effect of magnetostrictivity and piezoelectricity. The “Magnetostrictive effect” can be defined by the first part of the Equation (4.1). It is the property of a ferromagnetic material by which a physical change is induced in the material when subjected to an external magnetic field. Cobalt, Terfenol-

D and Galfenol are some materials that exhibit this behavior. Along with the magnetostrictive effect we also used the piezoelectric effect for transduction. The "Piezoelectric effect" is the process that converts mechanical energy to electrical energy. A detailed discussion on piezoelectricity is given later in this section. Both the magnetoelectric (ME) effect and the converse ME effect as shown in Equations (4.1-4.3) are the product of the magnetostrictive effect and the piezoelectric effect.

$$converse\ ME\ effect\ = \frac{magnetic}{mechanical} \times \frac{mechanical}{electric} \tag{4.1}$$

$$ME\ effect\ = \frac{electric}{mechanical} \times \frac{mechanical}{magnetic} \tag{4.2}$$

Thus, eliminating the common terms, the ME effect is the conversion of magnetic energy to electrical energy. The ME coupling coefficient (α) relates the interaction between the magnetic and the electric field. The formula used to calculate the ME coupling coefficient is [76]:

$$\alpha = \frac{\partial E}{\partial B} = \frac{V_{PZT}}{Thickness_{PZT} \times B_{AC}} \tag{4.3}$$

From Equation (4.3) it is evident that the higher the output voltage from PZT beam for a given external magnetic field, the stronger the ME coupling will be. The coupling coefficient represented in terms of the input (*B*) and output (*V*) gives the sensitivity (*S*).

$$S = V/B \tag{4.4}$$

$$ME_{VC} = S/t \tag{4.5}$$

where '*S*' is the sensitivity, '*V*' is the output voltage from PZT, '*B*' is the external

magnetic field strength, 'ME_{VC}' is the magnetoelectric voltage coefficient, and 't' is the thickness of PZT layer.

Apart from understanding the ME coupling effect, we also need to understand how piezoelectricity works. Jacques and Pierre Curie discovered piezoelectricity in the year 1880. The process by which electric charge appears in certain solid materials on the application of mechanical stress is called "piezoelectricity". The materials that exhibit this phenomenon are called piezoelectric materials. The "converse piezoelectric effect" occurs when mechanical stress appears in a material by the application of voltage. This ability to produce mechanical vibration or displacement in response to an electric signal, has influenced the use of piezoelectric materials in applications such as speakers, piezoelectric vacuum pumps, and quartz clocks.

The most commonly used piezoelectric material is PZT. Lead Zirconate Titanate or PZT has the chemical formula $Pb[Zr_xTi_{1-x}]O_3(0<x<1)$ and is a perovskite. PZT is a ferroelectric ceramic that consists of randomly oriented small crystals. Some of the crystals form areas of uniform polarization, called domains. They are built to minimize the intergranular stress, as PZT is cooled during processing. When a layer of PZT is deposited, these domains get randomly oriented within the film, cancelling the effect of each other. Hence, there is no net piezoelectric effect on the application of a very feeble electric field. However, on the application of strong electric field, the dipoles get aligned in the direction of the applied field. The dipole alignment leads to polarization. The voltage from the PZT beam (V_{PZT}) when subjected to an external force (F) is given by:

$$V_{PZT} = \frac{t_p {t_s}^2 (3E_sI_s+3E_pI_p)}{12\, d_{31}E_sI_sE_pI_p}\mathrm{F} \qquad (4.6)$$

where 't_p' is the PZT thickness, 't_s' is the brass thickness, 'E_p' is the PZTs' Young's modulus, 'E_s' is brass' Young's modulus, 'I_p' is the PZT area's moment of inertia and 'I_s' is the brass areas' moment of inertia. Equating Equation (4.6) in Equation (2.6), we can get the value of the voltage generated in the PZT layer ($V_{PZT} = \frac{t_p {t_s}^2 (3E_s I_s + 3E_p I_p)}{12\, d_{31} E_s I_s E_p I_p} \times \frac{\partial (V_m B_s B_{zcoil}/\mu_0)}{\partial z}$) due to an external magnetic field, generated by the coil.

4.2 Sensor Design

Magnetic field sensing using PZT garners broad research interest. Elbahr et al. [77] used COMSOL to simulate macro-scale unimorph piezoelectric cantilever with non-traditional geometry for generation of electrical energy. Brooks *et al*. [78] used thin film PZT and silicon as the substrate. Their device dimensions varied between 200 µm and 1000 µm. The resonant frequencies for the devices were below 350 kHz in most cases. Hong et al. [79] used PZT beams for BioMEMS applications. They fabricated and tested PZT-based resonant cantilevers with resonant frequencies below 50 kHz. Zang et al. [80] fabricated fixed-fixed PZT-based resonant structures with an application for sensing acceleration. The sensors were, however, relatively large structures (300 µm x 1000 µm) with a fundamental mode of 8.2 kHz and a low *Q* of less than 500. Our magnetometer had a low resonant frequency compared to the PZT beam-based sensors mentioned above, as we intend to use it for detection of ultra-low frequency magnetic fields (10-100 Hz). The sensor design, as discussed in Chapter 2, depends on the spring compliance of the beam. Rearranging the Equation (2.11) the spring constant of the PZT beam can be

$$\omega = \nu_n^2 \sqrt{\frac{0.236 D_p w}{(\ell - \ell_m{}^2)^3 (m_e + m_p)}} \qquad (4.7)$$

calculated and yield a well-designed, sensitive resonating structure. We know that $\omega = \sqrt{\frac{k}{M}}$; hence rearranging the Equation (4.7) and using the Equation (2.15) for calculation of 'D_p', we can get the value of '*k*.'

$$k = \nu_n \frac{0.236 D_p w}{(\ell - \ell_m^2)^3} \quad (4.8)$$

where 'ℓ_m' is the length of the proof mass (1.52 mm), '$\ell' = \ell_b$' is length of the beam (9 mm), '*w*' = 'w_b' = 'w_m' is width of the beam (1.5–3 mm), $\nu_n = 1.875$, and 'D_p' is given by Equation 2.15. Now, apart from the parameters mentioned above, since 'D_p' depends on Young's modulus of substrate and PZT and the thickness of substrate and PZT, the spring constant of the sensor will also rely on the parameters mentioned above. Hence, all these factors together contribute to the response of the PZT beam. The magnetoelectric magnetometer's response increased with a foot-mass (until 48 mg). The mass of the neodymium magnet (12-48 mg) contributed a lot to the resonant frequency, and the amplitude obtained. The experimental data for the same, is provided later in the chapter. We now move on to the fabrication of the beams.

4.3 Fabrication

We fabricated the PZT beams of varied widths (1.5–3 mm), keeping the length and thickness constant. We intended to show the coupled-mode response of the magnetoelectric sensor due to magneto-electric coupling as well. Hence, we fabricated the sensors in sets. Two devices of the same dimension were available for testing. The substrate was 0.05 mm thick brass, and the PZT layer was 0.12 mm thick (see Figure 4.1). The resonant frequency of the disc was 7000±600 Hz. It had a resonant impedance

of 100 Ω. In total, five sets of devices were fabricated of varied widths (see Figure 4.2). The disc was cut precisely using a surgical scissor. We needed beams with smaller widths (w) as $k \propto w$, and for better response 'k' needs to be small ($x \propto F/k$). The silver powder used as the top contact, in most cases shorted the beam. A digital multimeter was used to test the same. To remove the silver powder from the brass layer, sandpaper was used to gently scratch the edge. The short was generally eliminated by this method. However, in some cases, in addition to using sandpaper, ethyl alcohol was used to wash the sides. An optical image of the magnetoelectric sensor is given in the Figure 4.3.

To fix the beams to the anchor, we soldered them to a copper covered board. Soldering provided a very rigid support for the PZT beam. The final step was soldering extremely fine conducting wires on the top electrode. The wires were placed as close to the anchor (see Figure 4.3) as possible to avoid undue stress in the beam. Next, we will look at the experimental set-up used for the sensor characterization.

4.4 Experimental Set-up

The experimental set-up for the magnetoelectric sensor testing was similar to that of the ferromagnetic sensor as shown in the Figure 3.5, with a few changes (see Figure 4.4). Since the optical detection method was eliminated, the top slot in the shielding box was closed and shielded (see Figure 4.4b). The output was now produced from the PZT layer and was proportional to the displacement of the foot-mass ($V_{PZT} \propto F \propto x$). To detect the output, the vacuum chamber was tapped for BNC connections. The connections from the sensor were done as shown in the Figure 4.3 and given to the network analyzer as shown in Figure 4.4. For coupled-mode testing of the sensors, an extra Preamplifier was needed to amplify the output that, in turn, was fed to a secondary coil for parametric

amplification. The dimension of the coils was kept the same (Ø=3 and 5.5 cm).

4.5 Results

The AC magnetic field B_{AC} generated by the inner coil (Ø=3 cm) was applied directly perpendicular to the beam length. The axial force produced a strain in the PZT layer resulting in a voltage 'V_{PZT}' across the thickness of the PZT. The magnetoelectric voltage generated across the PZT unimorph has been shown to be non-uniform by Sreenivasulu et al. [81]. The ME voltage '*V*' was measured as close to the clamped end as possible. The value of the voltage from a resonating PZT beam was shown to be at the maximum, near the fixed end of the beam, by Sreenivasulu et al. The magnetoelectric sensor measured the linear relation between voltage (*V*) and the magnetic field (*H*). AC magnetic fields from the coil induced an electrical voltage in the PZT through magnetoelectric coupling effect.

We initially tested the effect of change in the foot-mass, the surface field of the foot-mass, spring constant modification and coupled-mode on sensor output. Increasing the surface field (B_s) of the permanent magnet (NdFeB) increased the output of the sensor as seen in the Figure 4.5. We used Neodymium (NdFeB) magnets (Grade N52) as the foot-mass. Increasing the number of magnets (n) increased the mass as well the surface field ($B_{eff} = \frac{q\mu_0 M'}{V_m}$), where '$B_{eff}$' is the effective surface magnetic field and 'q' is a constant that depends on the surface magnetic field change (ΔB_{eff}) with change in the magnet number (n). We observed that by increasing the count of the magnets, the surface field did not increase linearly. The surface magnetic field was measured using a handheld DC magnetic field sensor. The distance between the top magnet and the sensor was kept constant (see Figure 4.5a). With an increase in the number of magnets (1-4) the field

increased from 1-2.7 mT. The effective force acting on the sensor increased, thereby increasing the output (see Figure 4.5a).

$$F_{eff} = \frac{\partial(V_m B_{eff} B_{zcoil}/\mu_0)}{\partial z} \tag{4.9}$$

From the Equation 4.9 it is evident that as $F_{eff} \propto B_{eff} \propto q$ and $q \propto n$, the force acting on the sensor increases. An increase in the force increases the displacement of the foot-mass ($F_{eff} \propto x$). The change in the mass affected the resonant frequency of the beam ($\omega \propto \sqrt{\frac{1}{M}}$). The mass of a single magnet was 12 mg, with a thickness of 0.029" (0.75 mm) and a diameter of 0.06" (1.52 mm). The input to the sensor was maintained at -10 dB from the network analyzer. The device used for reporting the MDS and the sensitivity in our case, used 24 mg (1.7 mT) foot-mass. Hence, before saturation (<2.7 mT), there is a possibility of improvement in the signal output by a factor of 2.47.

We then used magnetic coupling between two sensors to improve the output of the magnetoelectric sensor. A schematic of the coupled-mode is shown in Figure 4.6. Magnetic coupling coefficient (C_c) as seen in Chapter 2, depends on the magnetic field strength (H_1&H_2) per unit volume ($C_c = \frac{\iiint \mu H_1 H_2 dv}{\sqrt{\iiint \mu |H_1|^2 dv \times \iiint \mu |H_2|^2 dv}}$). Individual sensor response, without coupling was determined as shown in the Figure 4.7. The resonant frequency was ~128 Hz with an amplitude of 1.7 mV. To determine the coupled-mode response, two sensors with similar dimensions and resonant frequencies were selected. When the resonator was excited using an external AC magnetic field, the force on either resonators was in the opposite direction, due to the opposite polarity of the foot-mass ($F_{eff} = \frac{\partial(V_m B_m B_{zcoil}/\mu_0)}{\partial z}$). The spectrum gets split, for coupled-mode response, as in one

case the two beams move up and down (~120 Hz) at the same time (↑↑ or ↓↓), whereas in the other case one goes up and the other moves (~285 Hz) down (↑↓). The magnetic excitation amplifies the opposite motion of the beams. For a given distance (2 mm), the voltage from either beam is $V_{PZT} = \frac{t_p {t_s}^2 (3E_s I_s + 3E_p I_p)}{12\, d_{31} E_s I_s E_p I_p} \times \frac{\partial (V_m B_s B_{zcoil}/\mu_0)}{\partial z}$. However, due to the opposite polarity of the permanent magnet $B_{s1} = -B_{s2}$, leading to $V_{PZT1} = -V_{PZT2}$. The output from individual resonators is fed to a Preamplifier, and thus the final voltage ($V_{PZT} = V_{PZT1} + V_{PZT2}$) gets amplified (see Figure 4.8). As the distance between the two resonators was increased (2-4 mm), the net magnetic field force ($F_{mm}{}'$) between the two permanent magnets reduced $F_{mm}{}' < \frac{\partial (V_m B_s B_{zcoil}/\mu_0)}{\partial z}$. This reduction in magnet-magnet force reduces the coupling coefficient ($F'_{mm} \propto C_c$). Using PZT excitation, we actuated the resonators mechanically. Using the invert function allowed either addition or subtraction of this signal. The mechanical excitation enhanced the motion of the resonators in sync (↑↑ or ↓↓), whereas it suppressed the motion in the opposite direction (↑↓). Hence, it was shown that using coupled resonators the mechanical vibrations can be suppressed. The resonant frequency reduced with the increasing distance as $\omega \propto \sqrt{\frac{k_{eff}}{M_{eff}}}$, and the effective spring constant of the sensor varied ($K_1 \pm K_2$). The MDS obtained using the coupled mode was 5.4 pT, whereas the individual sensors MDS were 13 pT and 16 pT respectively (see Figure 4.9). The noise-floor was also reduced by the use of the coupled-mode. The coupled-mode noise-floor was 3.08 µV, whereas for individual sensor response it was 3.8 µV and 4.05 µV. Thus, using magnetic coupling it was shown that the sensor response can be effectively improved, along with reduction, in mechanical noise. Using coupled-mode, an amplification factor of 2.37 was obtained.

We next investigated the spring constant modulation of the magnetoelectric resonators. In this case, one of the resonator (coupled-mode resonator) was used as the driver/actuator and the other was used as the sensing beam (see Figures 4.10 and 4.11). We know that, $k \propto \frac{D_p w}{(\ell - \ell_m^2)^3}$ and as the width and length of the resonators remained unaffected, the spring constant variation was brought by the change in the external force ($F \propto k$). The actuating voltage beam was excited using a signal generator, with varying voltages at a frequency away from the resonant frequency of either resonators ($V_{PZT} \propto V_0 \cos \omega_{ext} t$), where '$V_0$' is the actuation voltage and 'ω_{ext}' is the actuation frequency. There was a variation in the amplitude (x) with changing external force from the foot-mass on the ($F_{mm} = \frac{\partial (V_m [B_{s1} \pm B_{s2}] B_{zcoil}/\mu_0)}{\partial z}$), where '$B_{s1}$ & B_{s2}' are surface magnetic fields of individual resonators' foot-mass. As $F \sim kx$, for a constant actuation using external bias an increase in 'x' was brought by a decrease in 'k'. Given that $\omega \propto \sqrt{k}$, a decrease in 'k' decreased the resonant frequency (ω).

The final step was the investigation of the effect of parametric amplification on the magnetoelectric magnetometer. For the magnetoelectric sensor, a total of five sets of sensors were fabricated. Out of the ten devices, the best device output was noted and is reported here. We used the best set of sensors for the parametric amplification study (see Figure 4.12). The magnetoelectric sensor was characterized using the same signal improvement strategies as discussed for the ferromagnetic MEMS magnetometer. We then placed the sensor in the vacuum chamber and set the coil over it. The input from the network analyzer was provided to the inner coil (Ø=3 cm), and the output was taken from the PZT and given to the network analyzer. This formed the no feedback case. The output from the PZT was then by-passed through a Preamplifier and given to the outer coil

(Ø=5.5 cm) placed directly above the sensor. The BP was selected such that the input to the secondary coil was 90˚ out-of-phase with respect to the output from the PZT. The output from the magnetoelectric sensor was not linear. To obtain the MDS of the sensor we used extrapolation. We observed that the 2nd order polynomial trendline was a perfect fit for all the data taken for the ten sensors (see Figure 4.13). The 2nd order polynomial function saturated before reaching the noise-floor. In the case of the ferromagnetic MEMS sensor, the point of interaction between the trendline and the noise-floor gave the MDS (see Figure 4.14). To eliminate this, we considered the onset of saturation in the polynomial function as the MDS. In some cases, the parametrically amplified (PA) MDS was more than the no feedback (NF) case, which is not possible. To eliminate this MDS of NF was calculated and using the average amplification achieved for that sensor using parametric amplification, the MDS at PA was obtained. The MDS and sensitivity for all the sensors were compared (see Figure 4.15). MDS for the parametric amplification case for the ten sensors varied from 4 fT to 1 pT, whereas in the event of no feedback used the MDS ranged from 19.6 fT to 3.3 pT. The sensitivity, on the other hand, varied from 1.75-0.1 mV/nT for parametric amplification and 0.5-0.05 mV/nT in the case of no feedback. From the Equation (4.5) it can be seen that the magnetoelectric (ME) voltage coefficient is the sensitivity divided by the thickness of the PZT layer. Hence, the ME coefficient, too, can be easily calculated.

While characterizing the magnetoelectric sensor most of the signal improvement techniques were the same as used for the ferromagnetic MEMS sensors. The conventional techniques used were parametric amplification, noise reduction and shielding, and concentrators. We, however, did not incorporate vacuum, external bias for

‘*k*’ control, surface field dependency and foot-mass variation for sensitivity and MDS reported.

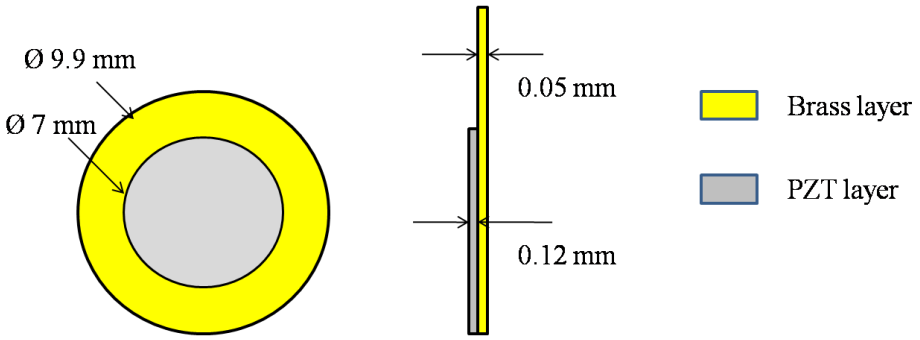

Figure 4.1. Schematic representation of the PZT disc used for the fabrication of the magnetoelectric sensor.

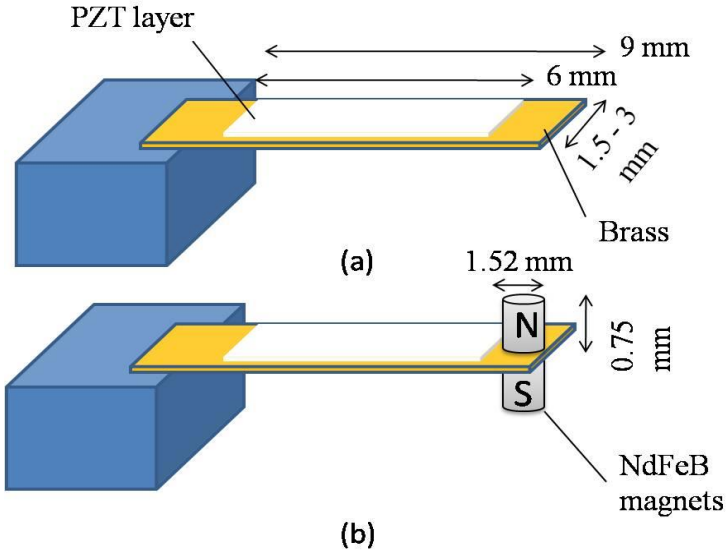

Figure 4.2. Diagrammatic representation of the magnetoelectric magnetometer (a) without and (b) with neodymium magnet as a foot-mass.

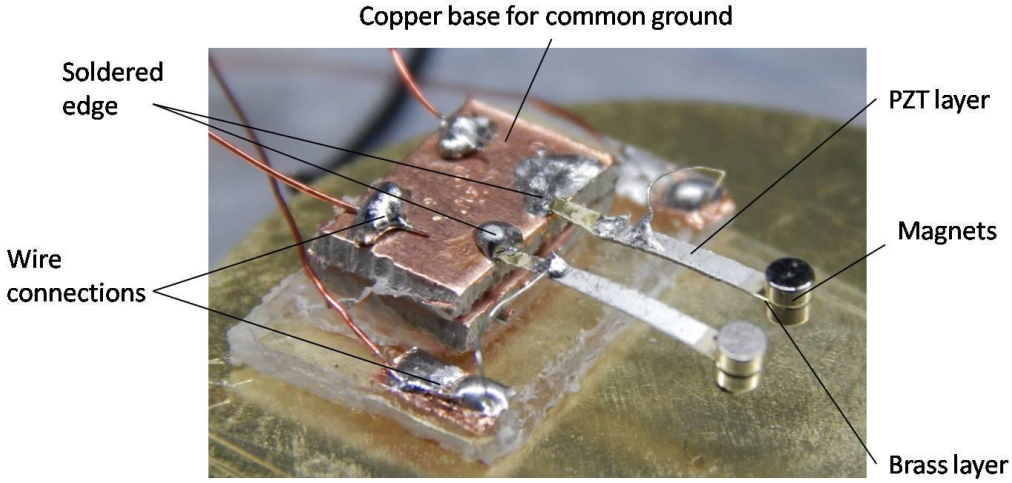

Figure 4.3. Optical image of the magnetoelectric magnetometer.

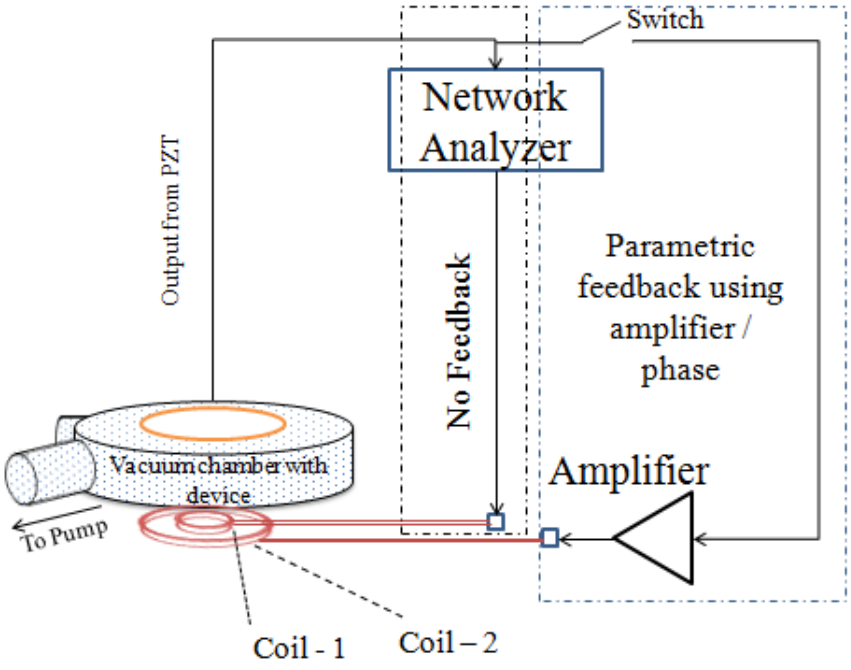

(a)

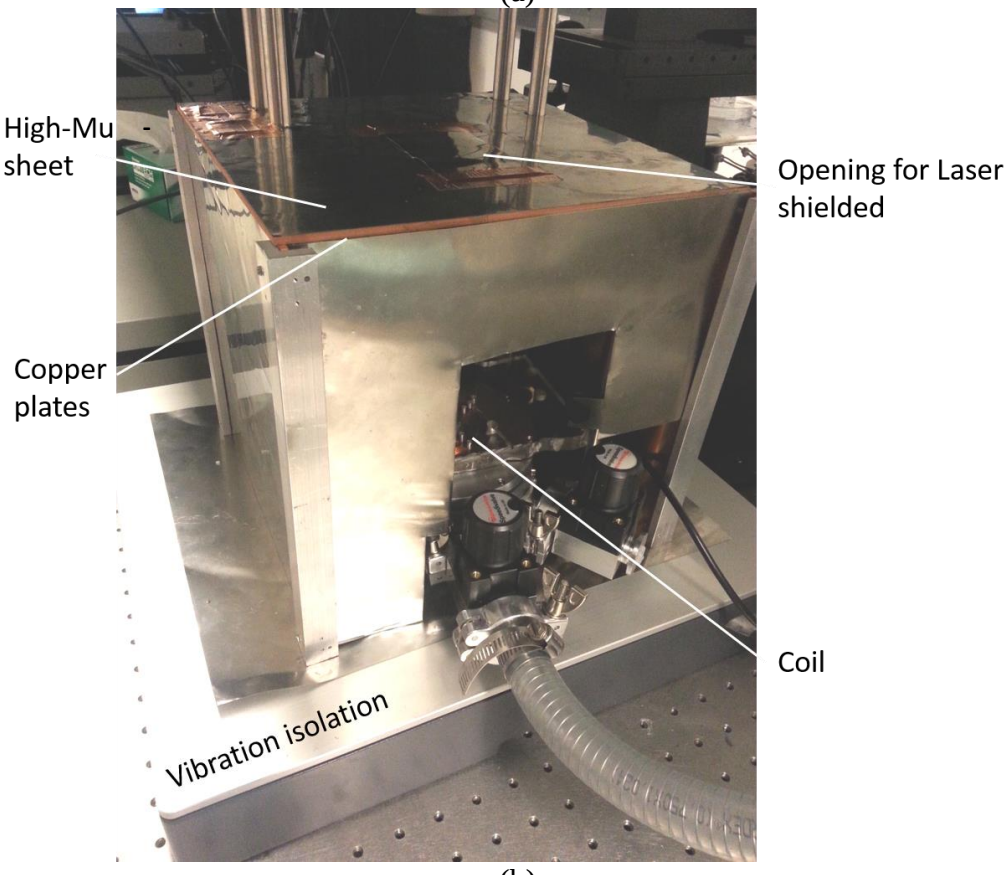

(b)

Figure 4.4. (a) Layout of the experimental set-up used for testing the magnetoelectric sensor (b) Optical image of the set-up.

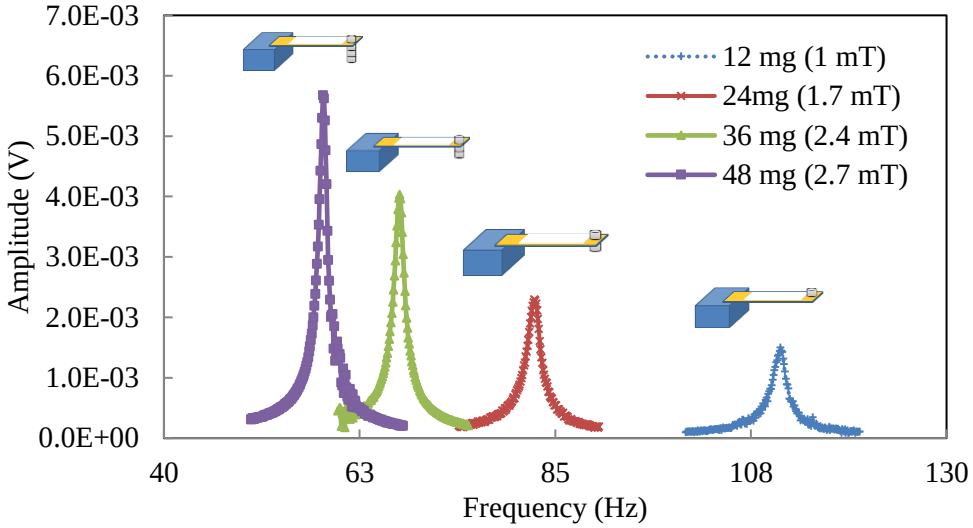

(a)

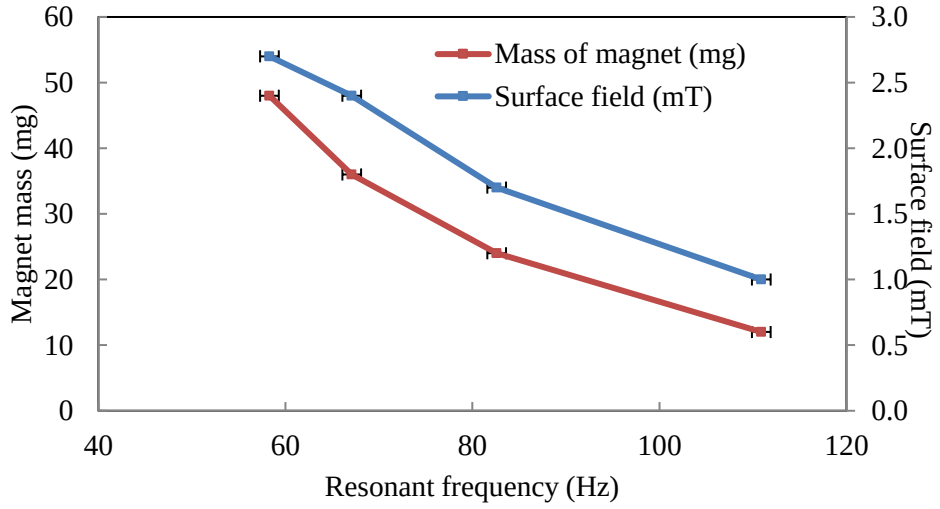

(b)

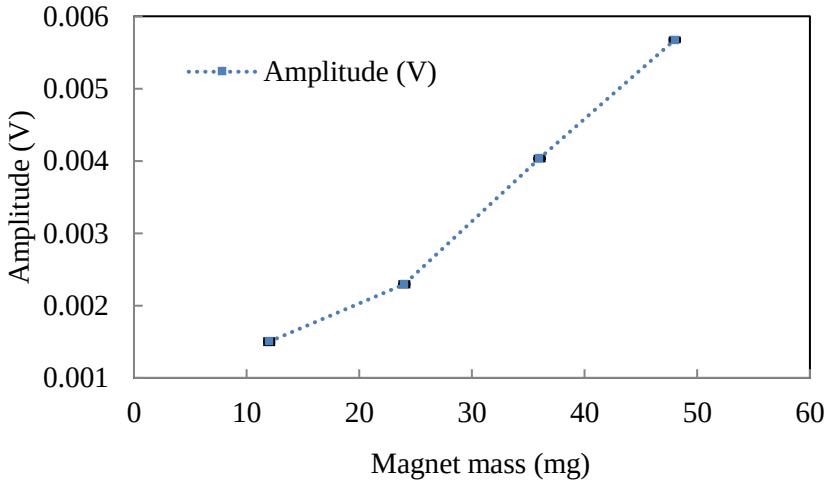

(c)

Figure 4.5. Graphs showing variation in (a) the spectrum (b) the resonant frequency and, (c) the output for different foot-mass (permanent magnet) surface magnetic field.

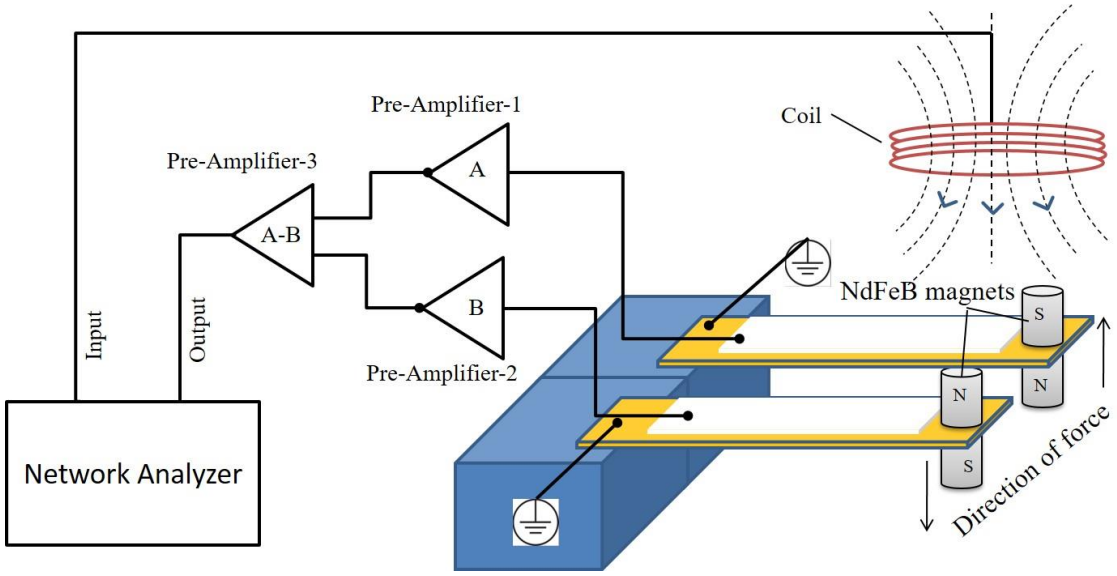

Figure 4.6. Schematic of coupled beams with the permanent magnets in opposite polarity and the setup used to detect the output.

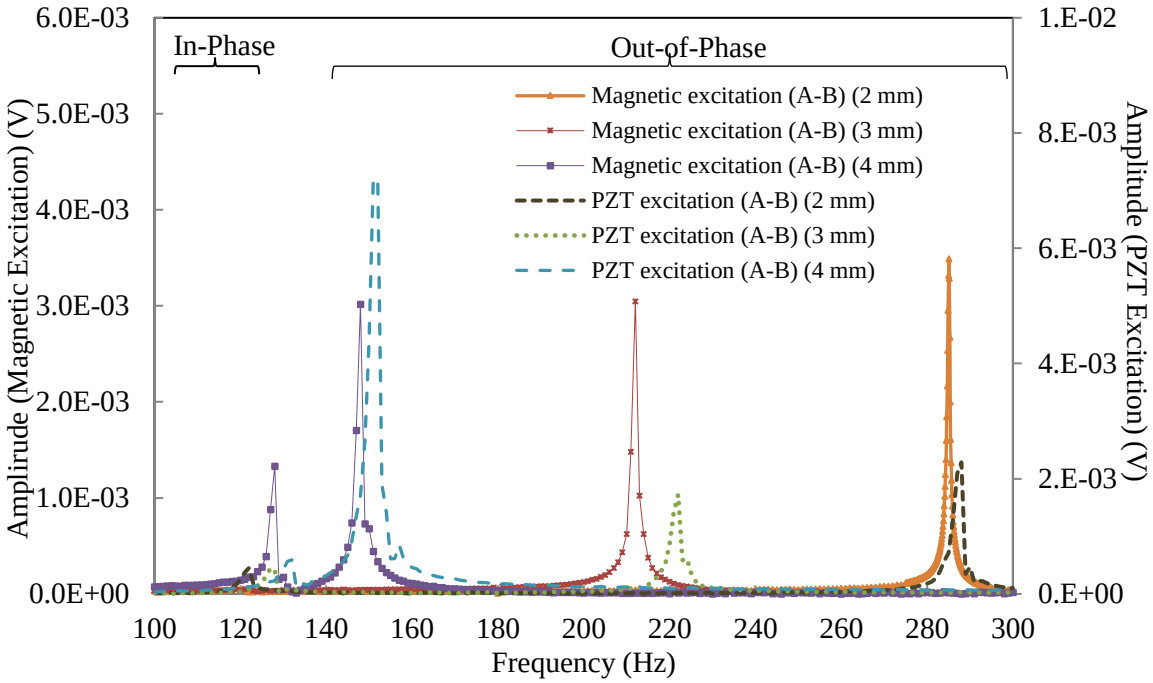

Figure 4.7. Spectrum showing coupled response for the magnetoelectric sensors (N9 and N10).

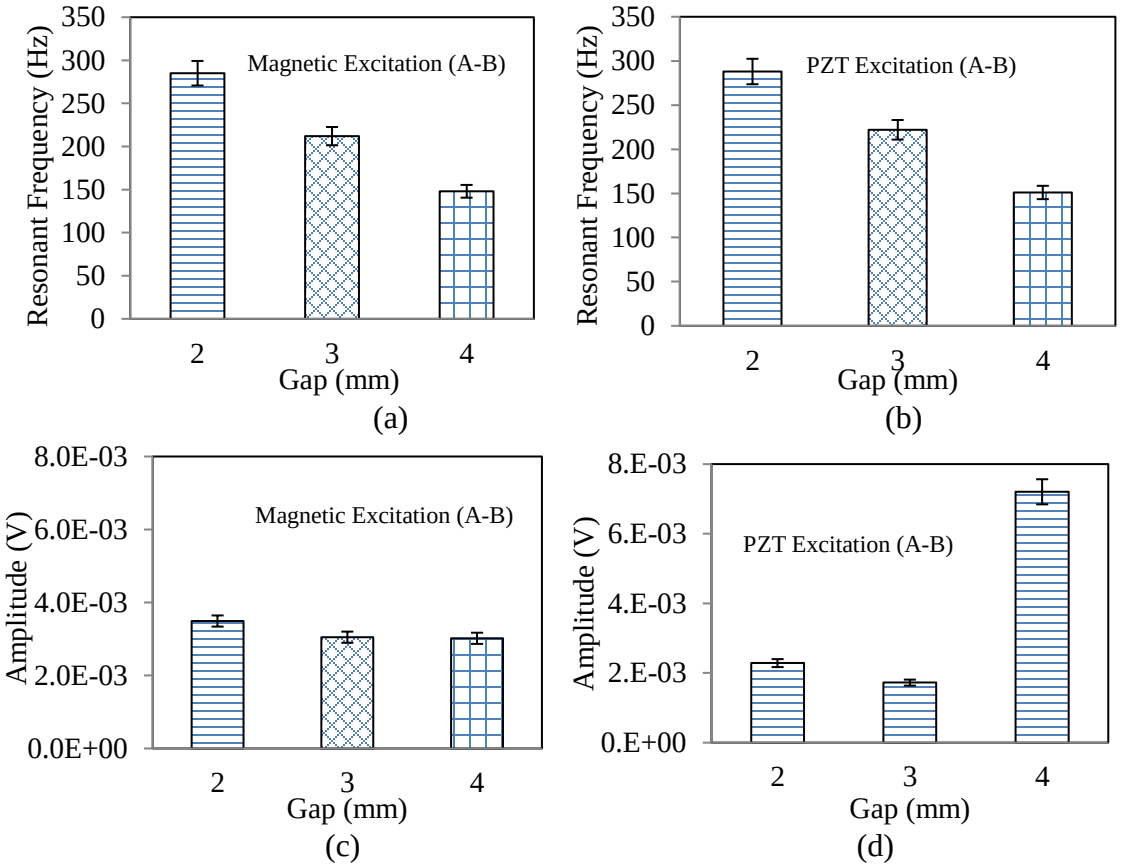

Figure 4.8. A Graph comparing the resonant frequency and the output from the coupled resonator as a function of the coupling gap and type of excitation.

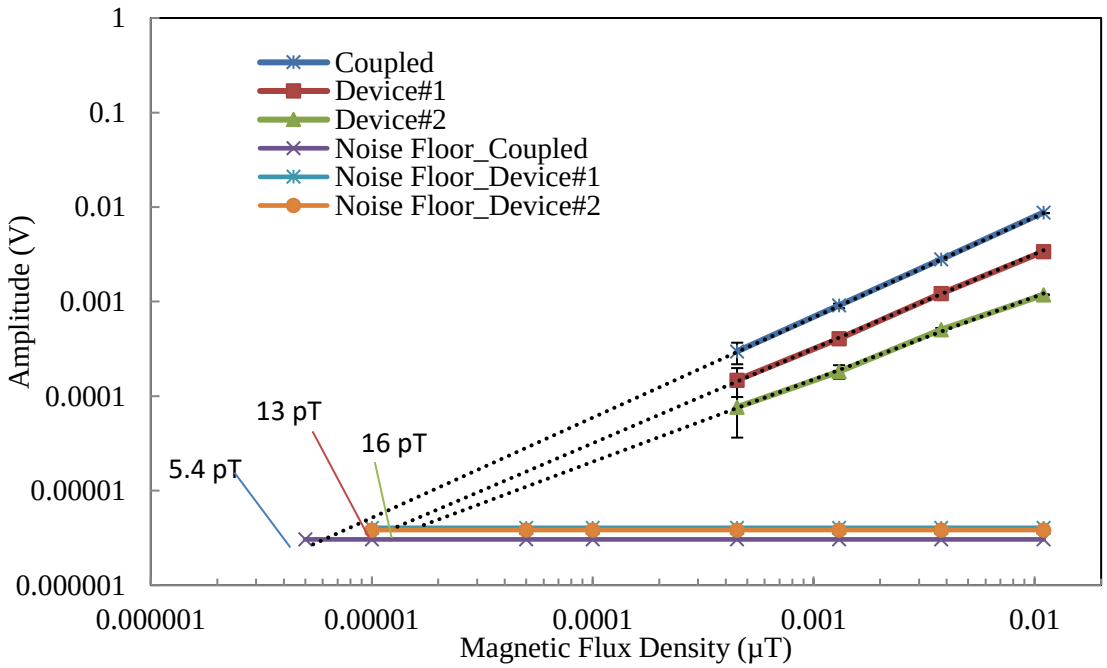

Figure 4.9. Comparison of MDS for individual magnetoelectric magnetometers (device #1 and device #2) with the coupled-mode resonator.

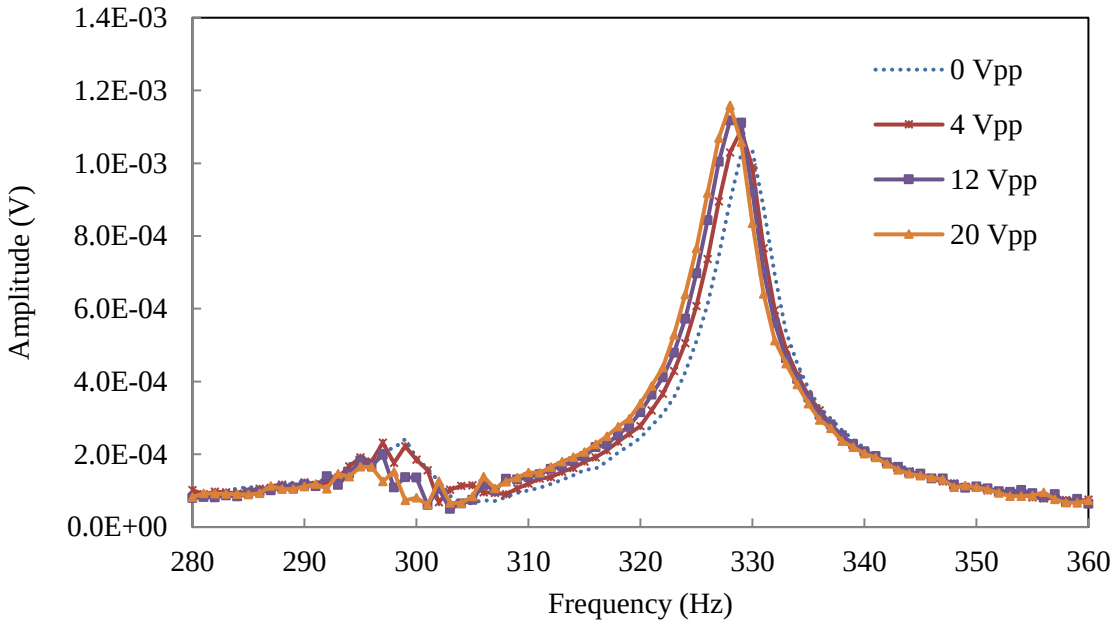

(a)

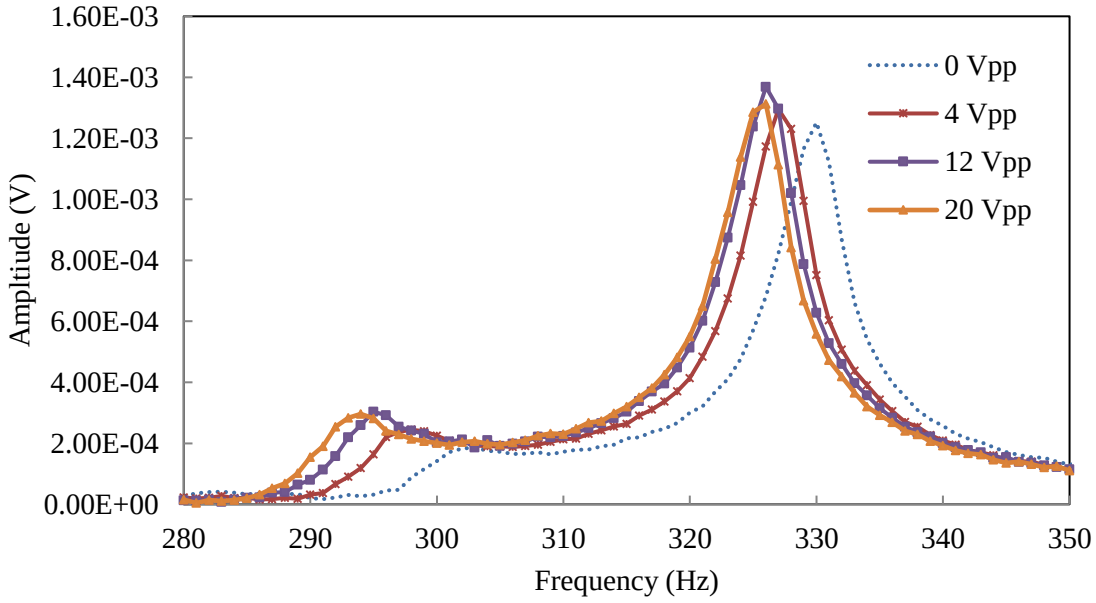

(b)

Figure 4.10. Spectrum showing variation of the resonant frequency and the amplitude with a) resonator-1 as driver and resonator-2 as detector b) resonator-2 as driver and resonator-1 as detector.

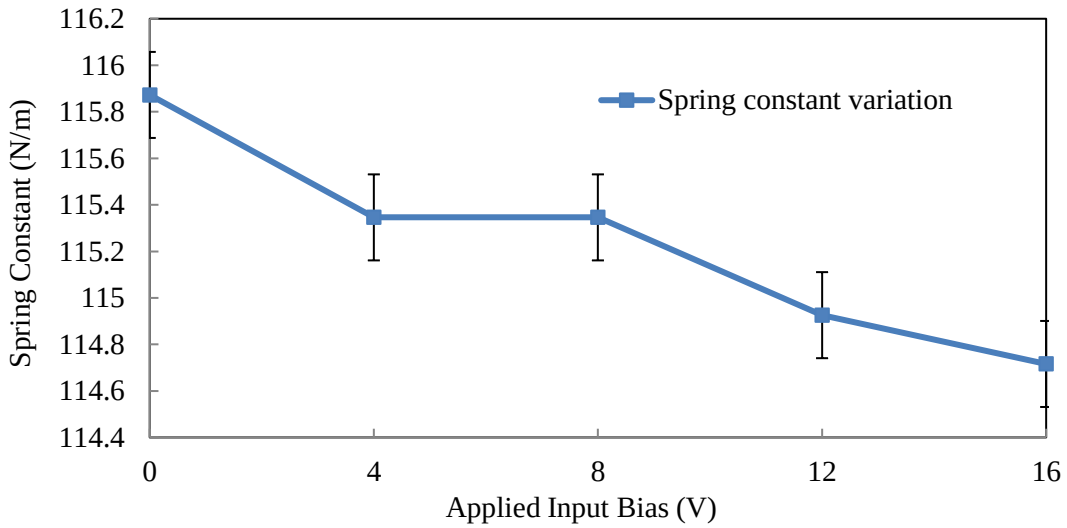

(a)

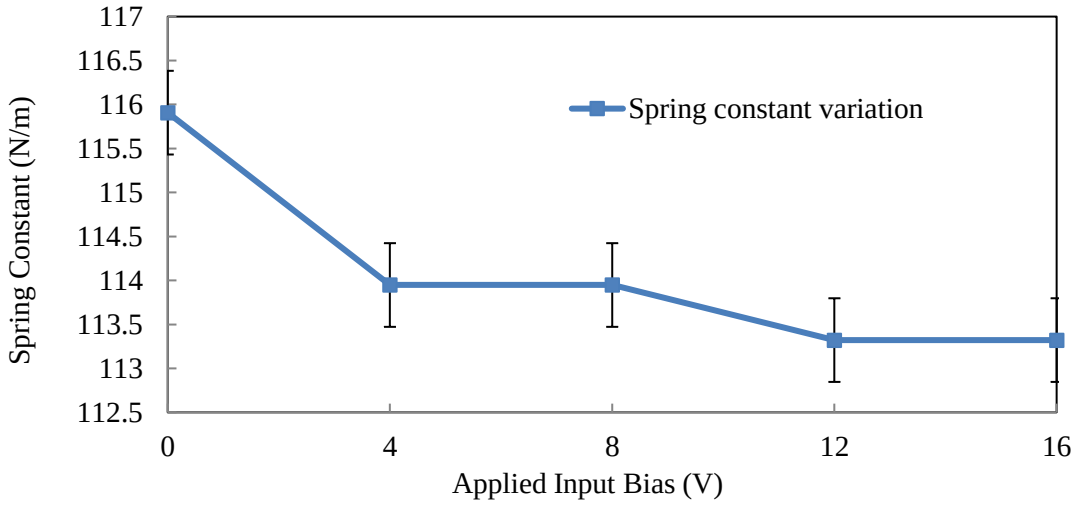

(b)

Figure 4.11. Graph showing variation of the spring constant with a) resonator-1 as driver and resonator-2 as detector b) resonator-2 as driver and resonator-1 as detector.

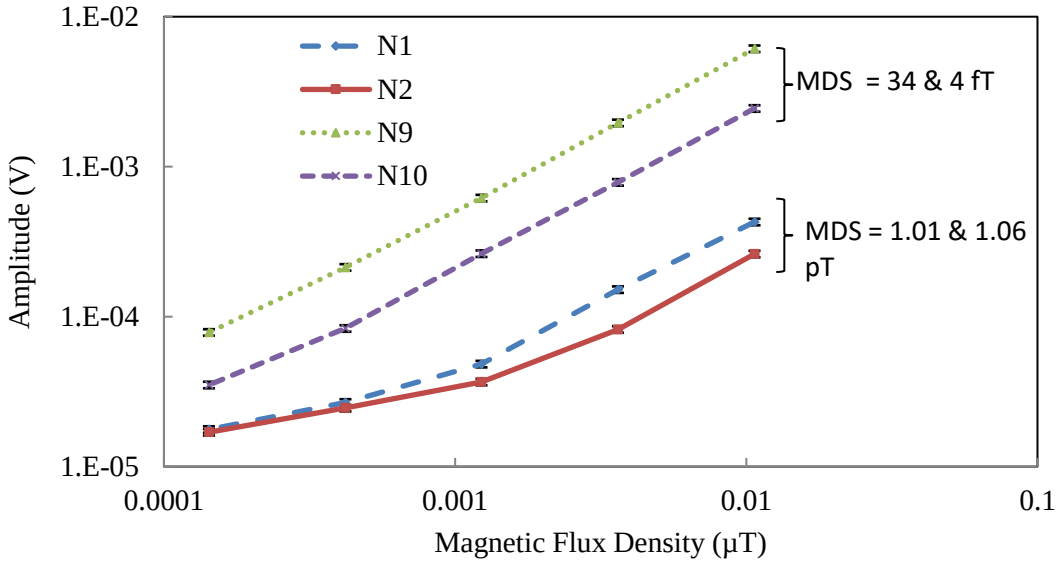

(a)

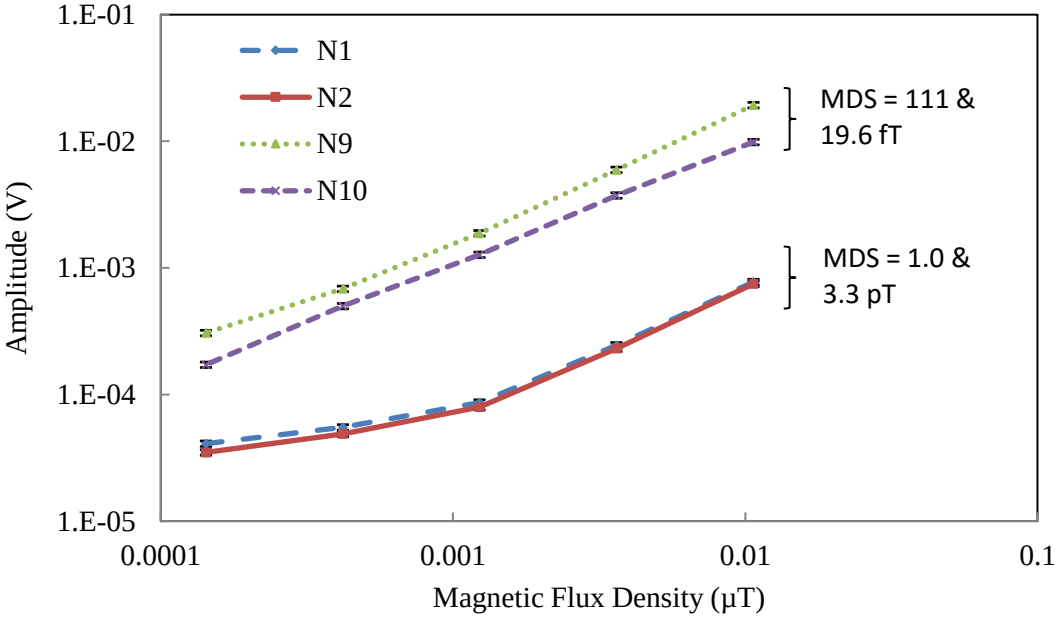

(b)

Figure 4.12. Graphical comparison of output for the best (N9 & N10) and the worst (N1&N2) devices using (a) parametric amplification (b) no feedback.

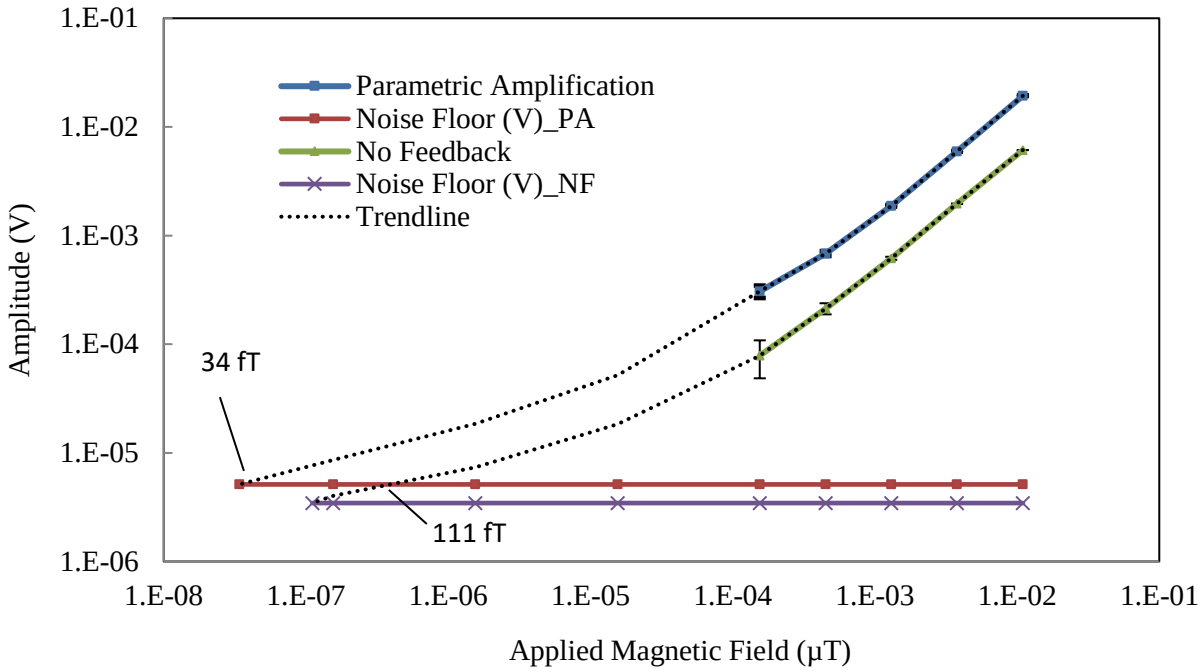

(a)

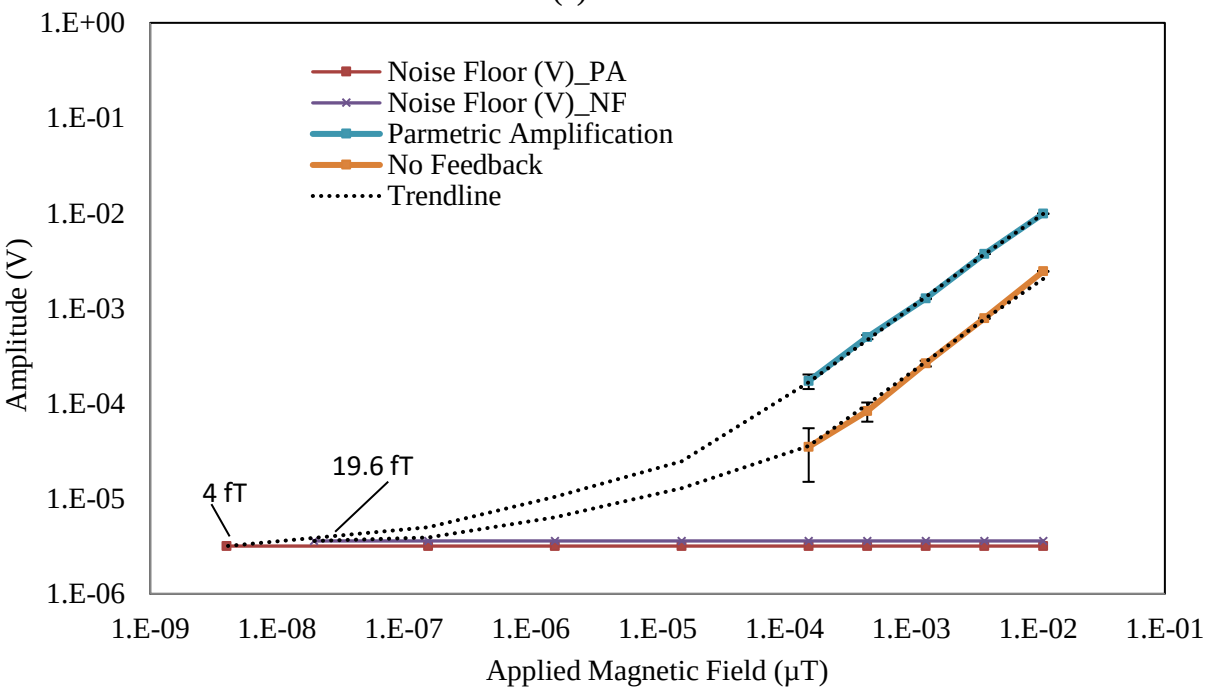

(b)

Figure 4.13. Result comparing the MDS for parametric amplification and no feedback for (a) N9 and (b) N10.

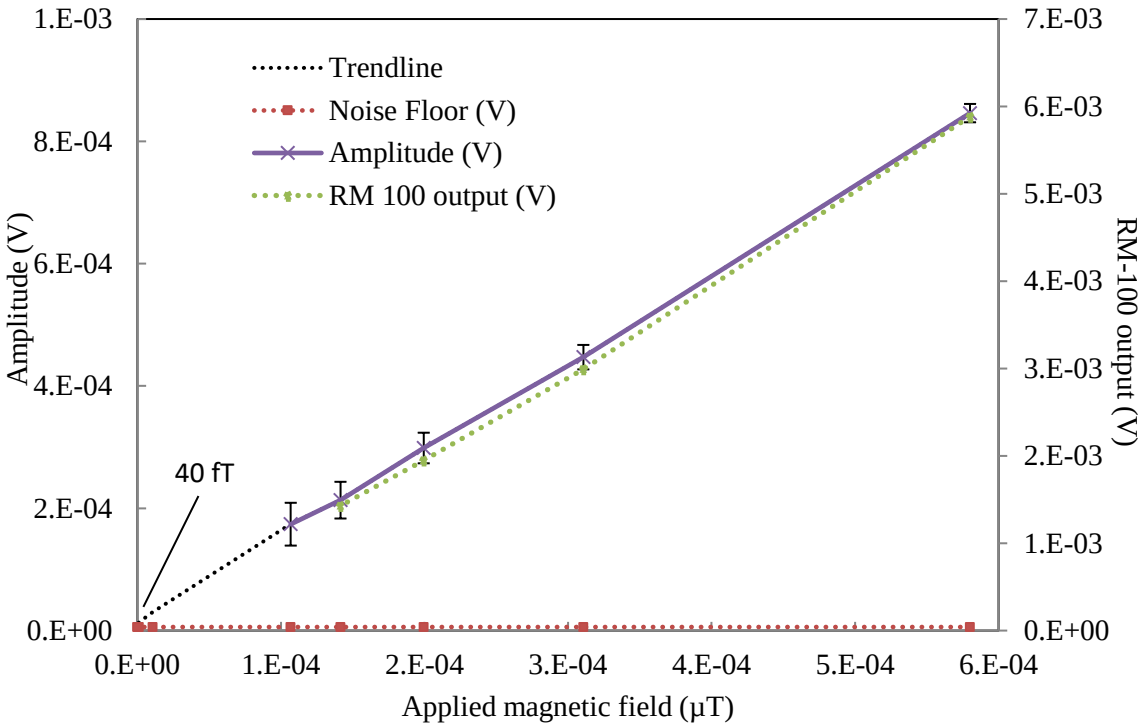

Figure 4.14. Comparison of the output from N9 with RM-100 output at lower magnetic field.

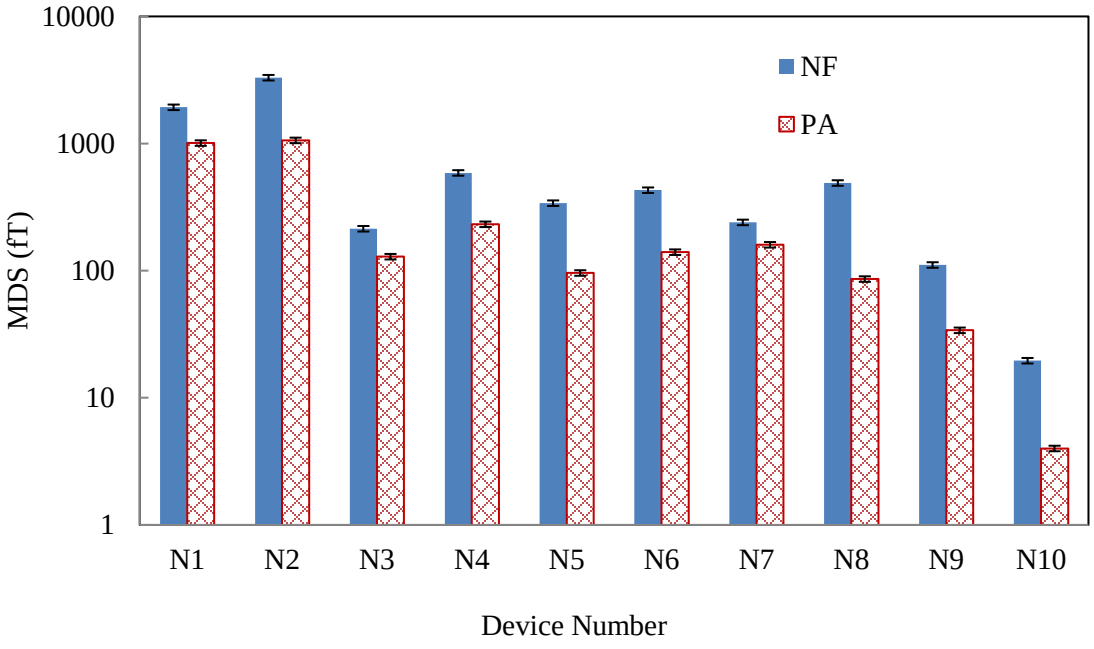

(a)

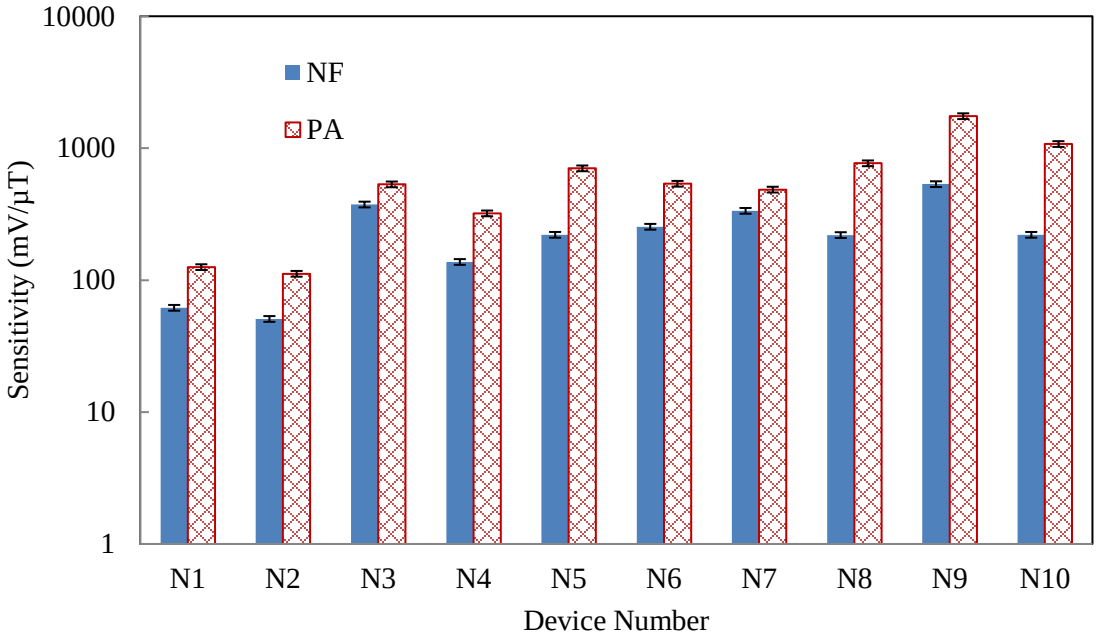

(b)

Figure 4.15. Comparison of the (a) MDS (b) sensitivity for the various magnetoelectric sensors used. The output was extrapolated using 2nd order polynomial function.

CHAPTER 5

CONCLUSION

Two different MEMS magnetometers were designed and characterized in this work. The first sensor was a ferromagnetic magnetometer, with 27 pT and 0.67 mV/nT sensitivity. The second sensor was a magnetoelectric magnetometer with MDS of ~40fT and 1.63 mV/nT sensitivity. Using a magnetoelectric magnetometer improved the MDS by 675 times and the sensitivity by a factor of 2.5. The external bias levitating the sensor was shown to increase the amplitude by relieving the built-in stress of the sensor. Parametric amplification was used to improve the MDS by a factor ~1000 and the sensor sensitivity by ~600.

In Chapter 1 we discussed how the magnetic field is generated in the neurons. The information from one neuron to another is transferred through synapses (10^{14}-10^{15}) forming a signal transmission pathway. We also discussed that this signal transfer is the result of a series of chemical changes, which is a reaction to an external stimulus. This signal transfer through the neuron produced a very feeble electric current.A synchronized axon current induced a detectable weak magnetic field. Thus, the magnetic field to be detected was produced by electric current flowing in neurons and was found to be of the order 10 fT-1 pT. We then discussed the current technology (EEG/MEG) used for mapping the brain. First, we discussed the similarities and differences in the functioning of EEG and MEG, followed by a detailed working principle of the two.

Electroencephalography (EEG) and Magnetoencephalography (MEG) measures the electrical and the magnetic signal respectively, at the surface of the skull produced by the combined current produced in neuron bundles. MEG in comparison to EEG has the potential to measure very high temporal as well as spatial resolution. The similarity between the two was that they are completely noninvasive techniques. We then discussed the working principle, advantages, and disadvantages of SQUIDs, a type of MEG. After reviewing the origin and strength of the magnetic field that we needed to measure, we discussed the approach we used for the sensor design, fabrication and characterization. We fabricated a MEMS ferromagnetic sensor (Si_3N_4 based) and a magnetoelectric sensor (PZT based) for magnetic field detection. The ferromagnetic MEMS sensor comprised of 4 different structures, namely: 3-leg bridge (4 mm × 2 mm × 1 μm), plus bridge (6-10 mm × 1-4 mm × 1 μm), fixed-fixed bridge (6-10 mm × 1-4 mm × 1 μm), and diaphragm (6-10 mm × 6-10 mm × 1 μm). The magnetoelectric magnetometer was a fixed-free beam. After selecting the sensor design, and the foot-mass material (NdFeB magnet), the sensors were fabricated using microfabrication techniques. To maximize the output our approach was to study the dynamics of the flexure beam structures and change the beam parameters electronically (mass, damping coefficient and spring constant). Using a set of Equations, we analyzed how the displacement in a flexure structure varied with input force.

The response of a sensor can be improved by electronically changing the parameters affecting the beam dynamics. We discussed the signal improvement strategies in detail. We analyzed that various physical and electronic techniques could be used that directly or indirectly impact the sensor parameters. Six such techniques were discussed (spring

constant adjustment, shielding, and concentrators, parametric amplification, coupled resonators, electronic noise reduction, and vacuum).We used external bias producing varying flux densities (+28 mT to -28.75 mT) to study the effect on the sensor amplitude. The output was increased for one polarity of the external bias with a decrease in the resonant frequency and a reverse effect on both the parameters for the other polarity of bias seen. Using 80% nickel-iron-molybdenum alloy (high-Mu sheet) with 0.006" thickness,the effect of the stray magnetic field from overhead power lines, earth's magnetic field and nearby equipment was reduced. A 20% reduction in noise-floor was observed by the use of shielding. The second signal improvement strategy used was parametric amplification. In this case, output from the sensor was given to a feedback loop that produced a 90^{o} out of phase signal with respect to the sensor's signal using a preamplifier. The gain of this signal was varied to achieve the highest possible sensor output while maintaining its stability. To further improve the signal from a sensor coupled resonator was discussed. Using two beams with similar dimensions and resonant frequency, the effective spring constant of the sensor was varied because of coupling. The amplitude of vibration in common mode was reduced, whereas in the opposite mode of vibration it improved the amplitude by 2-5 times. The fourth signal improvement strategy was electronic noise cancellation. The noise was controlled in the sensor by use of active and passive methods. Active noise reduction was achieved due to parametric amplification (electronic). A reduction of 3 mV noise was achieved at each step as measured using the oscilloscope. We also observed that optical transduction was ten times noisier than PZT transduction. The resonant amplitude of the MEMS ferromagnetic sensor increased 2 times when the sensor was subjected to 1 mTorr

(Atmospheric pressure = 1 Torr), pressure inside an aluminum sample holder with an optical window. Using a vacuum, the damping coefficient was reduced considerably hence, an improvement in sensor output was observed.

The material and equipment for sensor fabrication and testing were discussed after the signal improvement strategies. The choice of material for sensor fabrication depends on the Young's modulus and density component.). Silicon nitride was used for the MEMS version of the sensor supported by silicon frame. A rare earth neodymium (NdFeB) magnet was used at the center of the sensor to enhance the sensitivity. High-Mu sheets (0.006") were attached to thick copper plates to reduce the effect of stray magnetic fields. Coils made out of copper were used to produce the excitation magnetic field (Ø=3 cm) and the parametric feedback signal (Ø=5.5 cm). A plexy glass frame was used to support the coils. For coil calibration, the input was maintained at 510 Hz away from the DC frequency and 60 Hz harmonics. RM-100 was used for coil calibration. A network analyzer was used for providing input to the coil and detecting the output. The displacement in ferromagnetic MEMS sensor was detected using a Polytec laser Doppler vibrometer. Preamplifiers were used for impedance matching as well as providing proper gain for the feedback signal in case of parametric amplification. A signal generator was used to provide input at resonant frequency of the sensor, for the adjustment of the permanent magnet on the sensor, right at the center of the coil. We then discussed the transduction techniques that were used in our experiment. Three different transduction techniques, namely: Optical, Piezoelectric, and Magnetostrictive were used. A 633 nm laser was used for optical transduction. Voltage was generated from PZT beam due to piezoelectric effect when subjected to an external force.

The ferromagnetic MEMS sensor was then discussed in detail with emphasis on the experimental results obtained. Low pressure chemical vapor deposition (LPCVD) was used to deposit 1-2 μm thick silicon rich nitride layers at 825 ˚C. The built-in stress and gravitational force gave an estimate of sensor displacement (6.7 μm), using simulation. To simulate the effect of external bias, an external stress of 4.1E8 (N/m^2) was applied, resulting in a reduction of displacement by 0.08 μm. We next discussed the characterization results in detail. The biasing magnetic field improved the sensor output by 11-24 μV above 139 μV (no bias) at 463 Hz excitation. The external bias was varied from –28.75 mT to +28.75 mT in the z-direction which, was also the direction of the sensor's field. The MDS of 27 pT was obtained using linear extrapolation from the lowest magnetic flux density to zero. The MDS range for device #2 was 61 pT–533 pT without feedback and 1 pT–176 pT with parametric amplification. For 0.1 μT input magnetic flux the gain used was just 10. However, for 7 nT, 1 nT, and 0.5 nT input the gain used were 100, 500, and 5000, respectively. The RMS noise-floor around resonant peak was 77 μV for parametric amplification and 67 μV without any feedback. The noise-floor was observed to be less by a factor of 1.2 with the decrease in input. A 2 Hz bandwidth measurement provided a much lower noise when compared to 30 Hz. The effect of temperature on the sensor parameters was also discussed. The resonant frequency of the MEMS ferromagnetic sensor structure varied with temperature. The change was found to be 0.05 Hz/˚C. The change was 0.05 Hz/°C resulting in a 12 pV/pT/°C variation in temperature coefficient for 224 mV input.

We then moved on to the magnetoelectric magnetometer. The magnetoelectric magnetometer had low resonant frequency when compared to the PZT based sensors, as

we intend to use it for detection of ultra-low frequency magnetic fields (10-100 Hz). The magnetoelectric effect was seen to be a combined effect of piezoelectric and magnetostrictive transduction. PZT beams of varied dimension (9 mm × 1.5–3 mm × 0.17 mm) were fabricated. We intended to show the coupled mode response of the magnetoelectric sensor due to magneto-electric coupling as well, hence, sensors were fabricated in sets.The substrate was made of brass with a thickness of 0.05 mm whereas the PZT layer had a thickness of 0.12 mm. The AC magnetic field generated by the inner coil (Ø=3 cm) was applied directly perpendicular to the beam length. MDS for the parametric amplification case for the ten sensors varied from 4 fT to 1 pT, whereas for the no feedback case, the MDS varied from 19.6 fT to 3.3 pT. The sensitivity, on the other hand, varied from 1.75-0.1 mV/nT for parametric amplification and 0.5-0.05 mV/nT in the case of no feedback.

Lastly, we discussed some strategies that could be used to further improve the sensor MDS and sensitivity. For our experimentation, the foot-mass (NdFeB magnet) used for the sensors was 0.24 gm. Increasing the magnet mass increased the surface magnetic field. This improved the signal output by a factor of 2.47. The sensors were then tested in coupled mode. The phase and amplitude of the two sensors were matched before doing the testing. Using coupled-mode, an amplification of 2.37 was obtained. As observed in the case of ferromagnetic MEMS magnetometer reducing the damping on the sensor improved the quality factor. The same can be used for the magnetoelectric magnetometer to improve sensor’s MDS. Thus, ultra-sensitive magnetometers were designed, fabricated and tested, that can be used for mapping the magnetic signature of the human brain.

APPENDIX

List of Projects Worked on During MS

1. Ferromagnetic Silicon Nitride based MEMS Magnetometer for Brain Imaging.
2. Magnetoelectric PZT based MEMS Magnetometer for Brain Imaging.
3. Noninvasive monitoring of electrical parameters of *Schefflera arboricola* leaf.
4. Remote power transfer using magneto-electric devices.
5. Monitoring Yeast Activation with Sugar and Zero Calorie Sweetener using Terahertz Waves.
6. Temperature sensing using ultrasensitive MEMS device.
7. Silver Sulfide MOSFET with 7 mV/decade sub-threshold slope.
8. Energy harvesting from ambient environmental conditions using magneto-piezo electrics.
9. Use of Vanadium (IV) Oxide state transition for actuation.
10. Gate field effect using Vanadium (IV) Oxide active channel on MOSFET.

Publications/ Presentations

1. **Kushagra Sinha**, Olutosin C. Fawole, and Massood Tabib-Azar, "Noninvasive monitoring of electrical parameters of *Schefflera arboricola* leaf," *IEEE Sensors conf. 2015*, pp. 1-4.
2. **Kushagra Sinha,** and Massood Tabib-Azar, "Effect of light and water on *Schefflera* plant electrical properties," *Science Domain*, 2016/JSRR/19174, vol. 9, no. 4, pp. 1-11, 2016.
3. **Kushagra Sinha**, Rugved Likhite, and Massood Tabib-Azar, "High sensitivity silicon nitride MEMS magnetometer for brain imaging," *USTAR Conf., poster presentation*, 2015.

4. **Kushagra Sinha,** and Massood Tabib-Azar, “Remote power transfer using magneto-electric devices,” *PowerMEMS conf. 2015*.

5. **Kushagra Sinha,** and Massood Tabib-Azar, “27 pT silicon nitride MEMS magnetometer for brain imaging," *IEEE Sensors J.*, 2016, In Press.

6. Olutosin Fawole, **Kushagra Sinha**, and Massood Tabib-Azar, “Monitoring yeast activation with sugar and zero calorie sweetener using terahertz waves,” *IEEE Sensors conf. 2015*.

7. Wenyuan Zhu, **Kushagra Sinha**, and Massood Tabib-Azar, "Temperature sensing using ultrasensitive MEMS device," *USTAR Conf.*, poster presentation, 2015.

8. Olutosin Fawole, **Kushagra Sinha**, Rugved Likhite, Mitchell Terry, and Massood Tabib-Azar "Novel terahertz circuits and novel applications of Terahertz Waves," *USTAR Conf.*, poster presentation, 2015.

REFERENCES

[1] The White House "Brain initiative," [Online]. Available: https://www.whitehouse.gov/share/brain-initiative.

[2] S. Herculano-Houzel, "The remarkable, yet not extraordinary, human brain as a scaled-up primate brain and its associated cost," *Proc. Natl. Acad. Sci.*, vol. 109, no. 1, pp. 10661–10668, 2012.

[3] Institute for Learning & Brain Sciences, University of Washington, "What is magnetoencephalography (MEG)?," [Online]. Available: http://ilabs.washington.edu/what-magnetoencephalography-meg.

[4] M. A. Caliskan, "Introduction to neural networks – part 1: the neuron," *Delphi Science* [Online]. Available: https://delphiscience.wordpress.com/category/scientific-programming/biological-modeling.

[5] M. Hamalainen, R. Hari, R. J. Ilmoniemi, J. Knuutila, and O. V. Lounasmaa, "Magnetoencephalography theory, instrumentation, and applications to noninvasive studies of the working human brain," *Rev. Mod. Phys.*, vol. 65, no. 2, pp. 413-497, 1993.

[6] M. D. Michelenaa, F. Monterob, P. Sáncheza, E. Lópezc, M.C. Sánchezc, and C. Arocaa, "Piezoelectric–magnetostrictive magnetic sensor using stripe actuators," *J. Magn. Magn. Mater.*, vols. 242–245, no. 2, pp. 1160-1162, 2002.

[7] B. Piekarskia, M. Dubey, E. Zakar, R. Polcawich, D. Devoe, and D. Wickenden, "Sol-gel pzt for mems applications," *Integr. Ferroelectr.*, vol. 42, no. 1, pp. 25-37, 2002.

[8] E. Zakar, R. Polcawich, M. Dubey, J. Pulskamp, A. Wickenden, J. Conrad, R. Piekarz, D. Wickenden, and J. Champion, "Pzt mems for an extremely sensitive magnetometer," *Integr. Ferroelectr.*, vol. 54, no. 1, pp. 697-706, 2003.

[9] A. Yariv, and H. V. Winsor, "Proposal for detection of magnetic fields through magnetostrictive perturbation of optical fibers," *Opt. Lett.*, vol. 5, no. 3, pp. 87-89, 1980.

[10] The United States of America as represented by the secretary of the navy "Rare earth-iron magnetostrictive materials and devices using these materials," US4308474, Dec 29, 1981.

[11] D. K. Wickenden, T. J. Kistenmacher, R. Osiander, S. A. Ecelberger, R. B. Givens,

and J. C. Murphy, "Development of miniature magnetometers," *Johns Hopkins APL. Tech. Dig.*, vol. 18, no. 2, pp. 271-278, 1997.

[12] H. H. Yanga, N. V. Myungb, J. Yeea, D. Y. Parkb, B. Y. Yoob, M. Schwartzb, K. Nobeb, and J. W. Judya, "Ferromagnetic micromechanical magnetometer," *Sensor Actuat. A: Phys.*, vols. 97–98, pp. 88–97, 2002.

[13] J. K Yeea, H. H Yangb, and J. W Judya, "Shock resistance of ferromagnetic micromechanical magnetometers," *Sensor Actuat. A: Phys.*, vol. 103, no. 1–2, pp. 242–252, 2003.

[14] D. Anderson, A. Anghel, J. Chau, and O. Veliz, "Daytime vertical e × b drift velocities inferred from ground-based magnetometer observations at low latitudes," *SpWea. J.*, vol. 2, no. 11, 2004.

[15] S. de Haan, and J. C. Lodder, "The (anomalous) hall magnetometer as an analysis tool for high density recording media," *J. Magn. Soc. Jpn.*, vol. 15, pp. 349-354, ISSN 0285-0192, 1991.

[16] A. Frangi, B. De Masi, G. Langfelder, and D. Paci, "Optimization of lorentz-force mems magnetometers using rarefied-gas-theory," *IEEE Sensors J.*, pp. 659-662, 2013.

[17] M. Li, S. Sonmezoglu, and D. A. Horsley, "Extended bandwidth lorentz force magnetometer based on quadrature frequency modulation," *J. Microelectromech. Syst.*, vol. 24, no. 2, pp. 333-342, 2015.

[18] G. Langfelder, and A. Tocchio, "Operation of lorentz-force mems magnetometers with a frequency offset between driving current and mechanical resonance," *IEEE Trans. Magn.*, vol. 50, no. 1, 2014.

[19] S. Sonmezoglu, M. Li, and D. A. Horsley, "Force-rebalanced lorentz force magnetometer based on a micromachined oscillator," *App. Phys. Lett.*, vol. 106, 093504, 2015.

[20] Irene Karanasiou "Functional brain imaging using non-invasive non-ionizing methods: towards multimodal and multiscale imaging," Neuroimaging - methods, prof. Peter Bright (ed.), InTech, DOI: 10.5772/24601, 2012 [Online]. Available: http://www.intechopen.com/books/neuroimaging-methods/functional-brain-imaging-using-non-invasive-non-ionizing-methods-towards-multimodal-and-multiscale-i.

[21] R. J. Cooper, N. L. Everdell, L. C. Enfield, A. P. Gibson, A. Worley, and J. C. Hebden, "Design and evaluation of a probe for simultaneous eeg and near-infrared imaging of cortical activation," *Phys. Med. Biol.*, vol. 54, no. 7, pp. 2093–2102, 2012.

[22] F. Darvas, D. Pantazis, E. Kucukaltun-Yildirim, and R.M. Leahy, "Mapping human brain function with meg and eeg: methods and validation," *Neuroimage.*, vol. 23, pp.

S289-S299, 2004.

[23] H. Stefan, R. Tomioka, T. Dickhaus, C. Sannelli, B. Blankertz, G. Nolte, and Klaus-Robert Muller, "Large-scale eeg/meg source localization withspatial flexibility," *Neuroimage.*, vol. 54, no. 2, pp. 851-859, 2011.

[24] L. Cruces, Mind and Brain Laboratory-New Mexico State University "Electroencephalography principles," [Online]. Available: http://www-psych.nmsu.edu/~jkroger/lab/principles.html.

[25] Institute of Learning and Brain Sciences, University of Washington, "What is magnetoencephalography (MEG)," [Online]. Available: http://ilabs.washington.edu/what-magnetoencephalography-meg

[26] MEG International Services Ltd., "What is MEG and what makes CTF MEGTM the most advanced MEG technology in the world?," [Online]. Available: www.4dneuroimaging.com

[27] Los Alamos National Laboratory, "MEG helmet measurement," [Online]. Available: https://www.lanl.gov/quarterly/q_spring03/meg_helmet_measurements.shtml

[28] J. Knuutila, M. Kajola, H. Seppa, R. Mutikainen, and J. Salmi, "Design, optimization, and construction of a dc squid with complete flux transformer circuits," *J. Low Temp. Phys.*, vol. 71, no. 5, pp. 369-392, 1998.

[29] M. Li, V.T. Rouf, G. Jaramillo, and D.A Horsley, "Mems lorentz force magnetic sensor based on a balanced torsional resonator," *Transd. Eurosens.*, vol. 27, pp. 66-69, 2013.

[30] S. Marauska, R. Jahns, C. Kirchhof, M. Claus, E. Quandt, R. Knöchel, and B. Wagner, "Highly sensitive wafer-level packaged mems magnetic field sensor based on magnetoelectric composites," *Sensor Actuat. A: Phys.*, vol. 189, pp. 321-327, 2013.

[31] V. Kumar, M. Mahdavi, X. Guo, E. Mehdizadeh, and S. Pourkamali, "Ultra-sensitive lorentz force mems magnetometer with pico-tesla limit of detection," *IEEE Int. Conf. MEMS*, vol. 28, pp. 204 -207, 2015.

[32] D. Ren, L. Wu, M. Yan, M. Cui, Z. You, and M. Hu, "Design and analyses of a mems based resonant magnetometer," *Sensors J.*, vol. 9, no. 9, pp. 6951-6966, 2009.

[33] Z. Kádár, A. Bossche, and J. Mollinger, "Integrated resonant magnetic-field sensor," *Sensor Actuat. A: Phys.*, vol. 70, no. 3, pp. 225–223, 1998.

[34] N. Haned, and M. Missous, "Nano-tesla magnetic field magnetometry using an InGaAs–AlGaAs–GaAs 2deg hall sensor", *Sensor Actuat. A: Phys.*, vol. 102, pp. 216–222, 2006.

[35] A. Bertoldi, D. Bassi, L. Ricci, D. Covi, and S. Varas, “Magnetoresistive magnetometer with improved bandwidth and response characteristics”, *Rev. Sci. Instrum.*, vol. 76, no. 6, 065106, 2005.

[36] G. A. Wang, S. Arai, T. Kato, and S. Iwata, “Low-drift giant magnetoresistive field sensor using modulation of free-layer magnetization direction,” *J. Phys. D: Appl. Phys.*, vol. 44, no. 23, pp. 235003, 2011.

[37] T. Liakopoulos, and C.H. Ahn, “A micro-fluxgate magnetic sensor using micromachined planar solenoid coils,” *Sensor Actuat. A: Phys.*, vol. 77, pp. 66–72, 1999.

[38] S. Yabukami, T. Suzuki, N. Ajiro, H. Kikuchi, M. Yamaguchi, and K. Arai, “A high frequency carrier-type magnetic field sensor using carrier suppressing circuit,” *IEEE Trans. Magn.*, vol. 37, no. 4, pp. 2019–2021, 2001.

[39] P. Pai, L. Chen, and M. Tabib-Azar, "Fiber optic magnetometer with sub-pico tesla sensitivity for magneto-encephalography," *IEEE Sensors J.*, pp. 722-725, 2014.

[40] J. S. Beasley, and G. M. Miller, “Modern electronic communication (9th ed.),” ISBN 978-0132251136, pp. 4-5, 2008.

[41] S. Timoshenko, D.H. Young, and W. Weaver Jr., “Vibration problems in engineering,” 4th ed., John Wiley & Sons Inc., USA, 1974.

[42] S. M. Han, H. Benaroya, and T. Wei, “Dynamics of transversely vibrating beams using four engineering theories,” *J. Sound Vib.*, vol. 225, no. 5, pp. 935-988, 1999.

[43] J. W. Tedesco, W. G. McDougal, and C. A. Ross, “Structural dynamics: theory and applications,” Addison Wesley Longman, Inc., California, 1999.

[44] D. Shen, J. H. Park, J. H. Noh, S. Y. Choe, S. H. Kim, H. C. Wikle, and D. J. Kim, “Micromachined pzt cantilever based on soi structure for low frequency vibration energy harvesting,” *Sensor Actuat. A: Phys.*, vol. 154, no.1, pp.103-108, 2009.

[45] D. Vokoun, M. Beleggia, L. Heller, and P. Sittner, “Magnetostatic interactions and forces between cylindrical permanent magnets,” *J. Magn. Magn. Mater.*, vol. 321, no. 22, pp. 3758–3763, 2009.

[46] Magnetic Shield Corporation “How do magnetic shields work?,” [Online]. Available: http://www.magnetic-shield.com/pdf/how_do_magnetic_shields_work.pdf

[47] Y. Yang, E. Ng, P. Polunin, Y. Chen, S. Strachan, CH Ahn, O. Shoshani, S. Shaw, M. Dykman, V. Hong, and T. Kenny, “Experimental investigation on mode coupling of bulk mode silicon mems resonators,” *IEEE MEMS Conf. 2015*, pp. 1008-11, 2015.

[48] Y. Xu, H. Zhu, and J.E.Y Lee, "Piezoresistive sensing in a strongly-coupled high q

lamé mode silicon mems resonator-pair," *Freq. Cont. Symp. (FCS), IEEE Int.*, pp. 1-5, 2014.

[49] A. Erbes, P. Thiruvenkatanathan, and A. A. Seshia, "Numerical study of the impact of process variations on the motional resistance of weakly coupled mems resonators," *2013 Joint UFFC, EFTF, PFM Symp.*, pp. 674-677, 2014.

[50] A. Erbes, P. Thiruvenkatanathan, and A. A. Seshia, "Impact of mode localization on the motional resistance of coupled mems resonators," *Freq. Cont. Symp. (FCS), 2012 IEEE Int.*, pp. 1-6, 2012.

[51] G. Umesh, B. M. Giridhar Nayak, and A. Deshpande, "Design and analysis of a capacitively-coupled clamped-clamped mems resonator," *2014 Sixth Int. Conf. Comp. Intelligence Comm. Net.*, DOI 10.1109/CICN.2014.46, 2014.

[52] M. Manav, G. Reynen, M. Sharma, E. Cretu, and A. S. Phani, "Ultrasensitive resonant mems transducers with tuneable coupling," *J. Micromech. Microeng.*, vol. 24, 055005 (10pp), 2014.

[53] P. Pai, H. Pourzand, and M. Tabib-Azar, "Magnetically coupled resonators for rate integrating gyroscopes," *IEEE Sensors J.*, vol. 935, pp. 1173–1176, 2014.

[54] M. Spletzer, A. Raman, A. Q. Wu, X. Xu, and R. Reifenberger, "Ultrasensitive mass sensing using mode localization in coupled micro cantilevers," *App. Phys. Lett.*, vol. 88, no. 25, pp. 254102, 2006.

[55] M. Spletzer, A. Raman, H. Sumali, and J. P. Sullivan, "Highly sensitive mass detection and identification using vibration localization in coupled microcantilever arrays," *Appl. Phys. Lett*., vol. 92, no. 11, p. 114102, Mar. 2008.

[56] P. Thiruvenkatanathan, J. Woodhouse, and A. A. Seshia, "Enhancing parametric sensitivity in electrically coupled mems resonators," *J. Microelectromech. Syst.*, vol. 18, no. 5, pp. 1077-86, 2009.

[57] Tzong-Lin Wu, "Microwave filter design," [Online]. Available: http://ntuemc.tw/upload/file/20110607122336d81d3.pdf.

[58] VU Bioengineering RET Program, School of Engineering, Vanderbilt University, " Magnetic fields matter," [Online]. Available: https://www.teachengineering.org/view_lesson.php?url=collection/van_/lessons/van_mri_lesson_9/van_mri_lesson_9.xml.

[59] J. M. Kilpatrick, V. T. Markov, and P. Enrico, "Vibration measurements by laser techniques: advances and applications," *8th Int. Conf. Vibr. Meas.. Las. Tech.: Adv.. App.*, pp. 7098-09, 2008.

[60] D. O. Zyatkov, A. V. Yurchenko, V. B. Balashov, and V. I. Yurchenko, "The

capacitive magnetic field sensor," *J. Phys.: Conf. Series*, vol. 671, 012065 (6 pp.), 2016.

[61] F. Ahmad, J. O. Dennis, M. H. Md Khir, and N. H. Hamid, "A cmos mems resonant magnetic field sensor with differential electrostatic actuation and capacitive sensing," *Adv. Matrl. Research*, vols. 403-408, pp. 4205-4209, 2011.

[62] M. Stifter, H. Steiner, A. Kainz, F. Keplinger, W. Hortschitz, and T. Sauter, "A lorentz force actuated magnetic field sensor with capacitive read-out," *Proc. SPIE Smart Sens. Actuators MEMS*, vol. 6, 87632E, 2013.

[63] J. Liu, and X. Li, "A piezoresistive microcantilever magnetic-field sensor with on-chip self-calibration function integrated," *Microelect. J.*, vol. 38, no. 2, pp. 210–215, 2007.

[64] V. Beroulle, Y. Bertrand, L. Latorre, and P. Nouet, "Monolithic piezoresistive cmos magnetic field sensors," *Sensor Actuat. A: Phys.*, vol. 103, no. 1–2, pp. 23–32, 2003.

[65] K. Tan, K. Ohmori, K. Itoi, K. Nagasu, Y. Uemichi, and T. Aizawa, "High sensitivity magnetic field sensor utilizing magneto-impedance effect," *Fujikura Giho*, vol. 3, no. 115, pp. 59-62, Dec. 2008.

[66] J. Kiser, P. Finkel, J. Gao, C. Dolabdjian, J. Li, and D. Viehland, "Stress reconfigurable tunable magnetoelectric resonators as magnetic sensors," *App. Phys. Lett.*, vol. 102, no. 4, 042909 (4 pp.), 2013.

[67] S. M. Gillette,T. Yajie Chen Fitchorov, O. Obi, J. Liping, H. Hongbo, and V.G. Harris, "Metglas-enhanced tube-topology magnetoelectric magnetic field sensor," *IEEE Trans. Mag.*, vol. 50, no. 11, 4005103 (3 pp.), 2014.

[68] G. Meyer, and N.M. Amer, "Erratum: novel optical approach to atomic force microscopy," *Appl. Phys. Let.*, vol. 53, no. 12, 1998.

[69] T. H. Stievater, W. S. Rabinovich, H. S. Newman, J. L. Ebel, R. Mahon, D. J. McGee, and P. G. Goetz, "Microcavity interferometry for mems device characterization," *J. Microelectromech. Syst.*, vol. 12, no. 1, pp. 109 – 116, 2003.

[70] W. Merlijin van Spengen, R. Puers, R. Mertens, and I. DeWolf, "Characterization and failure analysis of mems: high resolution optical investigation of small out-of plane movements and fast vibrations," *Microsys. Tech.*, vol. 10, no. 2, pp. 89-96, 2003.

[71] S. L. Firebaugh, H. K. Charles Jr., R. L. Edwards, A. C. Keeney, and S. F. Wilderson, "Optical deflection measurement for characterization of microelectromechanical systems (mems)," *IEEE Trans. Instr. Meas.*, vol. 53, no. 4, pp. 1047-1051, 2004.

[72] A. Bosseboeuf, and S. Petitgrand, "Characterization of the static and dynamic

behavior of m(o)ems by optical techniques: status and trends," *J. micromech. Microeng.*, vol. 13, no. 4, 2003.

[73] K. Sinha, R. Likhite, M. Gao, and M. Tabib-Azar, "High sensitivity silicon nitride mems magnetometer for brain imaging," *USTAR Confl., 2015*.

[74] University of Minnesota, "Proximal nanoprobe tencor p10 profilometer," [Online]. Available: http://www.charfac.umn.edu/instruments/tencor_p10_description.html

[75] Y. Q. Qu1, R. Melamud, and T. W. Kenny, "Using encapsulated mems resonators to measure evolution in thin film stress," *IEEE Transducer Conf.*, vol. 21-25, pp. 1138-1141, 2009.

[76] J. R. Brauer, "magnetic actuators and sensors," John Wiley & Sons, ISBN: 978-1-118-50525-0, Wiley-IEEE Press, pp. 51-59, Jan 2014.

[77] H. Elbahr, T. A. Ali, A. Badawi, and S. Sedky, "Simulation of a new pzt energy harvester with a lower resonance frequency using comsol multiphysics," *Proc. 2014 COMSOL Conf. Boston*, 2014.

[78] K. Brooks, D. Damjanovic, N. Setter, P. Luginbuhl, G. Racine, and N. Derooij, "Piezoelectric response of pzt thin film actuated micromachined silicon cantilever beams," *App. Ferroelect. Symp.*, pp. 520 -522, 1994.

[79] K. I. Hong, S. B. Kim, S. J. Kim, and D. K. Choi, "Cantilever type pzt microsensor using resonance frequency for biomems application," *SPIE BioMEMS Smart Nanostruct.*, vol. 4590, pp. 337-344, 2001.

[80] G. Sreenivasulu, P. Qu, V. M. Petrov, H. Qu, and G. Srinivasan, "Magneto-electric interactions at bending resonance in an asymmetric multiferroic composite: theory and experiment on the influence of electrode position," *J. App. Phys. 2015*, vol. 117, pp. 174105, 2015.

[81] M. Zang, S. M. Zurn, D. L. Polla, B. J. Nelson, and W. P. Robbins, "Design, simulation and fabrication of a bridge structure microstransducer," *Mod. Sim. Microsys.*, pp. 265-268, 2000.